

Department of Precision and Microsystems Engineering

3-D printable flexible diamond electrodes

Stach van Leeuwen

Report no : 2023.087
Coach : Dr. J.G. Buijnsters
Professor : Dr. J.G. Buijnsters
Specialisation : Micro and Nano Engineering (MNE)
Type of report : Thesis
Date : 25 October 2023

MSc thesis in Mechanical Engineering

3-D printable flexible diamond electrodes

Stach van Leeuwen

October 2023

A thesis submitted to the Delft University of Technology in partial fulfillment of the requirements for the degree of Master of Science in Mechanical Engineering

Stach van Leeuwen: *3-D printable flexible diamond electrodes* (2023)

The work in this thesis was carried out in the:



**Precision and
Microsystems
Engineering**

Dept. Precision and Microsystems Engineering
Delft University of Technology

Supervisors: Dr. Ivan Buijnsters
Dr. Simona Baluchová

Contents

Abstract	vii
Acknowledgements	viii
1 Introduction	1
2 Literature Review	2
2.1 Diamond – background information	2
2.1.1 Diamond crystal structure	2
2.1.2 Diamond material properties	3
2.1.3 Diamond vs graphite	3
2.1.4 Carbon phase diagram	4
2.1.5 Synthetic diamond	4
2.1.6 Doped diamond	7
2.1.7 BDD electrodes	8
2.2 3-D printed composite electrodes	10
2.2.1 Why 3-D printing?	10
2.2.2 3-D printing techniques	12
2.2.3 Carbon-based printed electrodes	17
2.2.4 Diamond-based printed composites	23
3 Knowledge Gap and Research Objective	26
3.1 Knowledge gap	26
3.2 Research objective	26
3.3 Research questions	26
4 Materials and Methods	27
4.1 Chemicals	27
4.2 Composite preparation	27
4.2.1 SLA-based composites	27
4.2.2 FDM-based composites	28
4.3 3-D printing	30
4.4 Characterization	30
5 Results and Discussion	34
5.1 Powder characterization	34
5.1.1 Powder size and shape	34
5.1.2 Powder composition	35
5.2 SLA-based Composites: Fabrication and Characterization	36
5.2.1 Fabrication	36
5.2.2 Morphological and surface characterization	37
5.2.3 Mechanical, electrical and electrochemical characterization	38
5.3 FDM-based Composites: Fabrication and Characterization	41
5.3.1 Fabrication	41
5.3.2 Mechanical characterization	44
5.3.3 Electrical characterization	46
5.3.4 Morphological and surface characterization	49
5.3.5 Electrochemical characterization	51
6 Conclusion and Outlook	59
6.1 Powder characterization	59

Contents

6.2	SLA-printed composites	59
6.3	FDM-printed composites	59
6.4	Recommendations for future work	60
Bibliography		61
A Appendix 1		73
B Appendix 2		77

Abstract

Additive manufacturing technologies are widely gaining more attention, resulting in the development or modification of 3-D printing techniques and materials. At the same time, economical and ecological aspects force the industry to develop materials that are easier and quicker to manufacture, while attaining their desired properties. The electrochemistry field can certainly take advantage of this fabrication tool for sensing and energy-related processes. In particular, the fabrication of flexible sensing devices could extensively benefit from the currently developed 3-D printing techniques, such as fused deposition modelling (FDM) and stereolithography (SLA), as they provide a good platform for the integration of flexible materials (polymers). Mechanical flexibility of the electrodes is desirable for biomedical sensing applications, as it improves contact between sensor and skin or neural tissue by adopting the shape and decreases mechanical stress.

Boron-doped diamond (BDD) is a popular electrode material because it exhibits metal-like conductivity when sufficiently doped with boron atoms. BDD possesses highly desired electrochemical characteristics such as wide potential window and low background current, while attaining diamond's chemical stability and biocompatibility. The hardness of diamond, however, has hindered its applications in flexible electrodes. Moreover, common manufacturing techniques that focus on flexible BDD electrodes are time-consuming and require complex material transferring steps.

In this work, two 3-D printing techniques, FDM and SLA, have been employed to explore the possibility to manufacture 3-D printed flexible BDD-based electrodes. The effect of selected 3-D printing technique, BDD particle concentration, and treatment process on the mechanical, morphological, electrical and electrochemical properties of the developed composites was thoroughly investigated. For both SLA and FDM fabrication processes, the presence of BDD particles in the polymer composites resulted in enhanced mechanical properties such as Young's modulus (increased by 230% and 75%, for FDM and SLA, respectively), but caused a reduction in tensile strength and elongation at break. The FDM-based composites additionally allowed higher weight percent of BDD fillers to be introduced, 40 wt.% in contrast to only 12.5 wt.% achieved by SLA. For this reason, further development of composite electrodes was devoted to FDM.

Herein, an innovative, flexible, 3-D printed conductive composite was developed through FDM, which displayed promising mechanical and electrochemical characteristics. By using a unique combination of a flexible polymer, thermoplastic polyurethane (TPU), and fillers, BDD particles and carbon nanotubes (CNTs), a conductive composite material was fabricated which enabled its use as a flexible electrode. Three different compositions were prepared that each consisted of TPU, CNTs and BDD, with CNT-to-BDD ratios of 1:0, 1:1, and 1:2. For the TPU/CNT/BDD electrodes, the electrical conductivity was significantly improved with the addition of BDD particles and displayed an increase of over 7 times (up to 1.2 S/m) compared to without BDD. This effect was similarly visible in the electrochemical characterization, and well-developed peaks were observed in the presence of two commonly used redox markers $[\text{Fe}(\text{CN})_6]^{3-/4-}$ and $[\text{Ru}(\text{NH}_3)_6]^{3+/2+}$ with increasing BDD concentration. Surface treatment of the TPU/CNT/BDD electrodes drastically enhanced the electrochemical properties such as double-layer capacitance (C_{dl}) by 250 times, but also led to a significant increase in peak current intensities for both redox markers. The detection of dopamine was successfully achieved through the fabricated BDD-based composite electrodes. This study provides a state-of-the art, novel composite material that is characterized by excellent flexibility, attractive electrical conductivity and promising electrochemical characteristics. It provides insights into the interactions between composite components and their impact on the electrical and electrochemical properties of the 3-D printed electrode surfaces.

Acknowledgements

This project would not have been feasible without the guidance and helping hands of several people. Therefore, I would like to take this opportunity to express my deepest gratitude and appreciation to those who supported me in this journey at the TU Delft, and especially during the course of my master thesis. I'm extremely thankful to TU Delft for providing me the opportunity to perform my thesis under their name, and I feel incredibly proud to have been part of this incredible education and research institute.

Firstly, I would like to thank my supervisor, Dr. Ivan Buijnsters, for his advice, continuous support, and supervision during my master thesis. His immense knowledge, experience, and enthusiasm on diamonds have played a key role in the completion of my research work, and I am grateful to have been provided the opportunity to be part of his project. Being always open, honest, and able to provide coherent feedback is something I appreciate incredibly. Working with him has been an invaluable experience, and I feel truly fortunate to have had him as my supervisor.

I would also like to express my deepest appreciation to my other supervisor, Dr. Simona Baluchova, for her patience, guidance, and supervision. Her exceptional knowledge on, especially electrochemistry, has contributed significantly to the completion of this research. I would also like to express my appreciation for always being there when I needed her support, reviewing my progress constantly, and guiding me through my research. It was always reassuring to know that I could turn to her for questions and advice, both on a professional and personal level. I am truly grateful for her presence, support, and encouragement during this project.

Furthermore, I would like to thank the technical support staff at PME for their active involvement in this project. In particular, Bradley, Patrick, Gideon, and Alex were my reliable pillars of support. Their involvement and quick responses in this project were truly remarkable.

I want to thank Dr. Baris Kumru and Dr. Roy Awater from The Faculty of Aerospace Engineering at TU Delft, for the collaboration and providing me the opportunity to perform parts of this research at their faculty. Their support, and great amount of advice, have significantly contributed to this project.

Thank you to all the fellow graduate students, researchers, and PME staff members for their presence, and interest in my research topic.

I am also grateful for the friends I made during my years as a student. Our time together in Delft was not only about studying, but also about creating unforgettable memories. Thank you for being a part of this wonderful journey.

Finally, I must express my very profound gratitude to my parents, my girlfriend, my sister and to my other family members for providing me with unfailing support and continuous encouragement throughout my years of study and through the process of researching and writing this thesis. Their love, encouragement, and belief in me have been a constant source of motivation. This accomplishment would not have been possible without them. Thank you.

Financial support from the Dutch Research Council (NWO) through the ENW-XS (project no. 22.2.114) is gratefully acknowledged.

1 Introduction

Diamonds have been known for their long, decorative use in the gemstone industry and are considered the most valuable and sought-after material. Their outstanding material properties, such as extreme hardness, high thermal conductivity, chemical stability and optical transparency, have contributed to a tremendous amount of interest in the scientific community and industry too. Researchers have started to explore diamond's material properties, however its applications in the engineering industry remain rather limited. High cost, quality variations and processing difficulties of natural diamond have restrained engineers from the use of diamond for engineering purposes. Recent advances in the production process of synthetic diamond have overcome existing limitations and enabled scientists to further explore the astounding properties of diamond. The ability to function as an electrically conductive material has extended the field of new applications. By intentionally introducing boron impurities (dopants) in the diamond crystal, the naturally insulating behavior of diamond changes and it becomes electrically conductive. Boron-doped diamond (BDD) has become an attractive electrode material for electrochemical sensing devices. because they exhibit superior features such as wide potential window, low background current and chemical stability.

As applications and technology advance, electrodes with better performance, more complex designs and versatile characteristics are demanded. Complex electrodes, often integrated with flexible parts, are required to keep up with the technological development. Among the several types of diamond electrodes, the recent use of particulate (powder) BDD electrodes has especially raised great interest. Due to the easy incorporation of the particles within flexible materials such as polymers, fabrication limitations inherent to the current manufacturing technique can be overcome. This allows for a more efficient fabrication process that will greatly reduce complexity, and involves substantially less amount of steps, labor, and time. Additionally, current flexible thin-film BDD electrodes focus on 2-D planar designs, imposing limitations on current density and electric capacity. Their fabrication process, based on transferring material onto different substrates, is time-consuming and involves many steps. 3-D printed electrodes may accomplish higher electrical performance by increasing the surface area of the electrode for electrochemical reaction, and their fabrication process is less complex.

The main objective of this M.Sc. thesis project is to investigate the possibility of manufacturing flexible BDD-based electrodes through 3-D printing techniques, something which has never been reported before. By providing a straightforward approach to fabricate BDD electrodes, a more efficient and low-cost production process will be explored. Moreover, the newly developed electrodes will be subjected to different characterization techniques such as mechanical, morphological, electrical and electrochemical analysis, to investigate their performance.

This thesis report will cover six chapters in total, with the introduction being chapter one. Chapter two covers the relevant background information regarding diamond and the use of 3-D printing with different carbon-based materials, including diamond. It covers the manufacturing methods, examples from the literature and the characteristics of BDD electrodes. The third chapter will cover the research objective, knowledge gap and the research questions. Chapter four provides an overview of the materials and methods used in the project. Chapter five presents the obtained results. Finally, in Chapter 6, the conclusions drawn from this research are provided along with recommendations for future work on this topic.

2 Literature Review

2.1 Diamond – background information

This chapter discusses the important information that is required to understand the crystal lattice and material properties of diamond. It will deal with the structure of the diamond crystal, discuss the differences and similarities with respect to graphite, the main production methods for synthetic diamond, list the (semi)-conducting properties and will further discuss the common and potential applications of diamond in engineering.

2.1.1 Diamond crystal structure

Diamond is widely known to be the material with some of the most impressive properties [1]. Its discovery, which has been reported thousands of years ago [2] has led to an incredible demand for the mineral which has made diamond one of the most valuable materials on the planet. Its crystal structure contributes to the unique properties of the material, which are nowadays still being explored.

The atomic structure of diamond, commonly referred to as the diamond lattice, is solely built up of carbon atoms. The carbon atoms are arranged in a tetrahedral shape, which means that each carbon atom is connected to four neighboring carbon atoms. These tetrahedral shapes are the basis of the entire diamond lattice. The carbon connections are strong covalent bonds, which form the dense crystal structure and contribute to the incredible properties that diamond possesses (see Section 2.2). The most common crystal structure of diamond is called the cubic diamond structure, see Figure 2.1. It is formed by four tetrahedral units which are connected together. The diamond unit cell hosts eight carbon atoms.

The diamond unit cell can be considered as a combination of two interpenetrating face-centered cubic (FCC) sub-structures positioned along the diagonal axis with an offset of $1/4$. The FCC structure is described by a cubic unit cell (with a lateral size of 0.357 nm) with one atom at each corner and one at the center of each face. Diamonds can, under very specific conditions, also form hexagonal diamond [3], but it is far less common than cubic diamond.

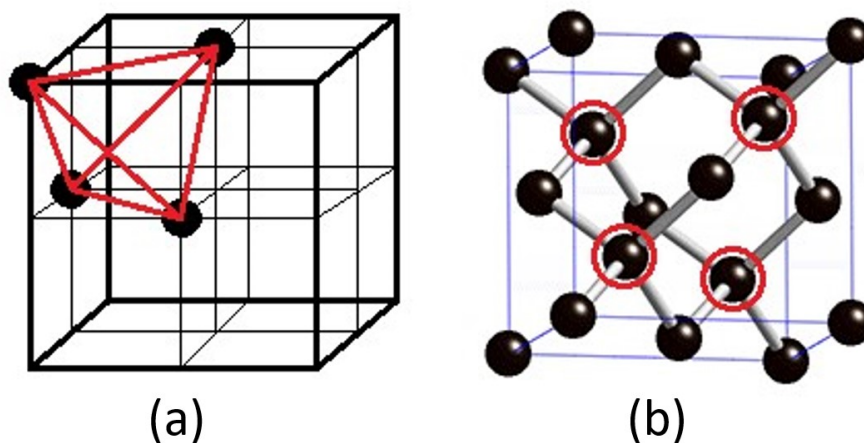


Figure 2.1: Diamond unit cell [4]: (a) with the tetrahedral shape indicated, and (b) with the four interior carbon atoms circled in red. (Note the tetrahedral arrangement of carbon-carbon bonds for these highlighted atoms.)

2.1.2 Diamond material properties

The crystal structure and strong covalent bonds give rise to unique properties within this material. Diamond is, for example, the hardest naturally occurring material in the world. It distinguishes itself from any other material in terms of their physical, mechanical and thermal properties. A selection of these properties is presented in [Table 2.1](#).

Table 2.1: Material properties of diamond [5].



Property	Value
Density	3440 - 3580 kg/m ³
Mohs hardness	10
Young's modulus	1050 - 1210 GPa
Tensile strength	2800 - 2930 MPa
Toughness	0.0539 - 0.0802 kJ/m ³
Melting point	3720 - 3910 °C
Thermal conductivity	900 - 2320 W/m.°C
Electrical conductivity	10 ⁻¹⁴ - 10 ⁻¹² S/m

Apart from the outstanding mechanical and thermal properties that diamond possesses, it is important to emphasize the chemical stability and robustness of diamond too. Diamond is highly chemically stable, which means that it will not react with any chemical reagents including strong acids and bases at room temperature. The strong chemical stability also makes diamond highly biocompatible. In terms of optical properties, diamonds can be found in different colors. Depending on the presence of crystallographic defects, diamonds can occur in colors covering the full color spectrum. Crystallographic defects generally include impurities present within the crystal or structural defects like vacancies or edge dislocations. Therefore, the purest form of diamond would be transparent and colorless. More information regarding the effect of impurities on the coloration of diamond will be provided in [Section 2.1.6](#).

2.1.3 Diamond vs graphite

Diamond is not the only material that is purely based on carbon. One material that is quite similar in terms of composition is graphite. Diamond has a tetrahedral-based configuration where a single carbon is connected to four other carbon atoms with strong covalent bonds. Graphite, however, has a hexagonal sheet structure where there are only three atoms connected to a single carbon atom. This seemingly small difference strongly affects the material properties of graphite compared to diamond [2]. Diamond is an incredibly hard material and has a 3-D cubic structure, graphite however is soft, and its atoms are arranged in a 2-D layered structure, see [Figure 2.2a](#). In between these layers, which are called graphene, are bonds that connect the different layers in the graphite lattice. These connections are however very weak, which give graphite its mechanically soft property. In terms of electrical properties, it is evident to mention that diamond is an excellent insulator, mainly because there are no free charge carriers present in the crystal structure. Graphite on the other hand is a good conductor of electricity. Delocalized electrons are able to move between the layers and carry charges. [Table 2.2](#) presents the most evident differences between diamond and graphite.

Table 2.2: Properties of diamond vs graphite [6].

Diamond	Graphite
Hard	Soft
Colorless	Black
Transparent	Opaque
Non-conductive	Conductive
Four covalent bonds	Three covalent bonds
Cubic geometry	Layered geometry
	

2.1.4 Carbon phase diagram

Diamond is the stable allotrope of carbon, but only at very high temperatures and pressures, see Figure 2.2b. More precisely, it means that diamond is thermodynamically stable and will remain in this stable state under the indicated conditions. However, under atmospheric pressure diamond is said to be thermodynamically unstable which means that diamond would slowly convert back to its more stable allotrope, graphite. Still, this conversion is happening at such a slow pace that diamond is therefore considered to be metastable [7]. Essentially, it means that diamond is thermodynamically unstable at atmospheric pressure but kinetically stable due to a large activation energy barrier [2]. Following from the strong covalent bonding, the large activation energy barrier is the main reason which is preventing diamond, once it is formed, to convert back to the more advantageous graphite state. At atmospheric pressure and room temperature, graphite is generally the stable allotrope of carbon which can be seen in Figure 2.2b. However, this does not mean that diamond cannot be produced under these conditions. One method that uses the meta-stability of diamond is called chemical vapor deposition (CVD). Various other methods for the production of synthetic diamond have also been developed over time, see Figure 2.2b. They will be discussed in the following section.

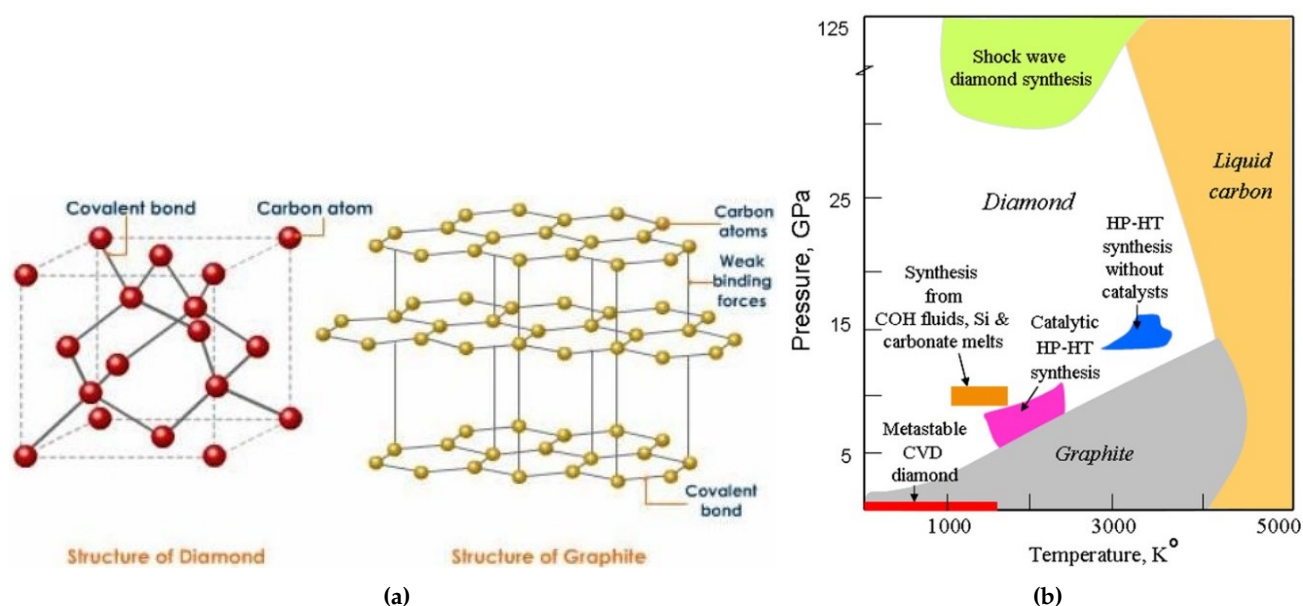


Figure 2.2: Graphical image of (a) diamond structure vs graphite structure [8] and (b) carbon phase diagram [9].

2.1.5 Synthetic diamond

Throughout the past 300 years, starting from 1797, scientists have been trying to synthesize diamonds by manipulating carbon-based materials [10]. The following sections are dedicated to three methods that describe the production of synthetic diamonds under specific conditions and for certain applications.

Detonation nanodiamond

One method of creating synthetic diamond is through a process called detonation nanodiamond (DND) or shock wave diamond synthesis, as depicted in Figure 2.2b. DND is produced by detonation of carbon-containing explosives in a closed reaction vessel. The process is divided into three main steps; synthesis, processing, and modification (see Figure 2.3).

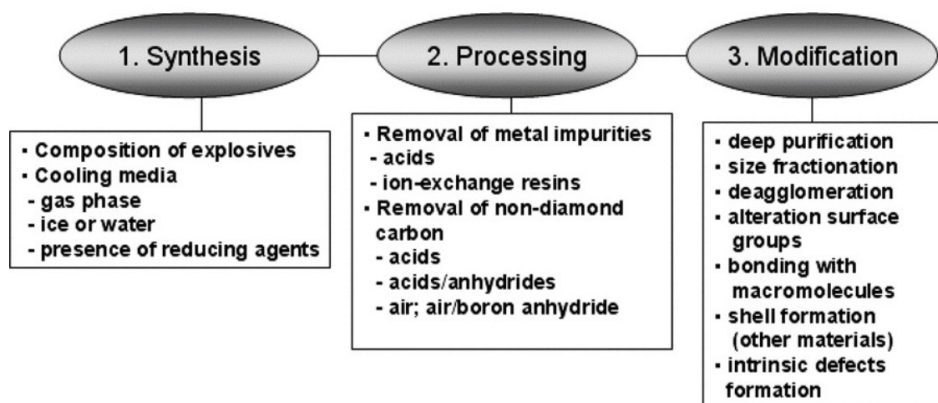


Figure 2.3: Process overview of detonation nanodiamond [11].

Firstly, detonation of explosives, typically TNT, induces a strong shock-wave which compresses the material, heats it up and starts its decomposition. During this decomposition process, high amounts of energy are released, which pass through the material. Subsequently, temperatures from 2500 K and pressures of around 25 GPa are generated which correspond to a stable region of diamond formation, see Figure 2.2b. The formation of DND during these complex processes is still not fully understood and remains a field of great interest for researchers. As of today, scientists have established two main requirements for the successful production of DND: the formed diamond needs to be prevented to convert back to graphite by closely monitoring the cooling rates, and the composition of the explosives must provide a stable environment for the diamond particles to form. These two requirements determine the rate of formation and quality of the DND. The mass-ratio of the used explosives with respect to the surrounding media and the shape of the explosives also influence the diamond yield [11]. The second part of the production of high-quality nanodiamonds involves processing. After the synthesis process, the DND particles generally contain high percentages of graphite (25-45 wt.%) and other incombustible impurities such as metals (1-8 wt.%) which result from detonation and explosives. Removal of these impurities is performed by a purification process, see Figure 2.4. After purification, the percentage of purity is between 90-99% since nitrogen, hydrogen, and oxygen residues are still present internally. These impurities are confined in the carbon-structure, which means that additional purification steps are required. Through different oxidation techniques, removal of confined impurities is achieved.

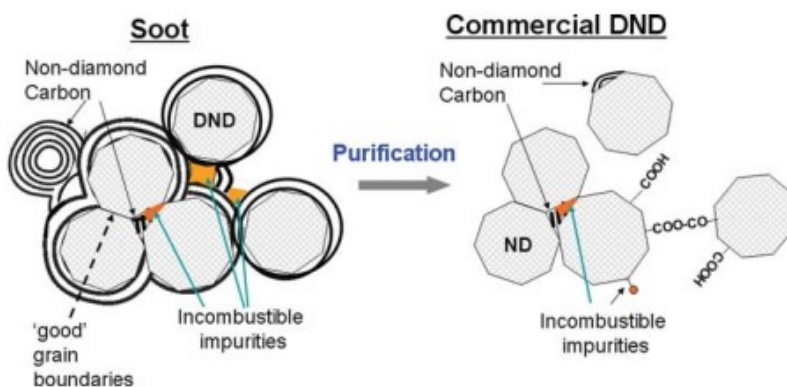


Figure 2.4: Purification process of detonation nanodiamond [11].

Lastly, the DND particles are treated through a modification process. This is done because either certain impurity levels are still too high, the average size of particles is too large, or the surface chemistry is not suitable for the intended application. Additional modifications might be fractionation, deagglomeration or deep-purification for example. After the process, high-purity diamond particles with sizes from 3-6 nm are obtained. DND is currently used in many engineering fields such as thermal, biological, mechanical and optical [11].

High-pressure high-temperature

High quality single-crystal diamonds can be produced by using high-pressure and high-temperature (HPHT) synthesis. First reported in 1955, when the General Electric Research Laboratories were the first ones to successfully reproduce diamonds [7]. In the HPHT-process, a carbon source such as graphite is compressed in a hydraulic press wherein, the carbon source is exposed to temperatures and pressures where diamond is in its stable region. The conversion is performed with (indirect conversion) or without (direct conversion) a catalyst, depending on the application [2]. Indirect conversion is performed with the addition of a metal solvent or catalyst to a carbon-based powder and placed in a growth chamber. The presence of a metal catalyst results in a faster conversion of graphite to diamond by lowering the activation barrier. Therefore, a lower pressure and temperature are needed to perform the conversion compared to the direct method. Direct conversion does not require a catalyst to be added to the sample and grows diamond faster than the indirect method. Still, temperatures around 3000 K and pressures above the 10 GPa will be reached, which means that special equipment and machinery is required. Direct conversion can yield diamonds in sizes from nm up to mm, meaning that large single diamond crystals can not be produced. Indirect conversion, on the other hand, is capable of producing large diamond crystals (centimeters) [12] and is therefore the most commonly used method in the commercial diamond growing industry [13]. The HPHT-method has however certain drawbacks. Firstly, it is very energy consuming as it requires generally high temperatures and high pressures, especially the direct method, see Figure 2.2b. Secondly, the production of single crystal diamonds is difficult to control and limits the range of application for which it can be used [2]. Consequently, other techniques have been developed to establish a more efficient, less energy consuming and more controllable process for diamond growth. One of these techniques is chemical vapor deposition (CVD).

Chemical vapor deposition

The CVD method is performed at conditions where diamond is metastable, generally at low pressures ($\ll 1$ bar). It involves a gas-phase chemical reaction with hydrocarbon and carbon gasses that occurs above a solid surface, which causes carbon deposition on a substrate. CVD requires activation of carbon-based precursor molecules from the gasses to realize the deposition of carbon. This activation is done either thermally (hot-filament), by a plasma (microwave, DC, RF) or through a combustion flame [2]. Figure 2.5 shows a schematic of the process of CVD. Process gasses are introduced into the growth reactor at first. Then as the gasses pass through the activation region which is a hot-filament (thermal) or plasma (electric), reactants are provided with a certain amount of energy until they dissociate to atoms and form radicals. This process of molecules fragmenting will further increase the temperature in the chamber. When the reactants pass the activation region, they start to mix with each other and initiate complex reactions until they hit the substrate. At this point three

things can happen: the particles can adsorb and react with the surface, or desorb back into the gas phase, or diffuse close to the surface. Generally, the substrate is covered with diamond seeds ranging from nm to mm to initiate the diamond growth. Within the process of CVD, multiple parameters determine the rate of diamond growth and purity of the diamonds. Firstly, the composition of gas mixture, more specifically the carbon-to-hydrogen ratio in the gas mixture, determines the quality of diamond and also the growth rate. A higher carbon concentration results in higher growth rates but at the same time increases the amount of defects, resulting in a lower quality of diamond film (i.e., higher content of graphitic phases) [14]. Secondly, the pressure of the system will affect the growth conditions. Higher pressure results in a higher concentration

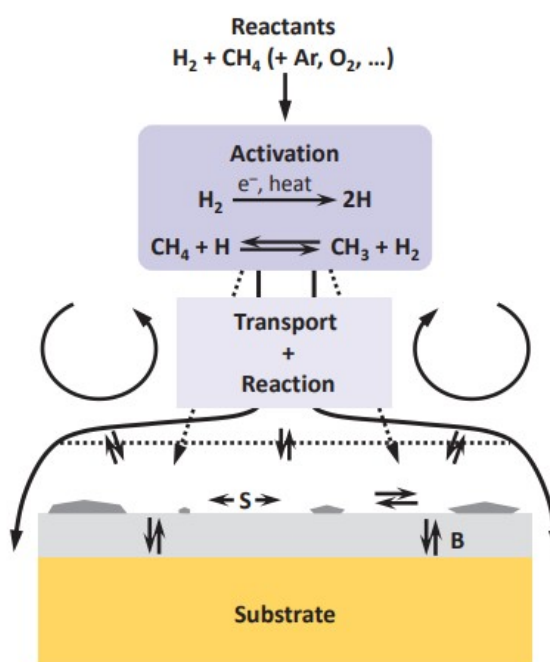


Figure 2.5: Schematic representation of the diamond CVD process [13].

of graphite formed in the film [15]. Lastly, substrate temperature which is generally between 700-1000°C also determines the growth and quality of diamond. As substrate temperature decreases, the percentage of non-diamond content increases in the film [16]. For commercial laboratory diamond growth, CVD is currently the most popular growth technique as it offers an efficient, low-pressure method that allows for controllable growth conditions. CVD is used to cover relatively large surface areas of diamond layers and has the ability to grow on structured substrates. High-purity single crystal diamond can also be grown by the CVD method when using mm/cm-sized diamond seed plates [17].

2.1.6 Doped diamond

Doping

Diamond has outstanding mechanical, thermal and chemical properties which are unique compared to any other material [1, 18]. Also, diamond is a wide-gap semiconducting material ($E_{gap} = 5.48$ eV) with a tremendous potential for electro(chemical) applications. It has the highest atomic density of any solid material due to the small size of the carbon atoms present in the lattice that form short covalent bonds. This makes it difficult to fit larger atoms in the lattice, resulting in only a small selection of atoms that can “fit” within the diamond lattice. These so-called “impurities” are sometimes introduced in the diamond lattice during the growth process. Several impurities have been reported in diamond; nitrogen, boron, nickel, cobalt, sulfur, phosphorous, silicon, hydrogen, and germanium are some examples [13, 19]. Unintentional contamination of these elements is inevitable due to their presence in the growth environment. Impurities can affect various properties, for example a change in optical appearance. Defects and dislocations create electronic states in the band gap, this allows for the absorption of light for specific wavelengths, which results in the difference of coloration [20]. Nitrogen impurities change the transparent, clear appearance of pure diamond to a typical yellow, brownish color. Boron impurities on the other hand result in a more blueish colored diamond.

Yet, impurities can also contribute to an enhancement of other material properties. Defect sites can affect the electrical, structural and thermal properties of the material. The ability to manipulate defect sites by introducing impurities in the diamond lattice enables scientists to tune the properties of the material. This process of intentionally introducing impurities in the diamond lattice is known as doping. As of today, nitrogen and boron are the most widespread elements being used for doping diamonds [21, 22].

Doped diamond as a (semi)-conductor

Diamond had rarely been considered a potential material for electrically conducting purposes due to limitations like its intrinsically high resistivity and previously mentioned wide-bandgap. Nevertheless, the high thermal conductivity [23], high carrier mobility [24], chemical inertness and extreme hardness of diamond triggered much attention as a robust electronic material. Its intrinsic properties are desirable for use in high-power devices and devices used at high temperatures, high voltage and in strong chemical environments [1, 25–28]. Therefore, diamond-based power devices are expected to significantly reduce both conduction and switching losses, which has resulted in more extensive research regarding possible applications such as semiconductors. Fortunately, over the past few decades, advances in the production of synthetic diamonds have also led to successful approaches to introduce dopants in diamond. To produce diamond with useful semiconducting properties, introducing controlled amounts of impurities is necessary. This should result in a sufficiently high and stable density of charge carriers, which can make diamond an electrically (semi)-conducting material. Two main elements are important in semiconducting physics which are p-type and n-type materials. A p-type semiconducting material is generally a bulk material with one element added that has one fewer electron, called an acceptor. On the other hand, adding an element with one extra electron (donor) than the bulk material will make it an n-type semiconducting material. P-type and n-type materials are essential in the operation of electrical devices like transistors and diodes nowadays [21].

Nitrogen is the most commonly found impurity in (natural) diamond due to its abundant presence in air (78 vol%). It can be easily incorporated in the diamond lattice, since there is a strong resemblance in their atomic sizes. Furthermore, nitrogen impurities can act as electron donors in the diamond lattice and can therefore be considered n-type dopants. However, using nitrogen for n-type semiconducting applications has proven to be ineffective. Despite the lack of success for nitrogen doped diamond as an n-type conductor, other applications for nitrogen doped diamonds have been reported. For example, they have been used

for thermoluminescence and radiation sensors [29], thermionic electron emitters [30], optical biosensors [31] and coatings for micro tools [32]. Also, the recent developments on optical centers involving nitrogen for micro/nano scale magnetometry [33–35] and quantum computing [36] are gaining lots of traction.

Boron has been used as an effective dopant for (semi)-conducting applications since 1973 [37], as it can act as an acceptor in the diamond lattice. By direct substitution of carbon atoms with boron atoms, a heterogeneous p-type material can be produced with conductivities ranging from semiconducting to near metallic [38] and even super conducting at low temperatures [39]. As a rule of thumb, a ratio of ~ 1 boron atom to 1000 carbon atoms is necessary to generate sufficient semimetallic properties (see Figure 2.6a), similar to a dopant density of $\sim 10^{20}$ B atoms per cm^3 . Diamond can be doped with boron using gas-phase growth techniques such as CVD, or with HPHT conversion of graphite using transition metal catalyst. During these processes, boron will typically be added in the form of di-borane or as trimethyl borane gas to obtain boron-doped diamond (BDD). Through this way, BDD can be grown in a controlled environment layer by layer, creating thin-film BDD.

BDD is already found in many applications like electrochemical sensors, biochemical sensors, wastewater treatment and supercapacitors [40–52]. As boron effectively takes up the same position as displaced carbon atoms, high amounts of boron doping are possible. Together with its relatively low activation energy (0.37 eV) compared to nitrogen, boron has emerged as the most suitable dopant in the industry [53]. A schematic image presenting the effect of boron doping on the band gap energy is presented in Figure 2.6b. Various properties of BDD as an electrode material will be discussed in the following section, together with the different types of BDD material.

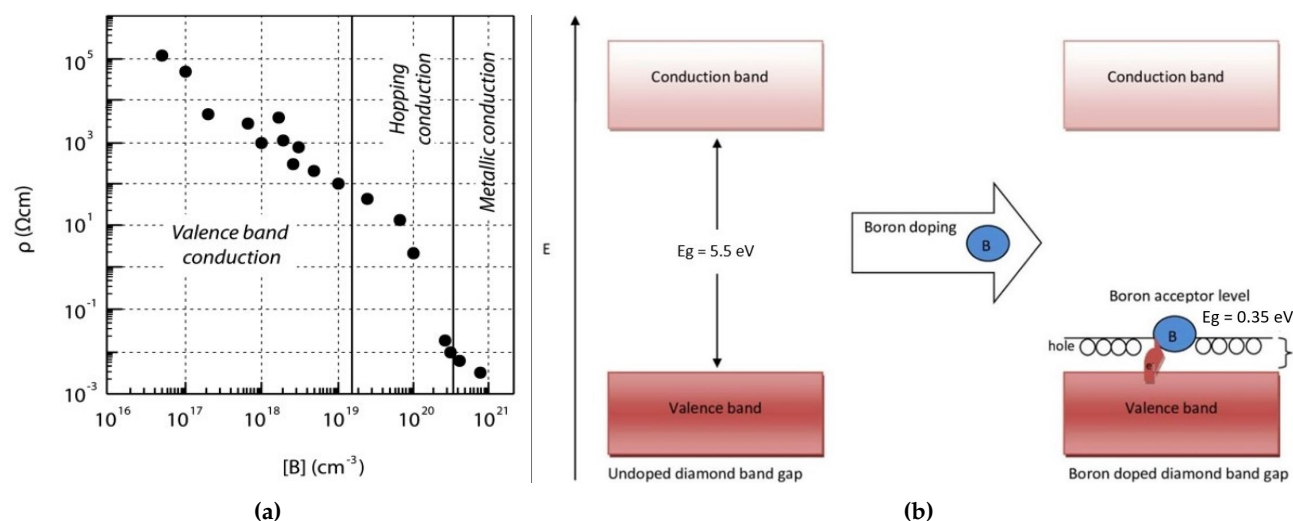


Figure 2.6: Effect of (a) boron concentration on electrical resistivity [53] and (b) boron doping on the band gap energy [40].

2.1.7 BDD electrodes

Introduction

BDD electrodes find their application mainly in electrochemical sensing devices. These sensing devices generally consist of multiple electrodes. A working or sensing electrode (e.g., BDD), a reference electrode and a counter electrode. Any electrochemical change at the working electrode, by oxidation or reduction, is monitored as a signal. This signal is displayed by a change in either current, voltage, or charge. By connecting this to the full system in a circuit, the system can detect and measure certain currents and amplifies the output according to the device.

The first example of diamond used as an electrode for electrochemical measurements was by Iwaki and colleagues in 1983 [54]. They discovered that introducing dopants in the natural diamond reduced the resistivity of the electrode. Later, Nishimura et al. were one of the first in 1991 to investigate the material and electrical properties of BDD-electrodes fabricated by a CVD process [55]. They concluded that the boron impurities

were essential for conductive behavior of the electrodes, and that BDD electrodes with 200 and 400 ppm boron showed an ohmic behavior.

BDD electrode types

Currently, three different types of BDD electrodes are being explored for sensing applications. The first type is based on a single-crystal boron-doped diamond (SC-BDD). This specific material type of electrode is particularly attractive because SC-BDD has no grain boundaries and has a nearly perfectly flat surface. In addition to that, the level of non-diamond particles (impurities) is relatively low, which would make SC-BDD electrodes suitable for optical and electrical sensing applications [17, 56]. However, SC-BDD electrodes studies are rare due to the challenge of producing well-defined, sufficiently doped, single crystals at a size sufficient for electrochemical investigation. The high requirement of substrate uniformity and the existence of grain boundaries leads to problems such as stress and defects, which quickly affect the quality of the SC-BDD. The various challenges of creating high doping concentrations, which are required for metallic-like conductivity to be achieved, had researchers questioned if SC-BDD would be applicable for electrochemical sensor development. Only recently, a paper has been published where researchers were able to grow heavily boron-doped single-crystal diamond, a promising material for electrochemical sensing applications [57]. The second type of electrodes is based on polycrystalline boron-doped diamond (PC-BDD), see Figure 2.7. PC-BDD films, produced mainly by the CVD process, can provide remarkable properties for high-performance MEMS/NEMS devices, with relatively low fabrication cost [2]. The polycrystalline surface is non-homogeneous and consists of many grain boundaries. Non-diamond impurities typically reside at these grain boundaries, which make PC-BDD less pure compared to SC-BDD [17]. These grain boundaries, however, can easily host other impurities such as boron or nitrogen, which makes them suitable for high-level doping. Therefore, the vast majority of the currently produced and employed BDD electrodes have a polycrystalline nature. The third type is a relatively new and unexplored material type of BDD electrodes. Here, BDD electrodes are fabricated using micro or nano-sized diamond particles. By mixing BDD powder with a binding material such as a polymer, a conductive composite suspension is obtained which will function as an electrode material [46, 58]. The suspension can be used to manufacture screen-printed electrodes by deposition of the material on a substrate, and casting it to adjust to a specific shape or design. The BDD-powder solutions can also be used for coating or painting of an electrode to function as a thick-film.



Figure 2.7: Example of various PC-BDD electrodes [59].

BDD electrode properties

BDD-electrodes exhibit superior features that make them very suitable for electrochemical applications. Their high overpotential for oxygen and hydrogen evolution leads to the widest potential window currently known in aqueous environment [60], which is around 3.5 V, see Figure 2.8a. Furthermore, BDD electrodes have a very low capacitance, which means a high signal-to-noise ratio compared to conventional electrodes like gold or platinum [40]. Also, BDD-electrodes can withstand extreme potentials, corrosive environments and

high temperatures. Compared to other metal electrodes or carbon-based electrodes, BDD electrodes retain desired properties for electrochemical sensing devices [53]. All of these promising features have resulted in a tremendous increase in publications over the past decade, see Figure 2.8b.

BDD electrodes can potentially be used for (bio)medical applications to improve our quality of life. BDD electrodes have found applications in electrochemical sensing devices where they act as sensing or working electrode due to their previously listed exceptional properties. Therefore, the main application as a detecting device is to be able to sense certain organic or inorganic compounds.

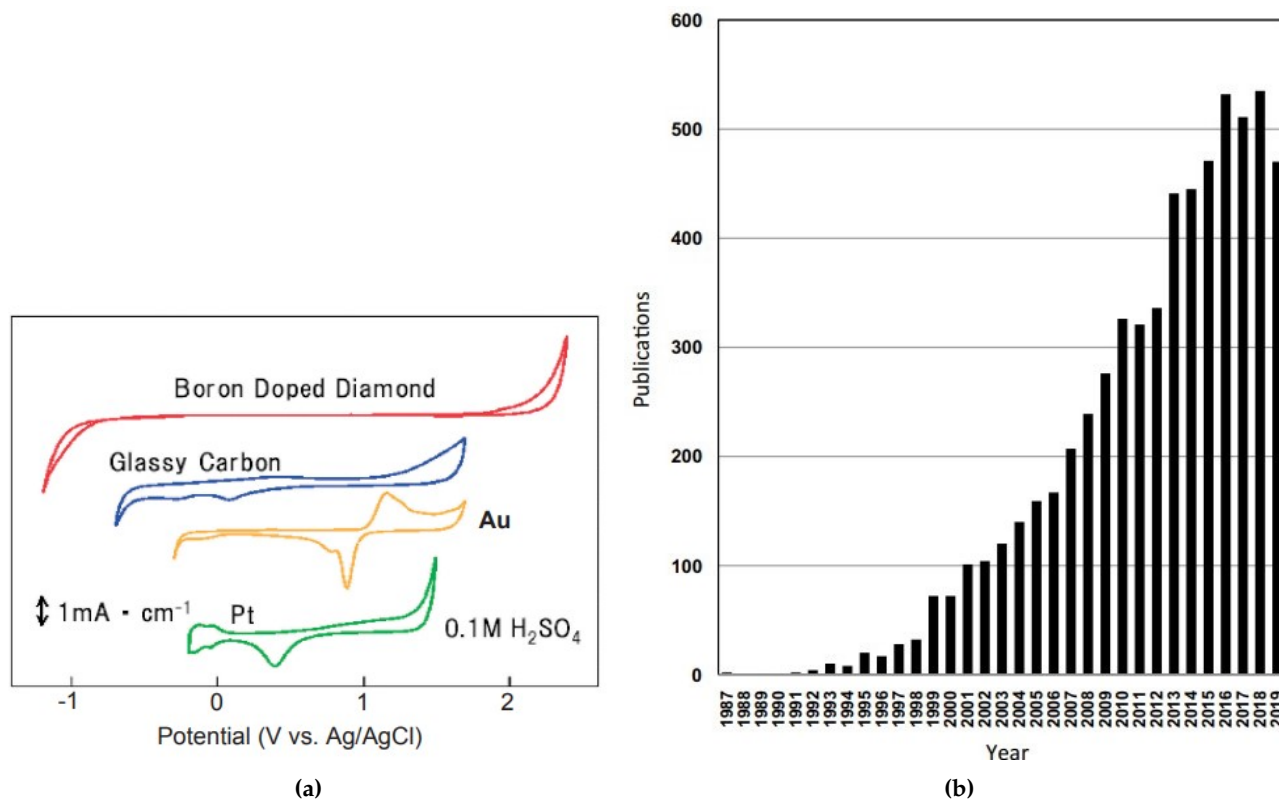


Figure 2.8: (a) BDD electrode potential window compared to other electrodes [60]. (b) Number of scientific publications on diamond electrodes [61].

2.2 3-D printed composite electrodes

This section will discuss the potential application of 3-D printing for the fabrication of flexible BDD electrodes. First, several arguments will be given that clarify the choice of 3-D printing as a manufacturing method. Next, an introduction regarding different 3-D printing techniques will be given. Then, the most promising techniques through which BDD electrodes can be manufactured are discussed. Lastly, various examples will be given regarding (flexible) carbon-based 3-D printed electrodes and also 3-D printed diamond-based composites.

2.2.1 Why 3-D printing?

Since the development of screen-printed BDD electrodes [41, 46, 58, 62] which can be manufactured quickly, cheaply and have proven to be effective, scientists have been looking at ways how to improve this manufacturing process, and the quality of products. Manufacturing techniques like screen-printing have limitations in controlling geometric design, dimensions, and architecture which would compromise their performance [63].

In addition to that, as technology and applications advance, higher quality products with more versatile characteristics are demanded. More complex designs, often integrated with flexible parts, are required to keep up with the technological development. Flexible, polymer-based electrodes are highly desirable in biomedical fields for electrochemical sensing devices such as wearable sensors. By improving the contact between sensor and skin, the electrode can use its flexibility to adopt the shape and reduce internal stress. Current CVD techniques that have been employed to manufacture thin-film BDD electrodes, impose limitations that prevent direct deposition of diamond on a flexible (polymer) substrate. The high diamond synthesis temperature is the main issue which will break down the polymeric substrate. Several papers [64–66] have therefore reported transfer of thin-film CVD diamond from stiff substrates onto flexible polymers to eliminate the temperature problem. This fabrication procedure unfortunately involves many complex, time-consuming steps (etching, photolithography, etc.) and requires expensive equipment, which makes this method incredibly ineffective. A schematic of such a fabrication procedure is depicted in Figure 2.9.

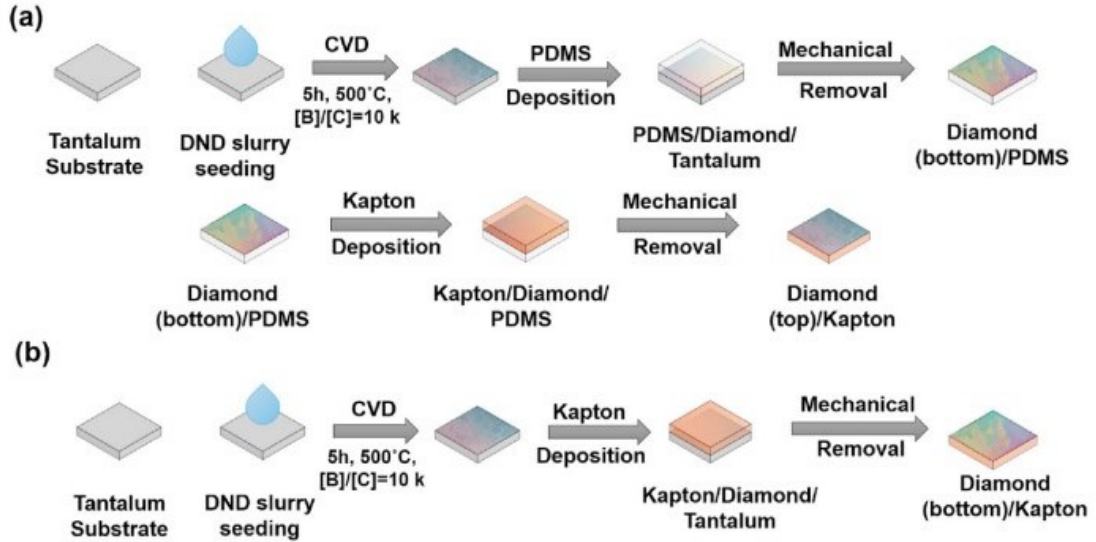


Figure 2.9: Growth and fabrication of flexible BDD electrode: (a) Top-surface/Kapton, and (b) Back-surface/Kapton structure [66].

Furthermore, traditional flexible BDD electrode designs have mainly focused on 2-D, planar structures (thin-film) that require a large surface in order to provide higher capacities. The planar structure imposes limitations on the electrical properties like current density and electric capacity. In order to obtain higher energy densities and better performing electronic devices, 3-D constructed electrodes are strongly recommended. A 3-D structure can enable higher electric densities by more efficiently using space within the material through, for example, a porous design. 3-D structured electrodes enable shorter diffusion paths and more efficient ion-transport [67]. As the world is moving towards better performing, smaller and more complex portable electronics, a manufacturing technique that can provide engineers the tools to manufacture these is essential.

With the recent development of the emerging, novel technology 3-D printing (additive manufacturing), many advances in material development and advanced manufacturing have taken place. Initially, 3-D printing was developed to be used as a rapid prototyping tool. Nowadays, the applications of 3-D printing have shifted from just rapid prototyping to many more different purposes like material development, complex structure design and product conceptualization [68]. 3-D printing is regarded a powerful manufacturing technique that can be used to eliminate design limitations and produce geometrically complex objects from macro- to nanoscale.

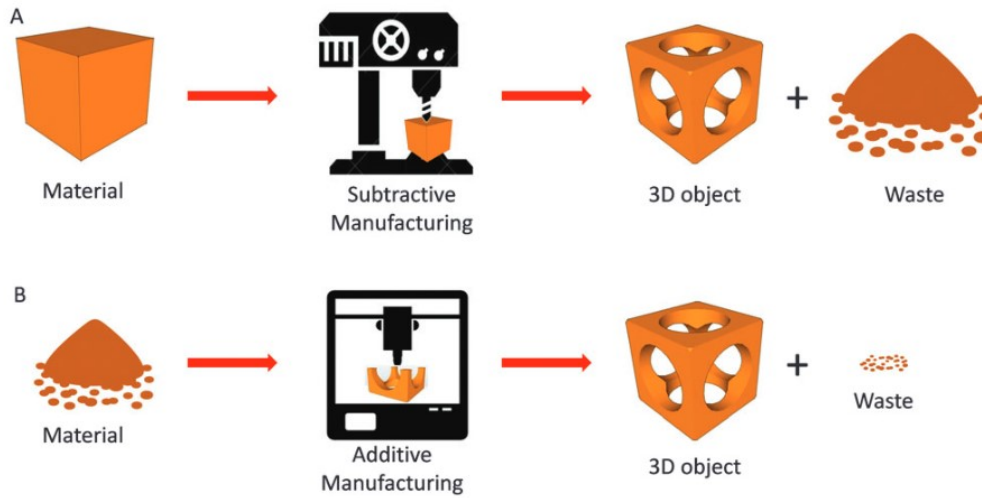


Figure 2.10: (A) Manufacturing process through subtractive manufacturing. (B) Manufacturing process through additive manufacturing [69].

Compared to conventional manufacturing techniques like drilling, milling and sawing, which are considered subtractive manufacturing methods, 3-D printing follows the opposite manufacturing principles where material is added instead of removed. Both manufacturing processes are valid methodologies for fabrication of parts and the choice depends on multiple factors such as material of choice, complexity of the object, number of replicates and the cost. Generally, subtractive manufacturing is used to make metal- and wood-based objects, while 3-D printing will be used for polymer-based objects. With the increasing scarcity of natural resources and materials in the world, and a focus towards more sustainable manufacturing methods, 3-D printing has more often been a preferred manufacturing method. 3-D printing can greatly reduce manufacturing costs by using less energy-consuming machines and reduce material waste, see [Figure 2.10](#).

Over the past two decades, significant improvements in the field of 3-D printing (machines, equipment, software) have been made, leading to the establishment of a reliable, simple and accurate manufacturing method. These developments have resulted in a tremendous amount of interest by engineers and scientists. Numerous research fields like mechanical, electrical, biomedical and even chemical engineering have discovered the advances in this novel manufacturing technique. Electrochemistry is certainly another field of science that could potentially benefit from this, enabling design and fabrication of better performing, more complex and cost-effective electronic devices.

2.2.2 3-D printing techniques

Overview

3-D printing is defined as the process of creating a three-dimensional object based on a computer-aid-design (CAD) model through a layer-by-layer deposition of material. Once a CAD model is designed, it needs to be converted to an STL (STereoLithography) format, which stores the information of the model's surface as triangular sections. The STL file can be read by every 3-D printer and will initiate the slicing process. Here, the printer will divide the model in very thin 2-D cross-sections that will be manufactured on top of each other to make the object. A flow diagram of the process can be seen in [Figure 2.11](#).

Various 3-D printing techniques exist and all can be divided into four main categories based on their working principle: 1) photopolymerisation, 2) extrusion, 3) powder-based and 4) lamination [68]. Photopolymerisation uses photo-polymers or radiation-curable resins in the form of a liquid, as their main material. These photo-polymers will react when exposed to light with certain wavelengths, usually in the ultraviolet region. When irradiation takes place on the photo-polymer surface, complex chemical reactions start to occur and the material becomes solid. Immersing the solidified layer, in a controlled way, allows for multiple layers to be solidified and stacked on each other. This specific method is called stereolithography (SLA). Other methods

that use photopolymerisation as their main working principle are material jetting, continuous interface liquid printing (CLIP) and two-photon polymerization (2PP). The second category is extrusion-based 3-D printing and relies on the working mechanism of extrusion of material. Material is heated inside the machine to a semi-molten state, then slowly deposited through a nozzle on a print-bed. Once deposited, each material layer will solidify so that it stacks on top of the previous deposited layer. Solidification of the material is imposed due to cooling of the deposited material, which is temperature-controlled by the print-bed. The most popular method that uses extrusion is Fused Deposition Modelling (FDM). Another technique that uses extrusion is direct ink writing (DIW). Here, more flexibility with respect to material choice and particle size is provided, which gives more design freedom for engineers. However, usually only low-resolution objects can be manufactured, stringent requirements on the ink's rheological behavior are necessary and post-treatment is always necessary to improve physical and mechanical properties.

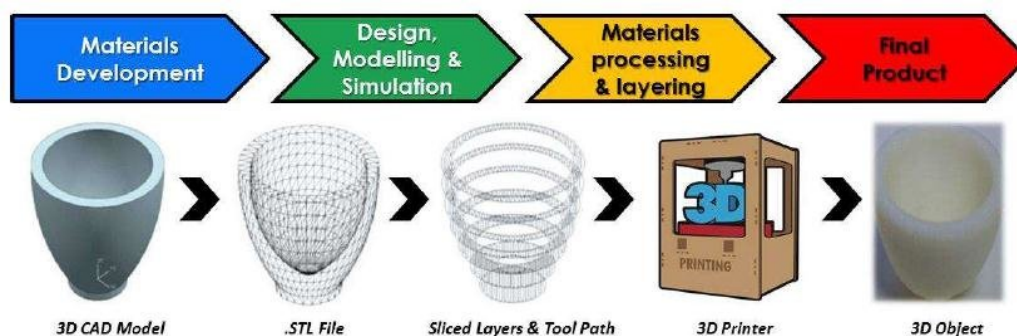


Figure 2.11: Flow diagram of 3-D printing process [70].

Multiple powder-based 3-D printing techniques are existing nowadays: selective laser sintering (SLS), electron beam melting (EBM) and selective inhibition sintering (SIS) are some examples. All of these processes share the same working characteristics. These include one or more thermal sources to induce fusion of the powder particles, a mechanism for controlling the powder particles to a prescribed region and method for smoothing the powder layer and enabling deposition of a new layer. The powder contains solid particles which are mostly metallic and have sizes ranging from 50 to 100 μm . The process of laminated object manufacturing (LOM) involves a layer-by-layer lamination of thin sheets. A sheet is placed on the bed and cut to the desired shape by using a laser. Then a new sheet is loaded on top of the previous one and is cut again. This process continues until the desired 3-D model has been created. To make sure that the layers are bonded together, adhesives or welding techniques are used. A summary of all previously mentioned 3-D printing techniques can be found in Table 2.3.

The electrochemical industry can certainly benefit from the extraordinary progress that has taken place in the field of 3-D printing. It would allow for the production of custom-made electrodes at a lower cost, in a shorter time and with greater versatility. Multiple 3-D printing techniques have been proven to be able to manufacture conductive electrodes with success. Fe-Ni superconductors have been manufactured by Lu and colleagues [71] using 3-D printing. Preparation of the porous structures was carried out using SLM-based powder technology. SLM has also been employed by Ambrosi et al. [72] to manufacture helical-shaped electrodes. These stainless steel electrodes were produced to form a platform for electrochemical devices such as pH sensors. Limitations of this technique are the necessity for post-processing of the metal surface and the minimum required printing dimensions (in mm range). For flexible BDD electrode development, three 3-D printing techniques in particular, will be useful due to extensive opportunities such as introducing flexible polymers in the production process. DIW, FDM and SLA are good candidates that can replace current manufacturing techniques. More attention will be paid to these methods, and a more comprehensive analysis of them as potential techniques to fabricate electrodes will be provided in the following sections.

Table 2.3: Summary of 3-D printing techniques from [69].

3-D printing process	Techniques	Materials	Advantages	Limitations
Photopolymerisation	Stereolithography (SLA)	Photopolymers	Simple	Single material
	Continuous liquid interface printing (CLIP)	UV-curable resins	High-speed	Single material
	Two-photon polymerisation (2PP)	UV-curable resins	Sub-100 nm resolution	Low yield of production
Extrusion	Material jetting	Photopolymers	Multimaterial structures	High-cost
	Fused deposition modelling (FDM)	Thermoplastics, glass, metal	Simple, multimaterial structures, low cost	High-cost(for glass and metal)
	Direct ink writing (DIW)	Plastics, ceramic, living cells, composites	Versatile	Post-processing, low resolution
Powder-based	Selective laser sintering(SLS)	Thermoplastics, metals	No need for support material	High cost, limited mechanical properties
	Electron beam melting (EBM)	Metals	No need for support material	High cost
	Selective inhibition sintering (SIS)	Metals	Sintering is performed after printing, lower cost than laser-based methods	Low resolution, limited mechanical properties
	Selective laser melting (SLM)	Metals	No need for support material	High cost
Lamination	Laminated object manufacturing (LOM)	Paper, metal, plastic	Versatile	Design limitations, limited mechanical properties

Direct ink writing

DIW has emerged as one of the most flexible 3-D printing techniques applied to electrochemical devices due to its wide range of available materials. The flexibility in printing materials, ranging from highly viscous polymers to conductive suspensions, allows for superior freedom in the design choices of electrodes. This 3-D printing process is unique in its ability to extrude continuous filaments at room temperature, since the solidification of the printed filament does not rely on temperature like FDM for example, but on the rheological properties of the ink. DIW is only limited by the material class as long as the ink exhibits sufficient rheological properties like viscosity and viscoelastic properties.

The DIW process typically involves pressure-driven deposition of an ink on a substrate through a nozzle (process depicted in Figure 2.12a). As the ink is deposited on the substrate, its material properties change from viscous to a solid state through either solvent-induced phase changes, liquid evaporation, gelation or from temperature-induced phase changes. The resolution of the printed part is defined by the nozzle diameter, which depends on the composition of the ink. The composition of the ink is usually the most critical part of the printing process, as it determines the ink's printability and ability to retain shape. In general, the ink is suitable for use when it can be extruded continuously without jamming the nozzle and can be used to create three-dimensional structures according to the CAD-model. For the ink to fulfill these characteristics, shear-thinning behavior at multiple flow rates is necessary. Shear-thinning is a phenomenon characteristic of non-Newtonian fluids, where the fluid viscosity decreases with increasing shear stress. In this case, increasing shear stress is a result of an increasing pressure in the nozzle extruder. So, decreasing the deposition pressure can for example increase the extrudability of the ink. Once the ink has been discharged from the nozzle, it must undergo a quick transition from a shear-thinning ink to a solid filament to retain its shape. Inside the nozzle, a minimum amount of pressure needs to be applied to make sure that the ink remains in its shear-thinning state and retains a low viscosity. Low viscosity is necessary for smooth and continuous extrusion through the nozzle. Once deposited, the pressure (and shear stress) is removed, and the material transforms to a viscoelastic solid. At this moment, the printed material should have the right rheological properties for it to stay in its shape and remain solidified.

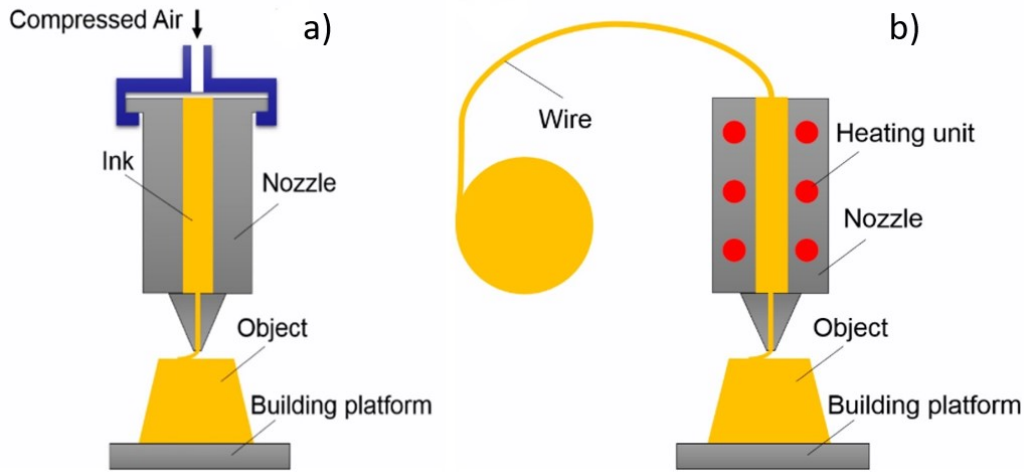


Figure 2.12: Schematic illustration of (a) DIW process and (b) FDM process [73].

The wide variety of available materials can lead to complicated process mechanisms for engineers. Especially, the optimization of the ink rheology can be a challenge. Controlling the rheology, which is achieved by adjusting the ink composition, is essential to obtain the desired resolution, geometry, and functionality of the printed component. Other challenges are the need for post-processing to enhance mechanical and electrical properties that could increase production time and cost. Furthermore, different materials are extruded under different conditions and currently no guidelines have been developed that correlate the material to the printing conditions. This makes it challenging for engineers to apply DIW to new developed materials, since extensive research is currently lacking in the industry. This is especially critical for newly developed composite materials. Introducing composite materials with (micro/nano)particles can also cause nozzle clogging. Nozzle clogging can result from the individual particles being too large or from particle agglomeration in the suspension.

Fused deposition modelling

Similar to DIW, FDM is another extrusion-based 3-D printing technique that uses a layer-by-layer deposition of polymer filaments. First, material (typically thermoplastics) will be fed via a system of rollers and gears to the extruder head, where the material will be heated until it reaches a semi-molten state. Once the semi-molten state is reached, material is deposited through a nozzle while the nozzle moves along a three-axis computer-controlled system. Once extruded, the material will land onto the print-bed and solidify to form a uniform solid layer which stacks on top of the previous layer according to the model design. Solidification of the polymer is based on polymer crystallization and cooling of the extruded polymer material. A schematic representation of an FDM printer can be seen in Figure 2.12b. The quality of printed parts can be controlled by altering printing parameters, such as layer thickness, printing temperature, printing orientation, raster width, print-bed temperature and raster angle. Apart from that, the quality of printed parts also depends on material parameters, such as viscosity, thermal conductivity, heat capacity and cooling rate. Today, FDM represents the most common 3-D printing technology due to the low complexity of fabrication, large size capabilities and availability of machines and material at affordable prices. Moreover, machine and software innovations have allowed easier user interaction as well as process optimization. Despite these advantages, there are certainly challenges that need to be considered when applying this 3-D printing technique. Compared to other 3-D printing techniques such as SLA, the surface of FDM-products is generally rougher with a resolution of around $100\text{ }\mu\text{m}$ compared to $<25\text{ }\mu\text{m}$ for SLA. So this requires surface treatments. In addition to that, the inter-facial adhesion between discrete layers can be poor during fabrication, which leads to anisotropic effects [74]. These effects can be partly tackled by adjusting process parameters such as part design, build orientation and applying post-processing [75, 76].

While initially based on the use of thermoplastics, the use of composite filaments has become widespread for improving mechanical, electrical, thermal, magnetic and dielectric properties. By adding (micro/nano)particles to the polymer matrix, one can introduce or enhance specific desired properties depending on the application. The use of conductive filaments especially has attracted a lot of attention from engineers for sensing

purposes. Incorporating electrically conductive particles into the polymer matrix can therefore enable the development of FDM-printed electrodes. There are now a number of commercial filaments available with conductive particles such as metals [77] while most of them are based on carbon particles [78–80]. However, when applying FDM to the fabrication of electronic component devices, engineers will face challenges inherent to the process of composite filament extrusion that need to be considered. Firstly, composite materials need to be in a filament form to enable the extrusion process of the printer. Therefore, polymer pellets need to be mixed with the (micro/nano)particles, which is done with the use of a solvent. Then, through a process called tape-casting, the mixture will be dried and cut into pieces. A filament extruder needs to be used to melt the composite pieces and fabricate the filament that can then be used for the FDM printer. This process can be seen in Figure 2.13. Alternatively, polymer powder could directly be melt blended with conductive powder in the filament extruder to obtain the composite filament. Next to that, engineers need to ensure a homogeneous dispersion of the particles, which is essential for having a good quality filament [81]. Attention should therefore be paid towards the mixing process of the composite during production. In addition to that, the viscosity of the filament needs to be high enough to provide structural support, but low enough to enable extrusion through the nozzle. The composition of the filament should therefore be carefully considered. Lastly, there is the risk of nozzle clogging. The nozzle may become clogged due to physical blockage of particle agglomerates during heating or due to excessive flow resistance caused by high viscosity. This will stop the extrusion process and can seriously damage the inside of the nozzle. Particle size and nozzle diameter are the main parameters affecting this problem [82].

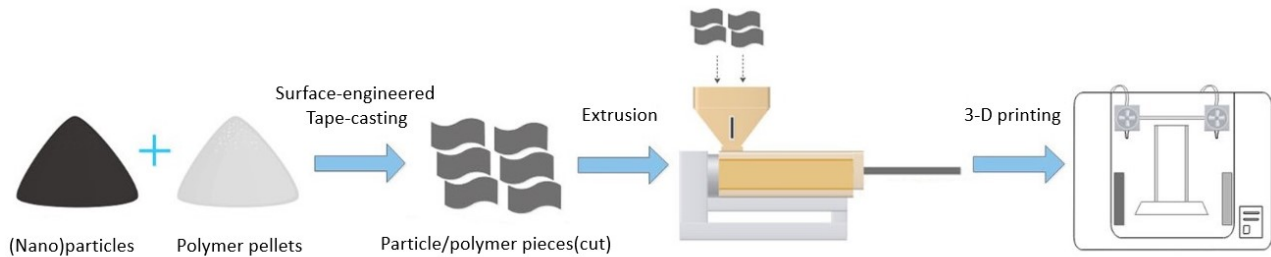


Figure 2.13: Process of manufacturing FDM composite filaments. Adopted from [83].

Stereolithography

In search of other methods to manufacture electrically conductive components, scientists have also looked at stereolithography (SLA) as a manufacturing method. SLA printing technique has widely been employed due to its advantages to manufacture objects with very high resolution and excellent surface quality. SLA-printed parts generally do not require post-treatment processes, depending on the application. During the printing process, a laser beam reaches a photocurable resin through reflection, then the photopolymer becomes polymerized and will be attached to the base. As the base is moving up or down (depending on the configuration), the photopolymer is polymerized layer by layer and starts to cure. This curing process induces solidification of the liquid photopolymer resin via cross-linking. For traditional SLA process, two configurations are possible. There is the bottom-up process [68]. A laser is placed above a base-platform which will be lowered in a reservoir filled with resin. The base-platform is lowered until only a thin layer of the resin is exposed to the surface. The laser will point downward and start curing the first layer, then the base-platform moves down to form the second layer and so on. The second process is called top-down process and works the exact opposite. Here, the laser is placed under the base-platform and will point upward as the base-platform is moving up so that resin can flow in between the reservoir and the base-platform.

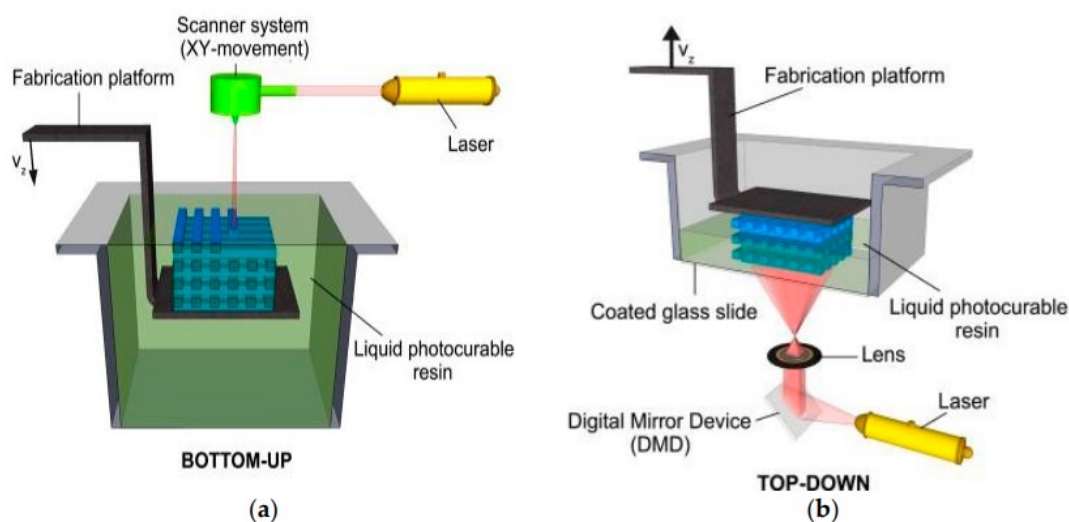


Figure 2.14: Schematic of the (a) bottom-up SLA method and (b) top-down SLA method [84].

SLA-printed objects have the highest printing resolution compared to other methods, such as FDM or DIW. While these available 3-D printers are limited to resolutions ranging from 50-1000 μm , SLA printers can print resolutions of around 25 μm [68]. Despite these advantages, SLA-based machines do have their drawbacks. SLA machines can have a slow building speed, which is a direct result of the curing process. Even though each layer can be formed quickly by the laser, the process of initiating a new layer generally takes a significant amount of time. Since the resolution of SLA-machines is high, more layers need to be used to cover the object's dimensions compared to other AM-techniques, which also increases printing time. Even though SLA-machines can be purchased quite cheaply, the photoreactive resins are still costly. Furthermore, resulting from constantly expanding research and development in AM-materials, a wide range of curable materials for SLA-machines has so far been developed. Still, most commercially available resins are developed for prototyping purposes only and do not retain the functional properties for industrial applications [85]. The materials are susceptible to creep, have limited impact strength and durability. Also, mechanical properties degrade over time as a result of UV degradation. So, commercially available resins currently lack sufficient mechanical, electrical, biocompatible and thermal properties for them to be effective. Nevertheless, by introducing (micro/nano)particles in the photopolymer resin, new potentials can be discovered which will expand their field of application.

Composite resins offer the potential for improved properties, however introduction of (micro/nano)particles in the resin can be complicated and cause challenges [85]. Small amounts of particles can seriously affect the viscosity of the resin. A higher viscosity will require increased curing times and decrease processability of the resin. Other encountered problems are dispersion and agglomerate formations. Many (micro/nano)particles are incompatible with resins, even at small loadings. Particles can form agglomerates, limiting the print resolution and printability. At the same time, (micro/nano)particles will also affect the polymerization efficiency of the resin due to the occurrence of UV absorption by the particles. High concentrations of these materials decrease the UV transmission depth through the resin and will lead to incomplete curing of the material, jeopardizing the material quality. Increasing the UV intensity and lowering the loading of particles are possible solutions to retain material quality.

2.2.3 Carbon-based printed electrodes

DIW printed carbon-based electrodes

Researchers have started to experiment with conductive inks for potential electronic device design. DIW has also been applied to manufacture different 3-D printed electrically conductive components like supercapacitors or electrodes. Various types of materials have been used to enable electrical conductivity in the ink solution. Great success has been achieved by using polymer composites that contain carbon-based materials

like graphene, carbon nanotubes (CNTs) or graphene oxide (GO). GO shows excellent rheological properties when dispersed in water, which is important for extrusion. Due to low-cost and simple implementation, incorporating conductive particles in polymer bulk materials has also widely been explored for property enhancements in DIW. In a recent study, Wang et al. [86] have manufactured high performance supercapacitors from a novel polyaniline (PANI)/GO ink which showed good shape retention and smooth extrusion. The ink was prepared by mixing GO and PANI in a solvent of water and N-Methyl-2-pyrrolidone (NMP), see Figure 2.15(a). Four types of ink were prepared with different mixing ratios to test the dispersibility, extrusion, object molding and the rheological properties during 3-D printing process. They manufactured macro-sized electrodes for construction of their supercapacitors, see Figure 2.15B. The electrodes were after printing dispersed in a hydroiodic acid bath for 30 min to convert the GO to reduced GO, which increases the electrical conductivity and mechanical strength. To test further practical application of the ink, various architectures including 3-D honeycomb and column lattices were printed on a substrate and each showed good resolution and shape retention. Also, the achieved printing resolution was reported to be around $300\text{ }\mu\text{m}$. Their planar supercapacitor also showed good capacitance retention after 1000 cycles, by reducing to 75% of the initial capacitance. The researchers concluded that 3-D printed PANI/RGO is a promising electrode material for fabrication of future electrical components.

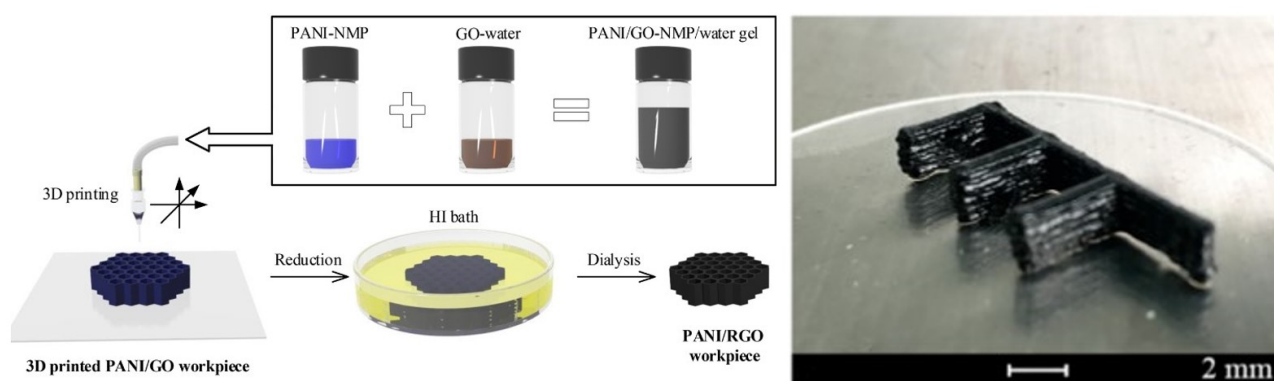


Figure 2.15: (a) Preparation of PANI/GO ink and fabrication. (b) Photo of printed electrodes. [86]

Other carbon-based materials like graphene have also been reported to be used as additives to polymeric composite inks for property enhancements. A 3-D printable biopolymer composite was manufactured by Jakus and colleagues [87] which consists of graphene and a bio-compatible elastomer (polylactide-co-glycolide). The manufactured ink was utilized at ambient temperatures via extrusion based 3-D printing and created graphene structures ranging from only a few layers ($<300\text{ }\mu\text{m}$ thin object) to hundreds of layers ($>10\text{ cm}$ thick object) with good precision and fidelity. An average printing resolution was reported between $100\text{ }\mu\text{m}$ and $1000\text{ }\mu\text{m}$. Three types of ink were tested in this study, each with a different graphene-to-polymer ratio, 75 wt.%, 56 wt.% and 32 wt.% graphene. The composite displayed high electrical conductivity and was mechanically flexible, bio-compatible, and biodegradable, see Figure 2.16. It was therefore concluded that this composite was highly suitable for practical applications like nerve tissue engineering.

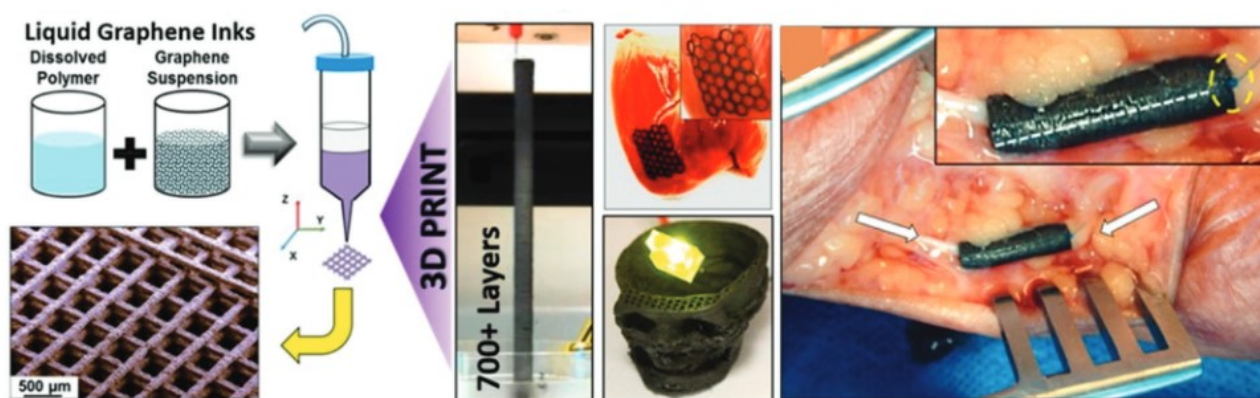


Figure 2.16: Process of composite fabrication (left), photo of a tubular 3-D printed specimen used as nerve conduit (right) [87].

FDM printed carbon-based electrodes

In recent years, along with the development of 3-D printing technology and composite filaments, FDM printing of electric energy sensing (EES) devices has undergone rapid development, in the meantime, more and more commercial filaments with conductive fillers have entered the market. Especially, filaments with carbon-based particles have been introduced as good candidates for printing conductive electrodes. Carbon-based particles such as MWCNT [83, 88–92], CNT [93–97], (r-)GO [98, 99], carbon black (CB) [100–103], nanographite (NG) [104, 105] and nanocarbon (NC) [106] have been reported to function well as electrically conductive particles for 3-D printed electrodes. Hybrid filler contents have also been applied such as CNF with graphite flakes [107], graphene with CNT and graphene with CB [103].

The following paragraph will highlight multiple interesting and novel researches that have taken place with respect to conductive carbon-based printed electrodes. Various papers have been reporting experiments, investigating the electrical conductivity and resistance of carbon-based printed electrodes; Foster and colleagues [105] fabricated various macroelectrodes from a NG loaded PLA filament with concentrations of 1–40 wt.%. The main purpose was to investigate the printability and electrical conductivity of high-loaded nanocomposite filaments (see Figure 2.17a). In terms of printability, it became apparent that loadings above the 25 wt.% were too brittle and could not produce a functional 3-D printed electrode. With 25 wt.% of NG, a conductivity was achieved of around 1.25 S/m. Wei and colleagues [98] manufactured a composite electrode from GO with PLA and investigated the conductivity and printability for multiple weight percentages of the filler. The GO particles had lateral sizes of around 3–4 μm and concentrations were ranging from 0.4–7.4 wt.%. The highest GO-loaded printable composite (5.6 wt.%) bears a conductivity of 0.00105 S/m (see Figure 2.17b). Due to discontinuous extrusion, no parts were successfully printed for a weight percentage of 7.4% and above. Possibly due to particle agglomeration, the nozzle was blocked, which restricted extrusion of the material. Kennedy et al. [89] produced highly-conductive polyvinylidene fluoride (PVDF) and MWCNT composites as filament feed stock for 3-D printing of sensing strips. The printed composites contained between 1–15 wt.% of MWCNT and were easily extruded from a 0.8 mm steel nozzle, even at 15 wt.% of MWCNT. The highest recorded conductivity was ~3 S/m for 15 wt.% of MWCNT. Other researchers have reported conductive filaments with higher weight percentages of nanoparticles for electrode manufacturing. A significantly high conductivity of ~200 S/m, was achieved by Kwok et al. [102] who used thermoplastic composite filaments based on polypropylene (PP) as polymeric matrix and CB as conductive filler. They used a high wt.% of CB between 1–40 wt.% where the highest conductivity was achieved by 40 wt.% of CB. Their study also focused on the durability of the printed electrodes. They reported stable electrical properties of the electrode under exposure of sunlight for 1 month and no observable degradation in electrical resistance when used at 12 V (AC) for 7 days.

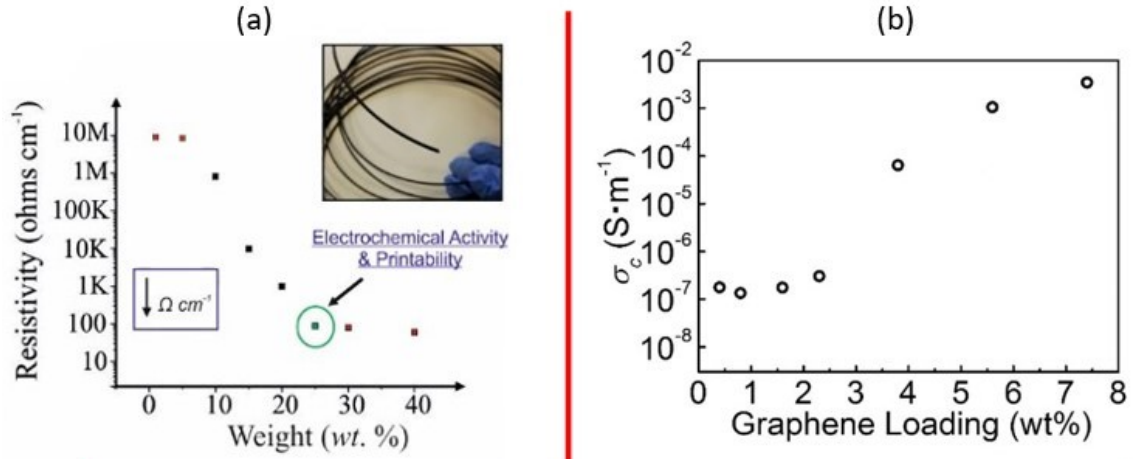


Figure 2.17: (a) Electrical resistivity for 3-D printed electrode as a function of NG concentration, from [105].
 (b) Electrical conductivity for 3-D printed electrode as a function of graphene loadings [98].

More studies reported embrittlement of the composite electrode material while increasing the weight percentage of carbon-based particles. Dorigato et al. [88] reported a significant reduction in elongation at break, from 35.4 % to 1.8 % while increasing the MWCNT concentration in an ABS composite from 0 to 15 wt.%. Also, this research investigated the effect on electrical and mechanical properties of the electrodes, considering horizontal, vertical, and perpendicular printing orientations. Especially, a visible effect of the printing orientations was noticed after investigating the mechanical properties such as strain and yield strength. Lastly, it was reported that higher filler concentrations resulted in an increased yield strength and stiffness. Another paper published by Ye et al. [96] similarly noticed that higher CNT concentrations in the polymer (PEEK) exhibited more brittle behavior (reduced elongation at break). Starting with 11.5% with no nanoparticles and decreasing to about 7% for 7 wt.% of CNT. In addition to that, Ye and colleagues reported increased tensile strengths and elastic modulus of the PEEK/CNTs composite when increasing nano reinforcement content. The tensile strength and elastic modulus of the printed sample containing 7 wt.% of CNTs increased by 27.8% and 17%, respectively. Another paper also reported higher tensile strengths while increasing carbon-particle concentrations [94]. Other researches however reported decreasing tensile strengths [97, 108–110]. This can generally occur when there is a non-homogeneous dispersion of the nanoparticles in the polymer, which results in particle agglomerations. Limited adhesion between the particles and polymer matrix has also been reported by Masarra and colleagues as a cause, since it will weaken the bonding forces. Lastly, this decrease could also be due to the location of the particles at the surface of the filaments, which can enhance the delamination of the 3-D printed adjacent layers. Potnuru and colleagues observed similar behavior regarding the tensile strength for increasing NC concentrations. Embrittlement of the filament with increasing NC concentrations was also observed by cleaner cuts for 9% and 15% NC. Gao et al. [111] more specifically investigated the effect of filler concentration on tensile strength. They reported that for lower particle concentrations (1 wt.% - 7 wt.%) the tensile strength increased with respect to the bulk polymer and that for higher concentrations (>7 wt.%), the tensile strength immediately decreased, possibly due to particle aggregation. Embrittlement of the composite material was also reported, as the strain at break decreased from 11.2% to 3.4% for 10 wt.% of GNP.

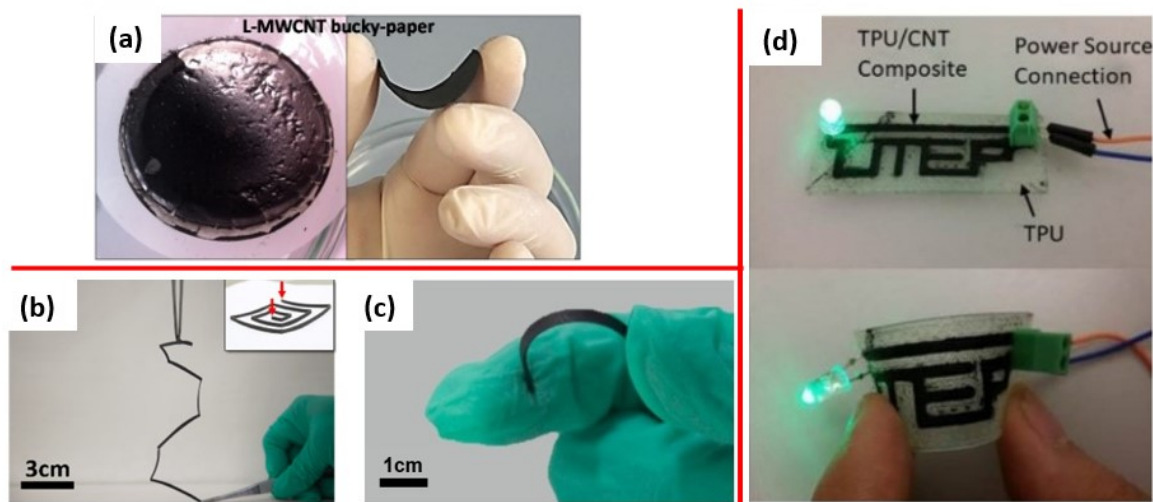


Figure 2.18: (a) Example of 3-D printed flexible paper [91]. (b) Stretching of 3-D printed circuit.[99]. (c) 3-D printed flexible electrode [99]. (d) Example of 3-D printed flexible circuit [103].

Introducing particles in the polymer matrix to achieve sufficient conductivity also affects the mechanical properties, such as tensile strength and elastic modulus. Reduction of elongation is yet another negative effect which will make the material brittle. In order to manufacture flexible electrodes, embrittlement of the material is not desired, but will be inevitable when using higher concentrations of fillers to achieve conductivity. Maurel and colleagues [112] manufactured highly loaded graphite-PLA electrodes to be used in a lithium-ion battery. In order to prevent embrittlement of the composite, plasticizers were added to the composite to provide the necessary flexibility of the electrode. The printed samples were loaded with around 60 wt.% of graphite powder and various concentrations of plasticizer were added to determine the optimal composition to ensure flexibility. A weight composition of 26.8/62.5/10.7 (PLA/graphite/plasticizer) resulted in a conductivity of ~ 20 S/m at ambient temperature. In addition to that, the authors included additional CNF and CB particles in the filament to increase the conductivity. Subsequently, a conductivity of ~ 50 S/m was obtained for a 10 wt.% CB loaded electrode. Other papers have achieved flexible electrodes by lowering the carbon filler content. Zhang et al. [99] printed flexible PLA/r-GO (1-8 wt.%) electrodes and investigated the mechanical and electrical properties (see Figure 2.18c). More specifically, the effect of bending and stretching on the conductivity of the electrode was studied. They reported that after an elongation of 2.5%, the conductivity quickly decreased by a factor 10^5 . In addition to that, the authors measured the conductivity of three different samples after blending the PLA with graphene. They concluded that the conductivity of each sample increased after each extrusion process, which ensured a more homogeneous allocation of the graphene particles.

SLA printed carbon-based electrodes

Introducing (micro/nano)particles in polymer resins has been a promising method to obtain composite resin materials with enhanced properties. Recently, various researchers have introduced carbon-based particles such as carbon fibers and GO for mechanical property enhancements. Manapat and colleagues [113] used a polymer composite with 1.5 wt.% GO to enhance tensile strength and tensile modulus. Lin et al. [114] also introduced GO with a 0.2 wt.% to a resin solution to increase the tensile strength and elongation. Other mechanical properties like compression strength have also been increased by adding nanoparticles to a polymer material. Xiao and colleagues [115] added a mixture of carbon fibres (CNF) and GO of up to 1.4 wt.% to a photopolymer dispersion. They achieved an increase of the compression strength by over 10 times compared to the bulk photopolymer. More interestingly, introducing carbon-based particles in polymers can also be used for electronic device design by increasing electrical conductivity. Gonzalez et al. [116] studied the effect of CNT concentration on the mechanical and electrical properties of multiple PEGDA/PEGMEMA composite printed parts (Figure 2.19b and Figure 2.19d). The thickness was reported to be 3 mm. CNT concentrations up to 1 wt.% were applied to the resin, where the optimal concentration for printing was 0.3 wt.%. Higher

loadings of CNT resulted in a decrease in photopolymerisation due to the high UV absorption of the CNT particles, which decreases cross-linking in the resin and printing resolution. It was suggested that this problem can be overcome by increasing the UV intensity of the light source or decrease particle concentration. In addition, mechanical tests concluded that at first an increase in CNT concentration increases tensile strength but after 0.5 wt.% significantly decreases, see Figure 2.19a. The researchers reported that a conductivity of around 0.4 S/m was reached for 1 wt.% of CNT (Figure 2.19c).

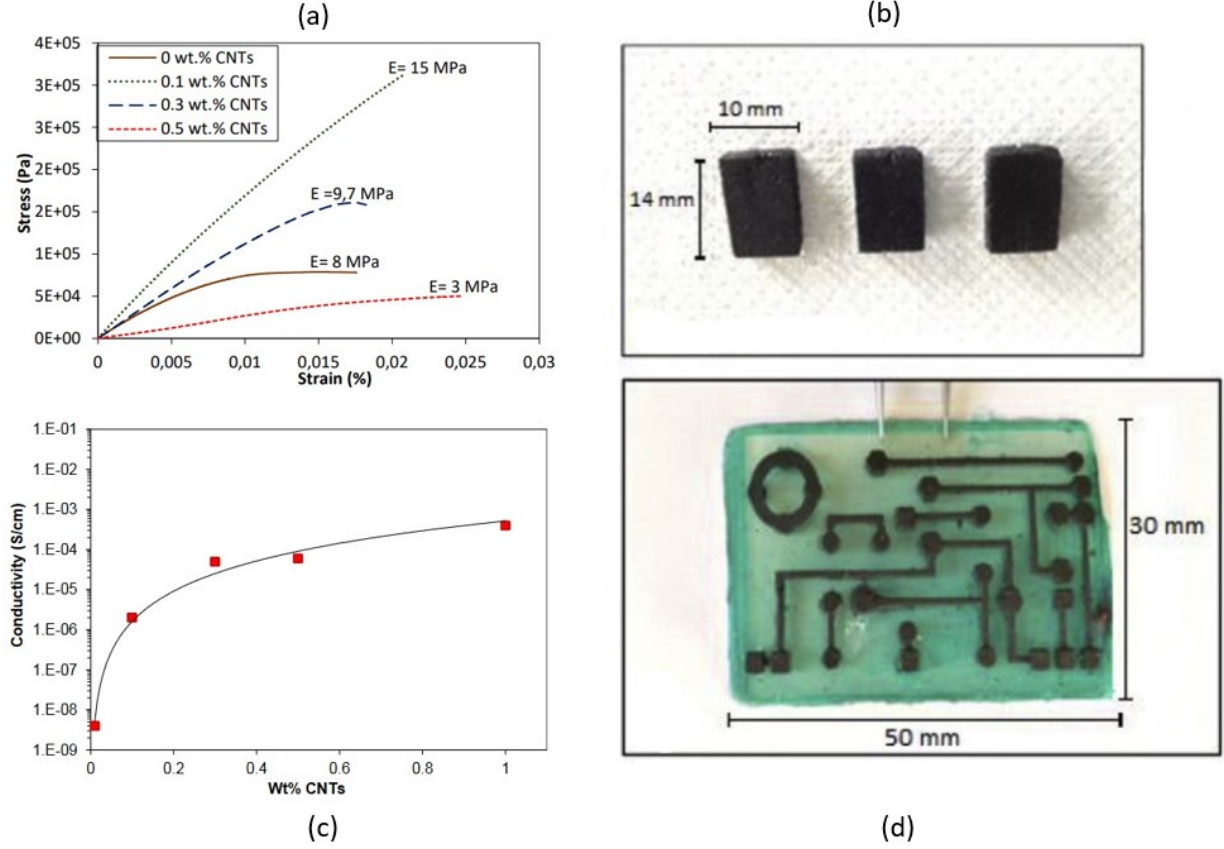


Figure 2.19: (a) Tensile test for resin formulations with different CNT concentrations. (b) 3-D printed cubes used for conductivity tests. (c) Electrical conductivity for 3-D printed cube as a function of CNT concentration. (d) Circuit-like structure built on insulating plate.[116]

Mu et al. [117] used an SLA-printer to prepare and investigate electrically conductive polymer nanocomposites. The ink was a mixture of an acrylic-based photoreactive resin with various concentrations of MWCNT from 0.1 wt.% to 0.6 wt.%. The concentrations of MWCNT were investigated to yield the best printing quality and optimal conductivity. They concluded that increasing MWCNT concentrations above the 0.3 wt.% already compromised the printing quality due to the viscosity of the ink. Different structures were printed such as electrodes, hollow capacitors and stretchable circuits to demonstrate the versatility of the ink, shown in Figure 2.20b and Figure 2.20c. Conductivity experiments showed that a maximum conductivity of around $2 \cdot 10^{-4}$ S/cm was achieved for 0.6 wt.% of MWCNT, as shown in Figure 2.20a. Moreover, mechanical performance experiments concluded that an addition of MWCNT could increase the tensile stress and the tensile modulus. On the other hand, a slight decrease in the elongation of break was also observed.

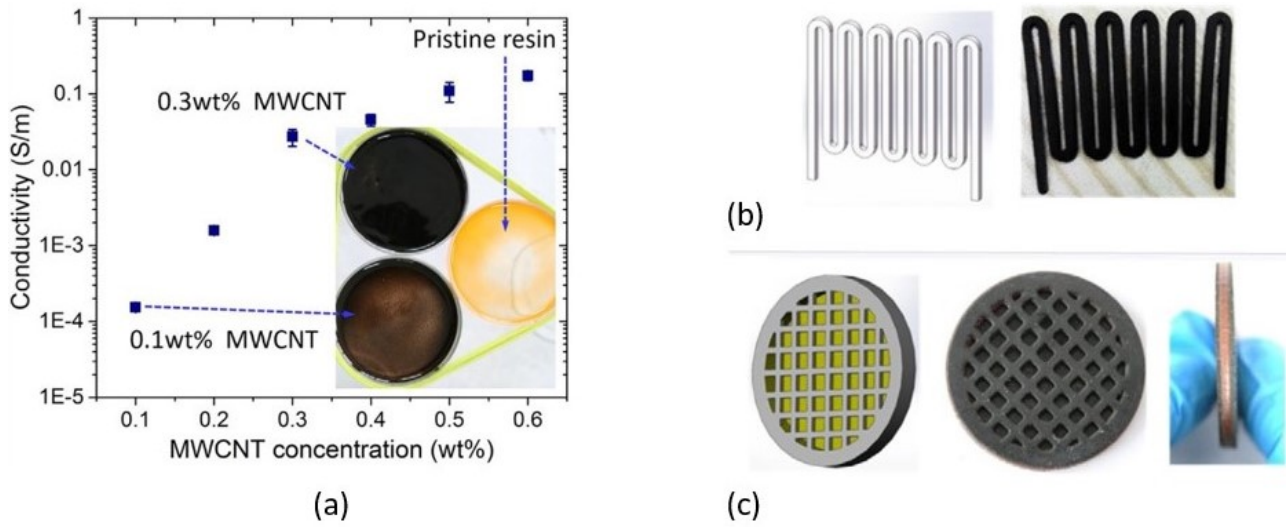


Figure 2.20: (a) Electrical conductivity for 3-D printed structures as a function of MWCNT concentration. (b) 3-D printed planar wave shape resistor. (c) 3-D printed capacitor with hollow structure.[117]

2.2.4 Diamond-based printed composites

Research papers that have mentioned the use of BDD for 3-D printed electronic components are very limited. Only one paper that has been published used BDD particles for the fabrication of a humidity sensor through 3-D printing. For this reason, the following section will report not only the use of BDD particles for 3-D printing purposes, but also undoped diamond particles that have been used for 3-D printing fabrication. Through this way, more knowledge can be gathered on the practical use of diamond particles for 3-D printing applications.

BDD-based printed electrodes

Kalsoom and colleagues [118] are currently the only known research group who have used BDD particles for 3-D printing electrical component applications. They developed a novel 3-D printable composite consisting of BDD (60 wt.%), LiCl (2 wt.%) and ABS. The developed composite material was employed for simple and quick fabrication of the humidity sensor using a low cost fused deposition modeling (FDM) 3-D printer. The BDD particles were included to act as electrode material that can attain high stability, and LiCl was employed as electrolyte material for sensing applications. The authors reported that a uniform distribution of the fillers and connectivity is crucial to attain the desired properties of the sensor. Weight percentages higher than 60 wt.% resulted in fragile and mechanically unstable filaments. To better understand the composite properties and the role of LiCl in improving the connectivity and electrical conductivity of the composite, ABS with BDD, ABS with undoped microdiamond and ABS with undoped microdiamond and LiCl were also studied for humidity sensing and electrical conductivity. Interestingly, they found that the electrically conductive properties of the ABS with BDD electrodes were found negligible, which confirms poor connectivity of the BDD particles in the polymer matrix due to signal interruption by the presence of a thin ABS layer on the BDD. Therefore, they concluded that the addition of

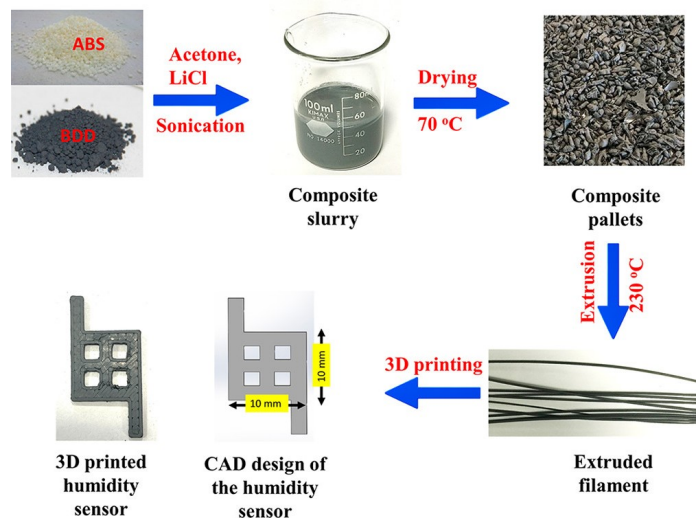


Figure 2.21: Schematic illustration of manufacturing process for 3-D printed, BDD-based humidity sensor [118].

LiCl was vital to accomplish the desired electrically conductive properties of the composite. SEM analysis was performed to verify the connectivity and distribution of the BDD particles in ABS with and without LiCl, see Figure 2.22. The authors also reported that an increased nozzle diameter was necessary together with an increased printing temperature, which had been raised to about 245 °C to avoid blockage and ensure a fluent material deposition.

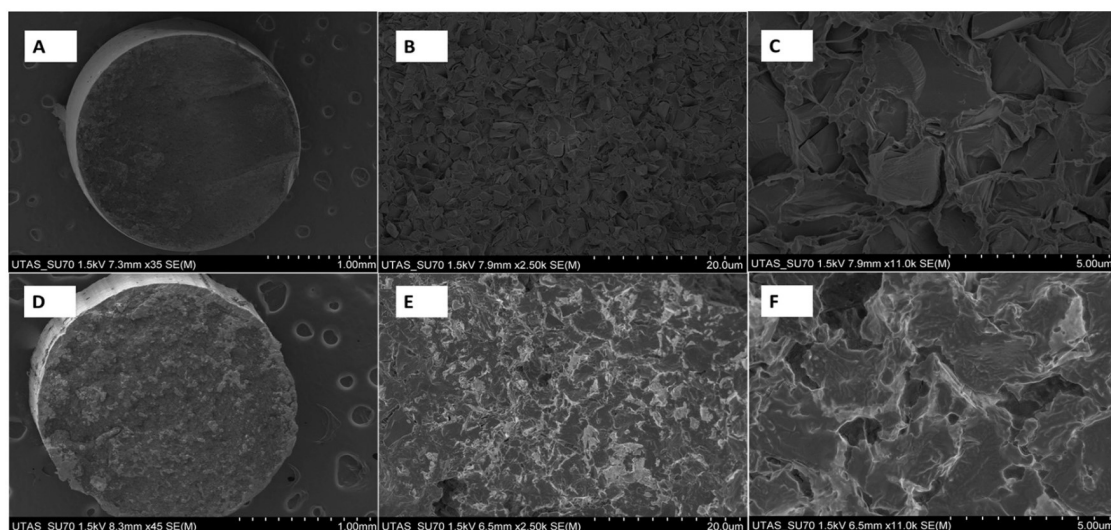


Figure 2.22: SEM images of ABS-BDD (a-c) and ABS-BDD-LiCl (d-f) composite filament cross-section [118].

Other diamond-based printed materials

Several researchers have used microdiamond reinforcements to improve thermal and mechanical properties. Waheed et al. [119] investigated the thermal and mechanical properties of an FDM printed ABS with microdiamond composite filament. The composite ABS filament with concentrations of 37.5 wt.% and 60 wt.% were manufactured through blending of the two materials and extrusion of the composite to produce the filament. Filaments extruded only once were shown brittle and had a porous and rough surface. They had an inconsistent diameter, reflecting the nonuniform distribution of the diamond particles. Subsequently, the filaments were cut into pieces again and re-extruded. This process was repeated six times and after that the surface was smooth, dense and showed no visible pores. These results can be seen in Figure 2.23. Additionally, the incorporation of synthetic microdiamonds significantly improved the thermal conductivity by more than a five-fold compared to ABS (for 60 wt.%). More importantly, their investigation also reported that the elongation at break was reduced significantly compared to ABS itself, from 4.23% to 1.70%. Still, mechanical properties were also improved by the addition of microdiamonds. The elastic modulus for the 60 wt.% composite increased by 41.9% with respect to pure ABS.

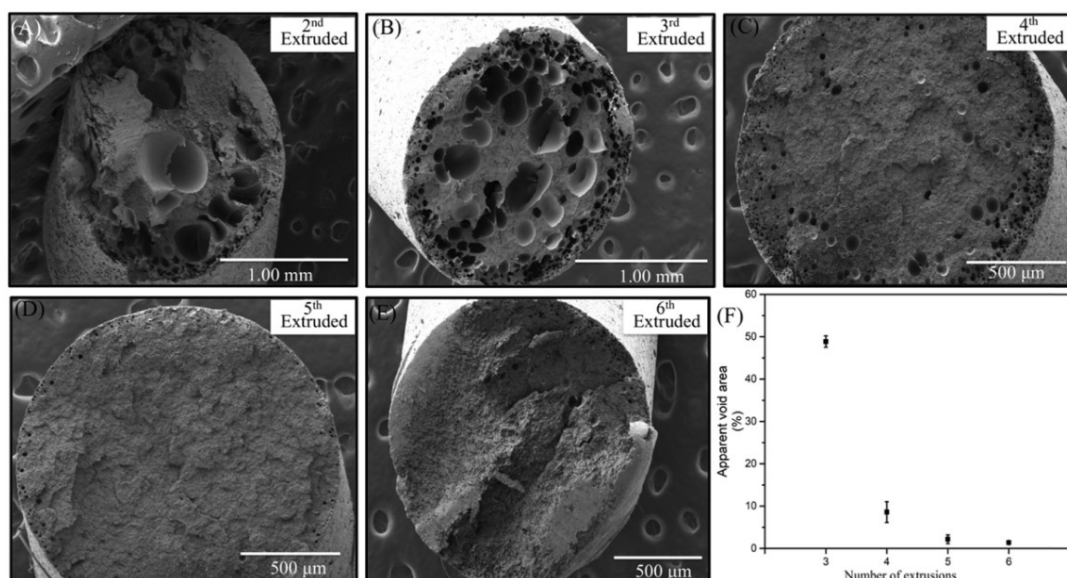


Figure 2.23: (A-E) SEM images of cross-section of second to sixth-time extruded filament. (F) Void area for the second to sixth-time extruded filaments.[119]

Another study conducted by Kalsoom et al. [120] similarly focused on introducing microdiamond particles in a polymer. Here, an SLA-based 3-D printing method was used to fabricate thermally conducting composite materials, see Figure 2.24. The composites containing 10, 20, 25 and 30% (w/v) of 2-4 μm sized synthetic diamond particles were mixed with an acrylate based photopolymer. High concentrations (30%) of microdiamond resulted in a substantial improvement (more than 200%) in the heat transfer efficiency of the composite.

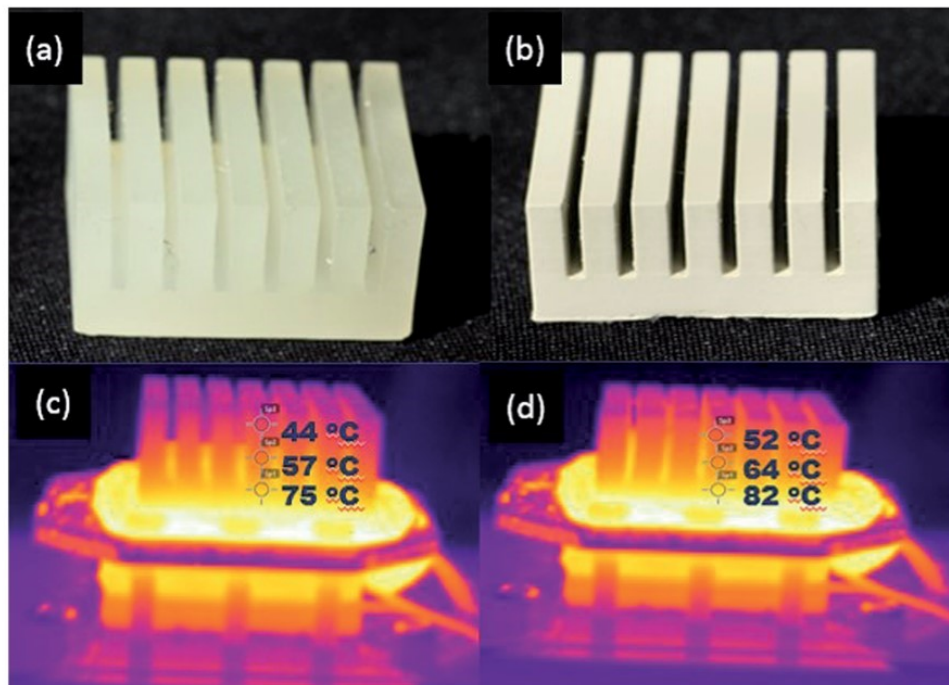


Figure 2.24: (a) 3-D printed heat sink using commercial acrylate resin, (b) 3-D printed heat sink using 30% (w/v) composite material, (c) IR images of polymer heat sink heated for 10 min at 100 °C, (d) IR image of composite heat sink heated for 10 min at 100 °C [120].

3 Knowledge Gap and Research Objective

3.1 Knowledge gap

Current research in the field of 3-D printed electrodes has mostly focused on the use of carbon-based additives such as CNTs, graphene and carbon black (CB). No studies have reported the use of BDD particles for property enhancement in flexible polymer composites. Only a handful of papers reported the use of undoped diamond for their research. No reports have also been published on the fabrication and use of flexible 3-D printed electrodes for electrochemical applications. These factors create the following knowledge gaps:

- There is no scientific literature on the use of BDD particles for flexible 3-D printed electrodes.
- There is no scientific literature on the use of flexible 3-D printed electrodes for electrochemical applications.
- The effect of diamond particles on the mechanical properties of flexible 3-D printed composites is not yet explored in detail.

3.2 Research objective

This research aims to investigate the possibility to manufacture flexible BDD-based electrodes through 3-D printing techniques. Two 3-D printing techniques, SLA and FDM, will be used to investigate the production of BDD composite electrodes. Iterative optimization rounds will be applied to produce electrodes with desired electrical and electrochemical properties, and at the same time attain a good degree of flexibility. Different concentrations of BDD powders will be mixed with various types of polymers (also including CNT fillers) to find the most effective composition. The electrical, electrochemical and mechanical properties of the developed electrodes will be studied through a set of experiments to characterize their performance.

This research aims to achieve a novel, straightforward approach for the preparation of flexible BDD-based electrodes using 3-D printing techniques which can remove existing barriers in the manufacturing process. This method should simplify the production and be significantly less time-consuming than current manufacturing techniques based on chemical vapor deposition. In addition, 3-D printing allows for additive manufacturing instead of existent subtractive manufacturing, which may contribute to a more sustainable fabrication.

3.3 Research questions

Main research question: “How can 3-D printing be used to manufacture flexible and conductive diamond-polymer composite electrodes for sensing applications?”

Sub-questions:

- How does the filler content affect the mechanical properties of as-printed diamond-polymer composites?
- How does the choice of 3-D printing technique affect the maximum wt.% of particles to be added?
- What is the effect of BDD particles on the electrical and electrochemical behavior of as-printed, CNT-containing electrodes?
- How does the printing technique affect the need for surface modification (post-processing)?
- What effects do post-treatment processes have on the structural integrity and electrical conductivity?

4 Materials and Methods

4.1 Chemicals

Prusament Flex80 transparent resin, a commercially available acrylate resin, was purchased from Prusa Research, Czech Republic. Thermoplastic polyurethane (TPU) pellets (5 mm) were supplied by 123-3D.nl, The Netherlands, and used as received. Low-doped (300-500 ppm) BDD powder (1 μm) was obtained from Boromond, China. Higher doped (710 ppm) BDD powder (< 0.5 μm) was purchased from UHD Ultrahard Tools Co., Ltd, China. Both powders were not treated and used as received (Figure 4.1). Multi-Walled Carbon Nanotubes (MWCNTs) NC7000 and TPU-MWCNTs composite masterbatches (10 wt.%), Plasticyl TPU1001, were purchased from Nanocyl SA., Belgium. Hexaammineruthenium(III) chloride ($\geq 98.0\%$), potassium hexacyanoferrate(III) ($\geq 99.0\%$), phosphate buffered saline (powder, pH 7.4), sulfuric acid (96.0 %), potassium nitrite ($\geq 99.0\%$) dopamine hydrochloride ($\geq 98.0\%$), dimethylformamide (DMF) (99.5 %), acetone and isopropanol were purchased from Sigma Aldrich, The Netherlands.

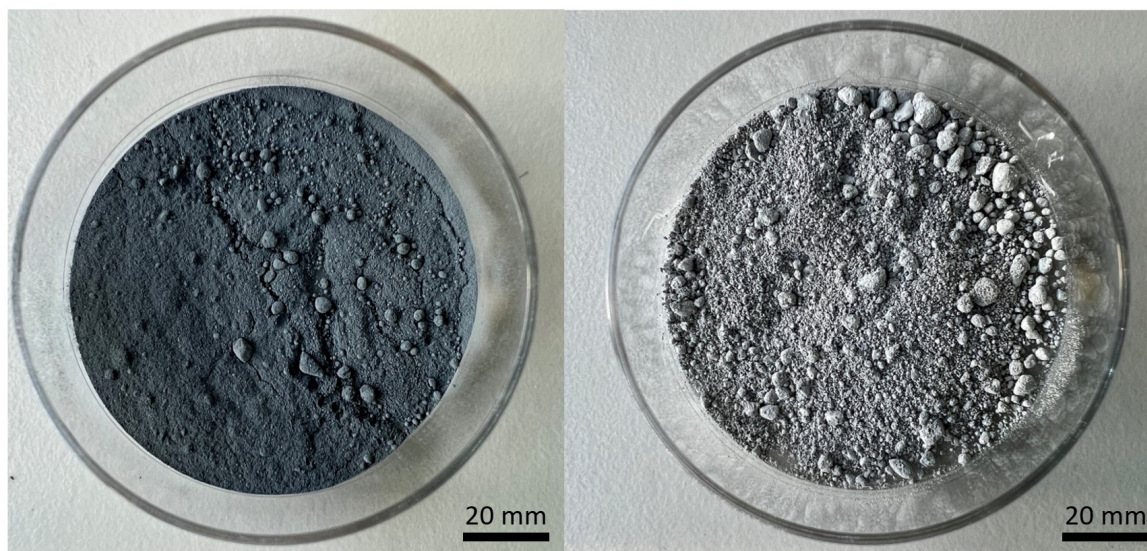


Figure 4.1: Optical images of Ultrahard BDD powder (left) and Boromond BDD powder (right).

4.2 Composite preparation

4.2.1 SLA-based composites

Prusament Flex80 transparent resin was used for the preparation of the SLA-based composites. Diamond-resin composites consisting of 2.5 to 12.5 wt.% were prepared by adding appropriate amounts of powder to the resin. Powders were, prior to addition to the resin, crushed to reduce the existence of aggregates before mixing with the resin. The composite mixtures were magnetically stirred for 90 min at 200 – 300 revolutions per minute (rpm) to promote homogeneous dispersion of the particles. After that, the mixture was sonicated for 30 min at 100 % power using a Branson 1800 Ultrasonic Bath 40 kHz to further disperse the BDD microparticles and to disintegrate aggregated particles. At last, the composite mixture was again magnetically stirred for 60 min to evenly distribute the settled particles on the bottom of the glassware resulting from the sonication process. Once prepared, the composite resin formulations were used for printing without any

modifications, but stored in tinted glass bottles at room temperature to prevent early polymerization. An overview of the preparation process is presented in Figure 4.2. The diamond-resin composites containing Boromond BDD powder are named BDR-X, where X represents the wt.% of BDD powder. The diamond-resin composites containing Ultrahard BDD powder are named UDR-X, where X represents the wt.% of BDD powder.

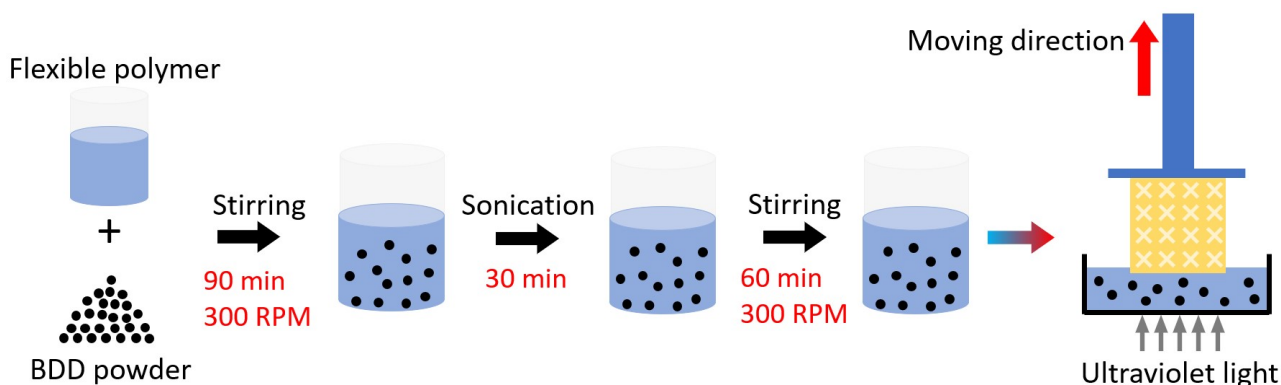


Figure 4.2: Schematic drawing of the preparation and printing procedure of SLA-based composites.

Prior to the SLA-printing procedure with the diamond-polymer composites, an optimization process was performed to investigate the feasibility of different BDD weight percentages. Multiple molds were manufactured that were each filled with different compositions of BDD-resin. Then, these molds were placed in different UV-curing machines, which used different wavelengths, for different time periods. The results of these experiments can be found in Table A.1. These results provided a solid starting point for the fabrication of the composite resins through 3-D printing. On the basis of these results, different compositions of BDD powder with resin were formulated, which were then used to print the BDR and UDR electrode samples. An overview of the experiments related to the optimization of the 3-D printing procedure can be found in Table A.2. For each BDD powder, three different BDD-resin compositions were formulated, where the highest weight percentage represented the limit of what was printable. BDR-5, BDR-10 and BDR-12.5 were prepared using the Boromond BDD powder, and UDR-2.5, UDR-5 and UDR-7.5 using the Ultrahard BDD powder.

4.2.2 FDM-based composites

Composite pellet fabrication

TPU/BDD and TPU/CNT/BDD composite pellets were fabricated using the following experimental procedure. First, TPU pellets were dissolved in DMF using a 1:10 (g/ml) ratio and magnetically stirred for 2 hours between 400-500 rpm at 60 °C. After all TPU pellets were dissolved, BDD powder was slowly added to the solution and magnetically stirred for 2 hours under the same conditions as mentioned before. Then, the composite solution was ultrasonicated using an Emag Emmi-60 HC 45 kHz operated at 100% power for 1 hour. After that, the composite solution was left stirring overnight at 500 rpm without heating to ensure a good homogeneity. The solution was then precipitated in deionized water to obtain composite “precipitates”. Precipitate formation is based on non-solvent induced phase separation [121]. It involves the formation of two phases through an exchange of the solvent from the polymer solution to a non-solvent, from which precipitation of the polymer occurs. The precipitates were dried in an oven at 165 °C for 2 hours to evaporate any remaining traces of DMF and water. At last, the dried composites were manually cut into 10-20 mm sized pellets, which were later used for extrusion. A schematic overview of the process is presented in Figure 4.3.

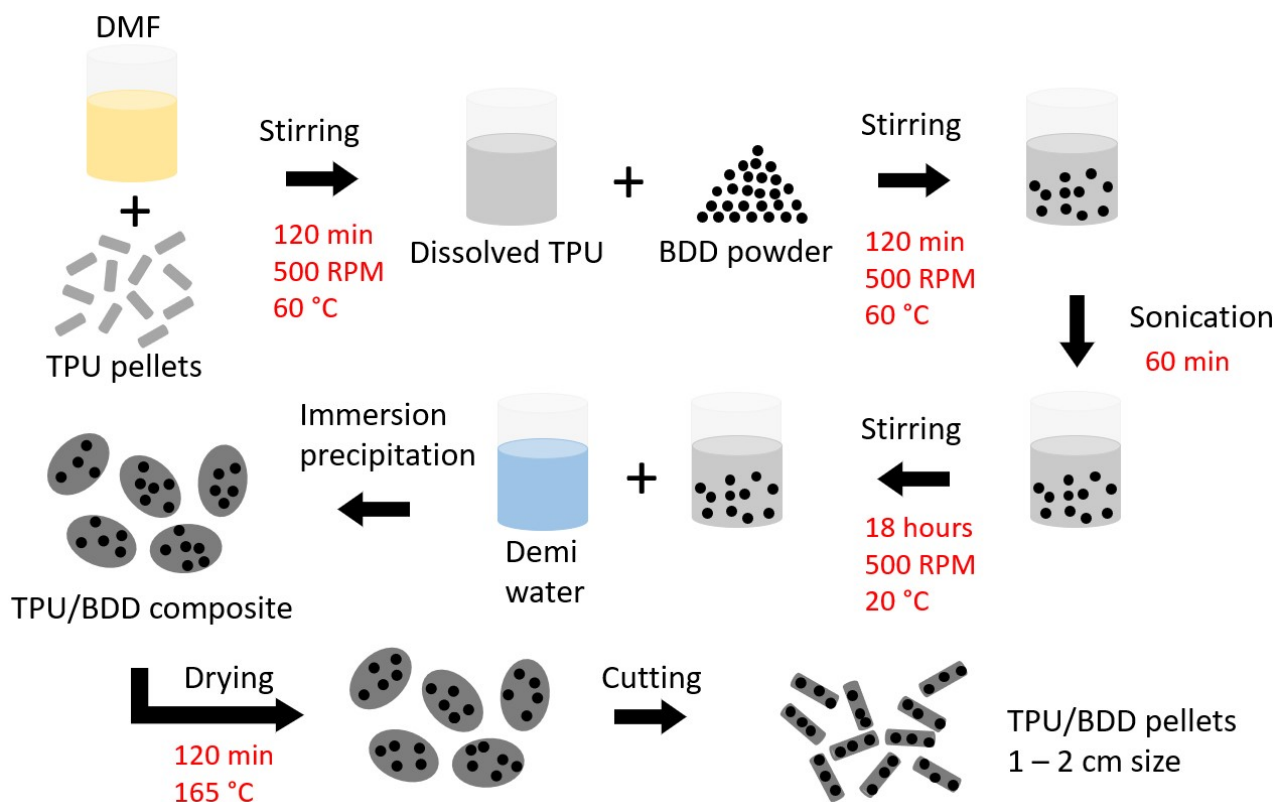


Figure 4.3: Schematic illustration of the preparation procedure for FDM-based composite pellets.

Composite filament fabrication

Composite pellets were extruded using a single-screw Felfil Evo extruding machine (Felfil srl, Italy), consisting of a controllable extruding temperature, and controlled extrusion speed or flow rate. To control the filament diameter, the extruded filament while still hot, was guided over a set of cooling fans to a spooling machine, consisting of a stepping motor to ensure stable speed and diameter. A schematic of the extruding set-up is presented in Figure 4.4. Occasionally, the filament was manually pulled out of the extruder machine to gain better control over the filament diameter. The extrusion temperature was set between 195–215 °C. The extrusion speed was set to 3–5 rpm and the speed of the puller was set to 0.4–0.6 m/minute. The extruded filament was manually cut into smaller pieces which were 10–20 mm in length and re-extruded. This process was repeated multiple times until the filament was dense, and showed no presence of porosity [119]. Extruded filaments used for printing were ranging in diameter from 1.55 to 1.70 mm.

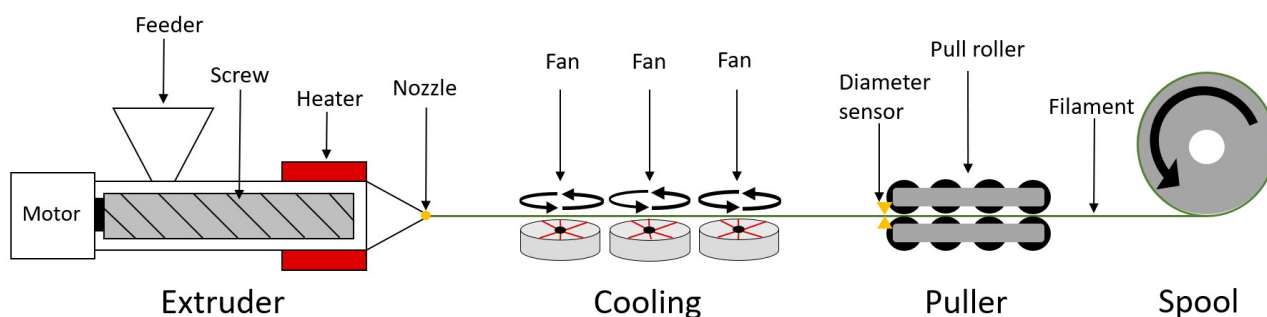


Figure 4.4: Schematic illustration of the extruder set-up to manufacture composite filaments.

4.3 3-D printing

SolidWorks 2022-2023 (Daussault Systemes SE, France) was used for CAD designing of the electrodes. The CAD files were exported as .STL file type and converted to a G-code using PrusaSlicer 2.5.0 (Prusa Research, Czech Republic) open-source program. The printed electrodes have dimensions of 25×25×1 mm³, with an average printing time per sample of 3 min using FDM and 45 min using the SLA-printer.

SLA-based printing

The SLA-printed electrodes were fabricated using a Prusa SL1S resin printer (Prusa Research, Czech Republic) with a bottom-up projection and 405 nm UV LED light source. The curing time for the pure resin was set to 25 s for the first layer and 5 s for each following layer. The thickness of each layer was set to 50 μm and the tilting profile of the printer was set to normal. For the BDR-X and UDR-X samples, the curing time was set between 50-120 s for the first layer and 10-50 s for each following layer. The light transmission depth of the photopolymer composite resin depends on the concentration of diamond particles. The increasing blocking effect of higher concentrations of diamond particles may result in a layer too thin to adhere to the previous layer, which causes print failure. The layer thickness was therefore set to 25 μm and tilting profile to highly viscous. The increased first layer exposure time and adjusted tilting profile are necessary to ensure proper adhesion of the printing samples to the print platform. After printing, all samples were cleaned for 5 minutes in isopropanol using a Form Wash (Formlabs Inc., USA) washing machine to remove uncured resin. The printing parameters for fabricating the SLA-based composites are presented in Table 4.1.

Table 4.1: Process parameters for SLA fabrication

First layer exposure (s)	Other layer exposure (s)	Layer thickness (μm)	Tilting profile
25-120	5-40	25	Highly viscous

FDM-based printing

The FDM-printed electrodes were manufactured using a low-cost Prusa i3 MK3S+ FDM printer (Prusa Research, Czech Republic). To withstand the abrasive nature of diamond, the commercial printer was modified by replacing several standard components. The hot-end was replaced by one which could operate at increased operating temperatures (from 250 °C to 300 °C). Furthermore, an enlarged, 0.8 mm, ruby nozzle was employed to avoid blockage of the nozzle by potential diamond aggregates and to withstand the diamond abrasiveness. The speed of the extruder head was set to 20 mm/s for printing moves such as infill and perimeter, and the speed was set to 40 mm/s for travel moves. The temperature of the heated bed was set to 50 °C for all samples, while the extrusion temperatures of the nozzle were set between 215-250 °C, depending on the composite composition. A summary of the printing parameters regarding the fabrication of FDM-based composites is presented in Table 4.2.

Table 4.2: Process parameters for FDM fabrication

Nozzle diameter (mm)	Print speed (mm/s)	Layer thickness (mm)	Nozzle temperature (°C)	Bed temperature (°C)	Raster angle (°)	Fill density (%)
0.8	20	0.3	215-250	50	45	100

4.4 Characterization

Scanning electron microscopy (SEM)

SEM was used to characterize the cross-sections of the 3-D printed diamond composites and to investigate the composite morphology. Samples were coated with a thin layer of gold using a JEOL JFC-1300 auto fine coater

to enhance the conductivity during the measurement. SEM images were taken using a JEOL scanning electron microscope (JEOL-JSM6010LA) which operated at an acceleration voltage of 5 and 20 kV. Additionally, SEM was used to investigate both BDD powders in terms of their particle size and shape. BDD powder was squashed on special carbon SEM stubs that were then mounted on the sample holder. Powder was also sputtered with a thin gold layer to increase image quality. Different equipment was used to obtain the best results regarding the imaging of both powders. At first, powders were deposited on a double-sticking carbon tape and directly mounted on aluminum mounts which were placed in the SEM. As image quality was poor, other alternative equipment was tested, such as carbon stubs. They are directly mounted on the aluminum mounts and by additionally sputtering the powder with gold, the best imaging results were obtained. Next to that, the powders were also deposited on a carbon slurry which was obtained by mixing a diluent with carbon paste, which was subsequently spread on a copper, one-sided, piece of tape. Both the carbon slurry and paste gave comparable results, with the carbon stubs having the preference over the slurry, taking into account preparation time and feasibility.

Raman spectroscopy

The Raman spectra of both BDD powders were collected at room temperature using a Horiba LabRAM HR micro-spectrometer equipped with an x, y, z moving stage. A Cobolt fandango 50 argon-ion laser operating at 514 nm wavelength and 50 mW was used as excitation source. BDD powder was manually squashed in a small cavity and placed directly under the laser. The Raman spectra were analyzed with Origin Pro 2023 software. During this research, observations were made, from which it appeared that a down-shift of the diamond peak depended on the laser intensity. Therefore, a set of systematic acquisitions were performed on the powder surface to investigate this phenomenon. [Figure B.1](#) shows a series of Raman spectra obtained from the same sample of Boromond BDD powder at different laser powers. The graph shows that when 1% of the laser power intensity is applied, the diamond peak is located at the expected, 1332 cm⁻¹. But for higher laser intensities, 10% and 100%, the diamond peak starts to shift down to 1323 cm⁻¹ and 1317 cm⁻¹, respectively. It can be concluded that the use of a laser with increased power leads to uncontrolled heating of the powders that is manifested as a broadening and down-shifting of the 1332 cm⁻¹ line.

Keyence Digital Microscope

Cross-sections of different extruded filaments were used to investigate the effect of number of extrusions on the porosity and filament quality. The effect of treatment procedure on the 3-D printed electrode surface was also studied. Measurements were carried out using a Keyence Digital Microscope VHX-6000. The filament cross-section images were taken using x30 objective lens and the images of the electrode surfaces were taken using x50 and x100 objective lens.

Mastersizer 3000

The particle-size distribution of both BDD powders was measured by laser light scattering using a Malvern Mastersizer 3000 instrument (Malvern Instruments Ltd, Worcestershire, UK) with a Hydro SM wet sample dispersion unit. The particle size distributions (PSDs), i.e., particle size at 10% (Dv10), 50% ((Dv50), median diameter), and 90% (Dv90) of the volume distribution were calculated using the Mastersizer 3000 software (version 5.54). The measurement was carried out in triplicates. BDD powder was dispersed in deionized water and added to the wet dispersion unit.

Electrical properties

The electrical properties of the 3-D printed composites were investigated using a digital multimeter (Votcraft CV820-1) equipped with two probes. The probes were manually positioned at fixed distances on the composite filaments and samples, and the obtained resistances were converted to volume resistivity using the following equation:

$$\rho = R \cdot (A/L) \quad (4.1)$$

where ρ is the volume resistivity, R is the resistance, A represents the surface area and L is the distance between the probes or length of conductive path. Electrical measurements were (when necessary) facilitated with the application of silver contacts to the composite electrodes to mitigate measurement error with uniform metallic connections.

Mechanical properties

Uniaxial tensile tests to identify the mechanical properties of the 3-D printed composites were performed using a Zwick & Roell tensile testing machine with a constant pulling rate of 20 mm/min. Yield and stiffness properties were evaluated from three specimens. Printed composite samples were dumbbell-shaped with dimensions according to the ASTM D-638 (type V) presented in Figure 4.5a. An image of the tensile test set-up with a sample placed in the machine is presented in Figure 4.5b.

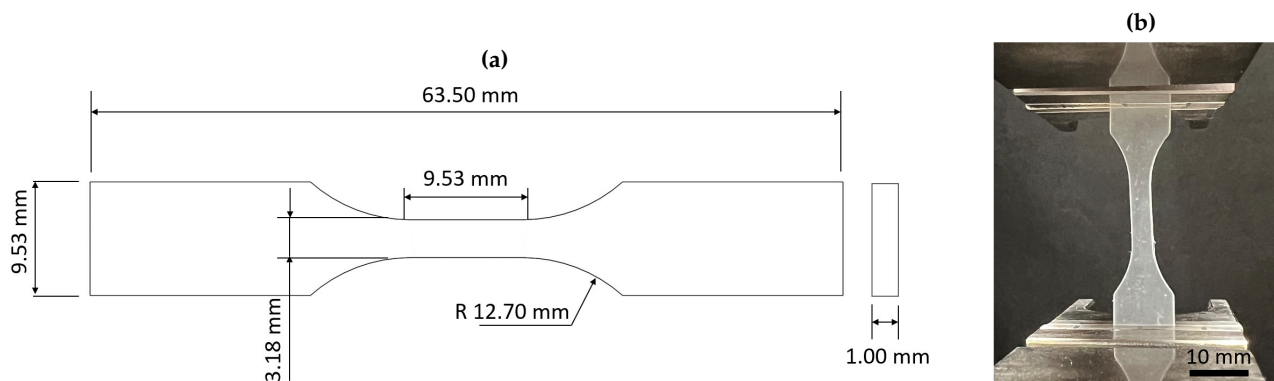


Figure 4.5: (a) Schematic drawing with dimensions of tensile test samples according to ASTM D-683 type V. (b) Image of test set-up used for tensile test.

Electrochemical properties

Electrochemical measurements, including cyclic voltammetry (CV) and differential pulse voltammetry (DPV), were carried out using an Autolab PGSTAT 128N controlled by Nova 2.1 software (Metrohm, The Netherlands). The working electrodes (WE) employed were the 3-D printed composite electrodes, as reference electrode (RE) a silver-silver chloride (RE-1BP from ALS co.) is used and a 25 cm 99.9 % platinum wire (catalog No. 50HX15 purchased from redox.me, Sweden) as counter electrode (CE) to create a conventional three-electrode set up. The WE was placed in a 25 mm x 25 mm sample holder with a 1 cm² aperture purchased from redox.me, Sweden. An image of the WE set-up with the holder is presented in Figure 4.6. The electrodes are placed inside a glass beaker, and all are submerged in the measuring solution. All experiments were performed under laboratory conditions (23 °C). During the CV, the voltage is swept from zero to a positive value to a negative value and back to zero. Each CV scan was performed five times to verify its accuracy. CV was used to determine the potential window, background current and double-layer capacitance. For the latter, CVs were recorded in 0.5 M KNO₃ in the potential range between -0.5 V and +0.5 V and the following equation (Equation 4.2) was employed to estimate the double layer capacitance (C_{dl}) values:

$$C_{dl} = \Delta I_{AV} / A_{geom} v \quad (4.2)$$

where ΔI_{AV} (in A) is the average background current difference between the forward (anodic) and reversed (cathodic) scan at a potential of 0 V, A_{geom} represents the geometric surface area (1 cm²) and v is the scan rate (0.1 V/s).

For the detection of dopamine, differential pulse voltammetry (DPV) was used. Scans were recorded using a pulse amplitude of +25 mV, pulse width of 50 ms, potential step of 2.5 mV and a scan rate of 5 mV/s.

Furthermore, a scan rate study (10, 25, 50, 75, 100, 150, 200 and 250 mV/s) is conducted using 1mM [Ru(NH₃)₆]^{3+/2+} (RuHex) and 1mM [Fe(CN)₆]^{3-/4-} (ferrocyanide), both in 0.5 M KNO₃. The data obtained

from the RuHex scan rate study is used in the Randles-Seveck equation for the determination of the effective electrode surface area (A_{eff}). The Randles-Seveck equation is presented in Equation 4.3.

$$i_p = 2.69 \cdot 10^5 n^{3/2} A_{\text{eff}} D^{1/2} C_0 v^{1/2} \quad (4.3)$$

where n is the number of exchanged electrons, D is the diffusion coefficient of the redox probe, v is the scan rate, C_0 is the concentration and i_p is the peak current.

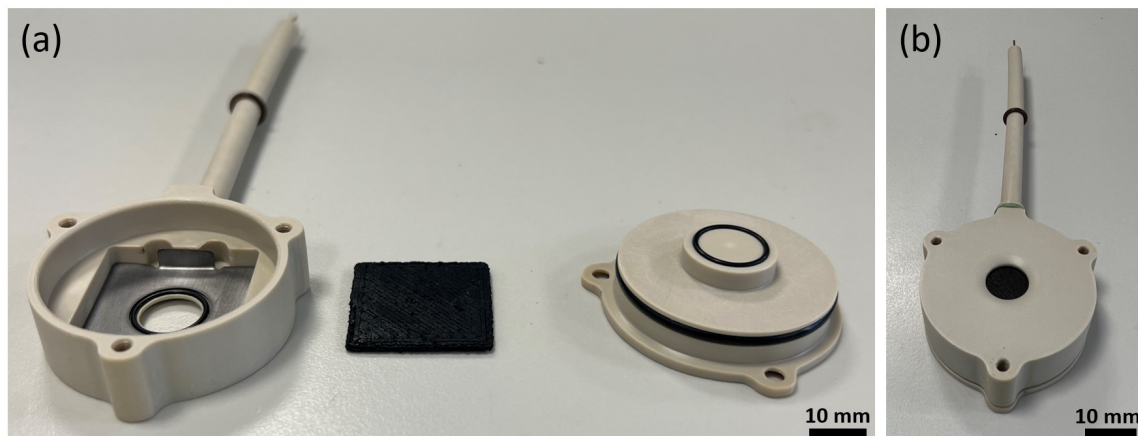


Figure 4.6: Image of (a) electrode holder parts and (b) assembled electrode holder.

5 Results and Discussion

5.1 Powder characterization

5.1.1 Powder size and shape

Particle size distributions for both BDD powders were obtained by laser diffraction analysis, and the results are presented in [Figure 5.1a](#) and [Figure 5.1b](#). Both graphs present a good picture of the distribution of the particle sizes. From [Figure 5.1a](#), it can be observed that the distribution of Boromond BDD particle size is mostly focused between $0.5\ \mu\text{m}$ and $1.5\ \mu\text{m}$. There is no symmetrical distribution of the particles visible in the graph, with a distribution maximum indicating a particle size of roughly $0.45\ \mu\text{m}$ for 8% volume of the measured sample quantity. All particles had sizes ranging from $0.1\ \mu\text{m}$ up until $3\ \mu\text{m}$. Regarding the particle size distribution of the Ultrahard BDD powder, it can be observed that the distribution is more centered around a significantly narrower range of sizes, visible in [Figure 5.1b](#). A symmetrical distribution is centered around $0.35\ \mu\text{m}$, with the maximum representing about 12.5 volume % of the measured sample. No particles larger than $1\ \mu\text{m}$ have been detected for the Ultrahard BDD powder, meaning that this type of powder can be considered sub-micron. All particles were between $0.1 - 1\ \mu\text{m}$.

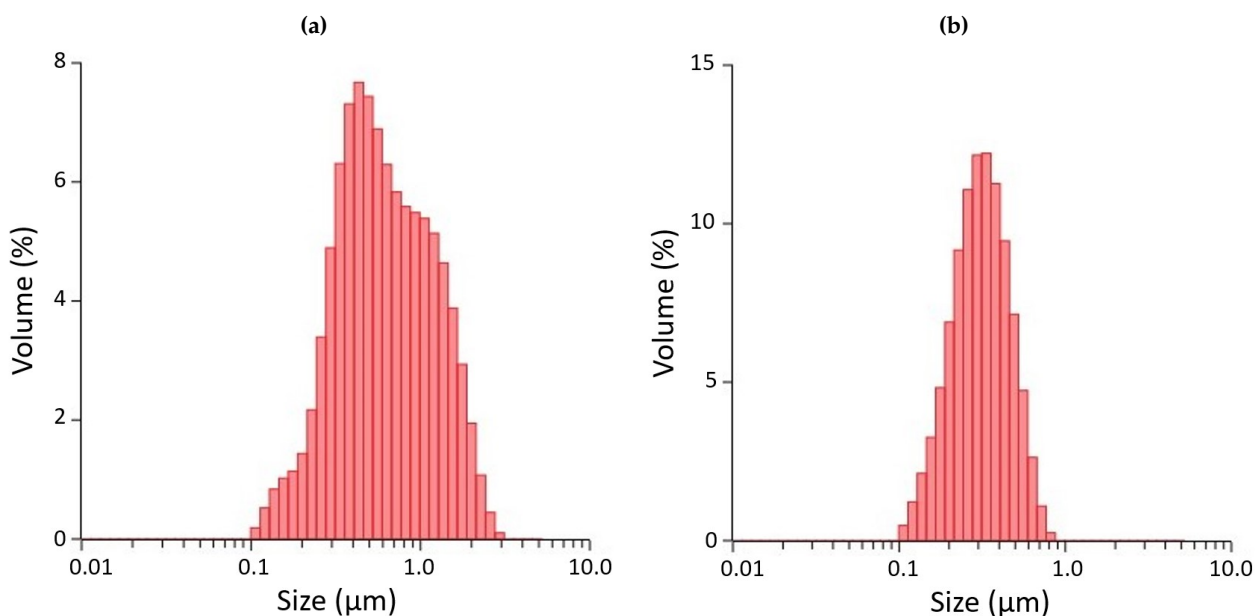


Figure 5.1: Particle distribution size of (a) Boromond BDD powder and (b) Ultrahard BDD powder.

Additionally, SEM was employed to investigate the shape and size of both BDD powders. The SEM images are presented in [Figure 5.2](#).

Regarding the particles size, if we compare the SEM images from [Figure 5.2](#) with each other, it is clear that the results obtained from the particle size analyzer are in line with the observations we can make from the SEM images. The Boromond BDD particles are clearly, on average, larger compared to the Ultrahard BDD particles. Also, the Ultrahard particles seem to be more similarly sized compared to the Boromond particles, which is also in line with previously established observations (See [Figure 5.1](#)).

Lastly, the shape of the particles is for both powders rather sharp. Especially the Boromond BDD powder has particles with sharp, and pointy edges. Most particles are non-spherical and showed a cubic-like shape.

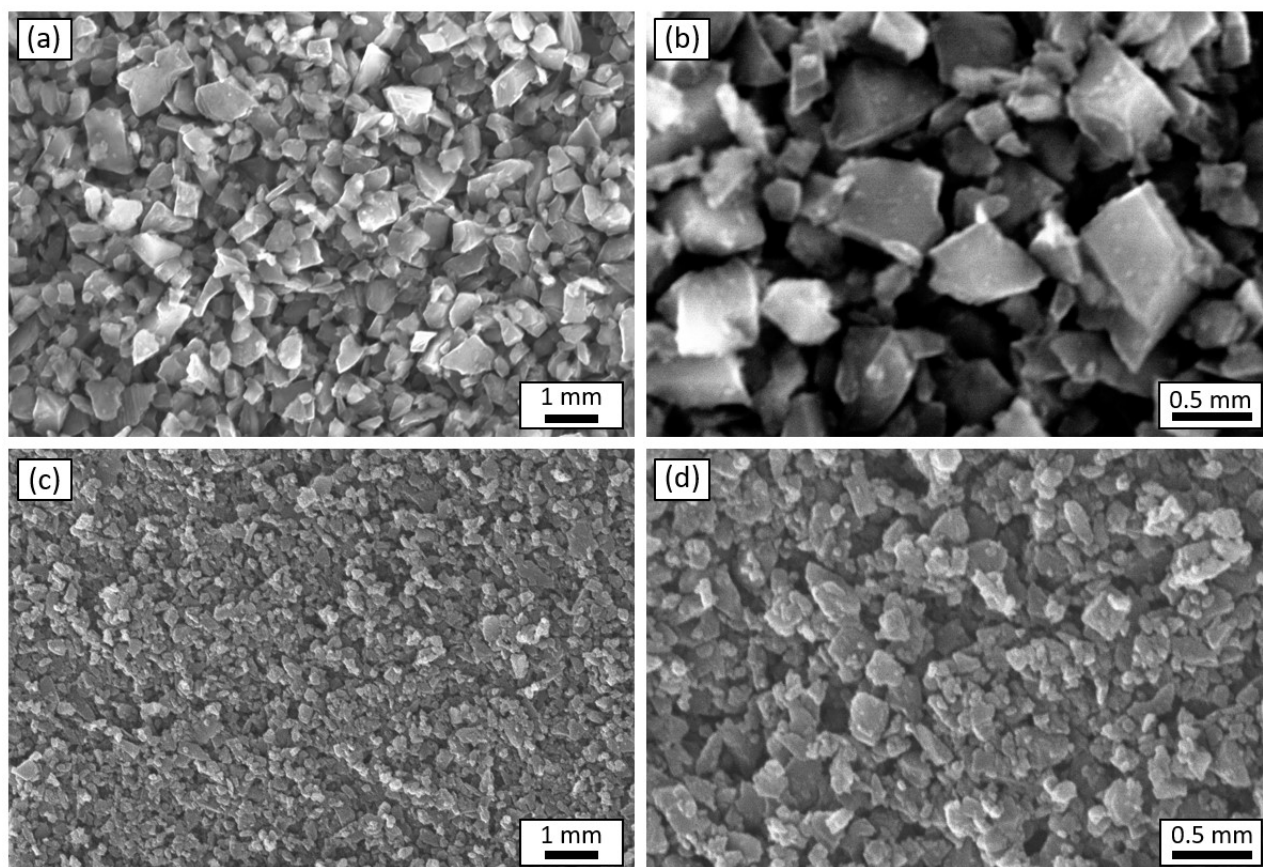


Figure 5.2: SEM images of different BDD powders with different magnifications. Magnified image of Boromond BDD powder at (a) x11000, (b) x30000, and of Ultrahard BDD powder at (c) x11000 and (d) x30000.

5.1.2 Powder composition

Raman spectroscopy was employed to assess the composition of the BDD powders and to evaluate their boron content. The Raman spectra of both powders are presented in Figure 5.3a. The common feature of the recorded Raman spectra for both samples is the sharp first-order diamond peak located at 1332 cm^{-1} . This characteristic peak is related to the presence of C–C sp^3 chemical bonds and is commonly present in bulk diamond single-crystals [122]. Moreover, another band region, between $1500 - 1600\text{ cm}^{-1}$, can be observed in the Raman spectrum of the Ultrahard BDD sample which is possibly due to sp^2 amorphous carbon (G-band). The Boromond BDD powder on the other hand shows a symmetric Raman spectrum with a clear diamond peak present at 1332 cm^{-1} which means that the composition of the powder is dominated by sp^3 carbon. In addition, the Raman spectra presented in Figure 5.3b provide more information on the composition of both powders. For the Boromond BDD powder, there is a symmetric band situated around the 1332 cm^{-1} . This behavior is very much in line with reported literature [123] related to Raman analysis of undoped diamond micropowders. Since there is a strong resemblance in terms of symmetry compared to undoped diamond powder, it would indicate a significantly low level of boron doping of the powder.

On the other hand, a more asymmetric shape of the diamond peak can be observed for the Raman spectra of the Ultrahard BDD powder. This could indicate the presence of boron in the diamond crystal, which has been reported in literature. It is known that an increase in boron concentration within the diamond lattice leads to an increasing asymmetry in the first order Raman peak (zero phonon line) [122]. This effect was further investigated by Ushizawa and colleagues [124]. The asymmetric behavior is generally starting to

develop when concentrations of 200 ppm of boron or higher are present in the diamond crystal. The observed asymmetry is not very prominent, and therefore it is hard to make any conclusive decision on the boron doping level in the powder. Moreover, there appears to be a broad, but very weak, Raman band situated around 500 cm^{-1} , which is often linked to boron doping in diamonds [125]. It can be concluded due to the visible asymmetry that there is a certain concentration of boron present, but the doping level will be relatively low, in the region of 200 to maximum 750 ppm compared to reported literature. Lastly, it is reported that the reduction in particle size, and therefore, the increase in surface-to-volume ratio compared to bulk diamond powder, can cause a downshifted diamond peak towards lower wavenumbers [126]. Thermal effects, such as size of particles and laser power, must be considered when interpreting any downshift of the 1332 cm^{-1} diamond Raman line.

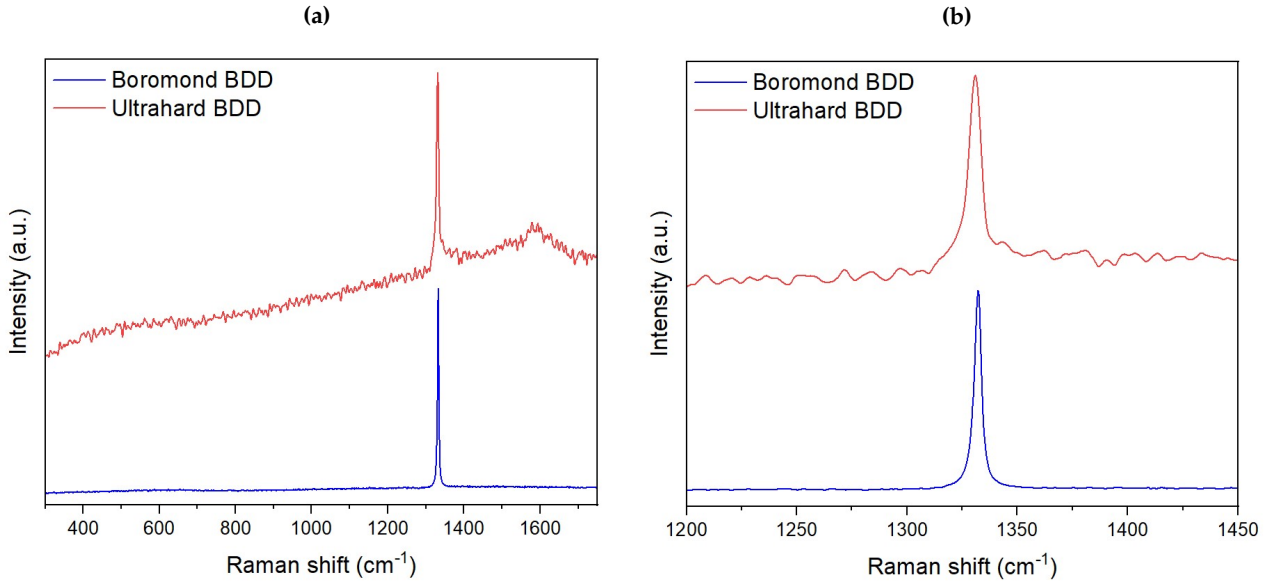


Figure 5.3: (a) Raman spectra of Boromond BDD powder (blue) and Ultrahard BDD powder (red). (b) Raman peak of Boromond BDD powder (blue) and Ultrahard BDD powder (red).

All previously reported Raman spectra were acquired at a reduced laser power intensity. To achieve this, a neutral density (ND) filter was applied, which allowed only 1% of the laser power to be subjected to the sample surface. During earlier acquisitions, when higher laser powers were used, dark spots were noticed after a measurement cycle on the sample surface. Using the ND filter, the laser power could be controlled, and these spots generally decreased in size and darkness, and eventually disappeared as the laser power was decreased. The presence of dark spots on diamond (micro)powder samples has earlier been reported by researchers [126]. They are directly related to the laser power, which causes local heating on the sample surface.

5.2 SLA-based Composites: Fabrication and Characterization

5.2.1 Fabrication

Prior to the fabrication of the SLA-printed electrodes, various experiments were conducted to investigate the effects of introducing BDD particles in a photoreactive resin (reported in Table A.1). When BDD particles are introduced in photoreactive resins, the composition of the resin starts to change, subsequently affecting its viscosity, density, but also the way in which the (composite) resin cures. Low viscosity or good fluidity is crucial in the process of 3-D printing through polymerization, but retaining this property can be challenging when working with composite resins. This is because the viscosity of photosensitive resin tends to increase with increased filler content [127].

The following sections are dedicated to present and discuss the effect of increased filler weight percentage on the mechanical, electrical and electrochemical properties. Also, the effect on the morphology of the electrodes will be discussed.

5.2.2 Morphological and surface characterization

After printing the BDD/photopolymer composites, the samples were investigated by SEM. SEM images of a fracture surface presented in Figure 5.4 show noticeable differences between the pristine flex80 resin (a) and the BDD composite samples (b) and (c). The pristine resin sample has a smooth surface compared to both BDD composite surfaces. A few white spots are noticed in the image, but could be attributed to contamination. For images (b) and (c) presented in Figure 5.4, the surface is mostly characterized by a more rigid-like, bumpy surface morphology. The rough surface contains multiple pullouts (white fragments) and has significantly more voids and grooves compared to the pristine resin. This can also be observed on the fracture surface's coarse area, corresponding to the locations where the BDDs were completely pulled out and indicating in some areas a weak interface between the BDDs and the polymer matrix. Increased surface roughness with composite resin samples compared to neat resin is expected and has earlier been reported in literature [91, 128]. The BDD particles are well distributed throughout the polymer matrix in both samples (Figure 5.4b,c) and no clear sign of agglomeration is observed.

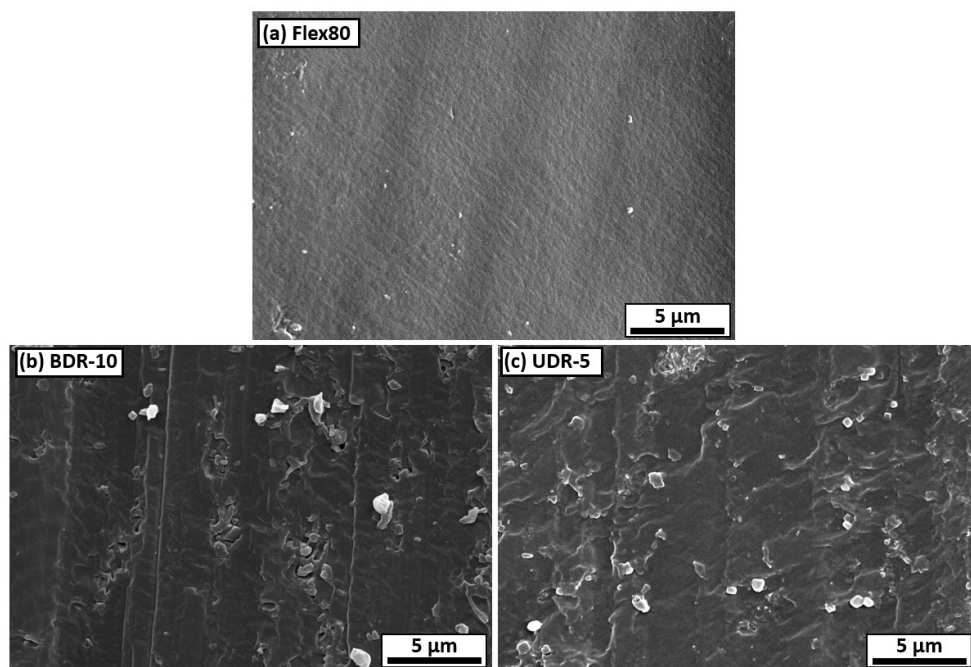


Figure 5.4: SEM images of the fracture surface of different 3-D printed samples: (a) neat resin, (b) BDR-10, and (c) UDR-5.

Furthermore, different graphic features of the composites were detected with the increasing concentration of BDD additives. For all samples, presented in Figure 5.5, the fracture morphology is mostly characterized by multiple particle pullouts (white fragments). Several of these pullouts exist in the structure, which means they are not tightly stacked in the resin matrix, resulting in weak adhesion between additives and matrix. With increasing wt.% of additives, the white fragment pull-outs start to appear more frequently. Similarly, the increase in weight percent of additives leads to the occurrence of more particle aggregation, visible in Figure 5.5b. More “clustered” fragments are present at 12.5 wt.% compared to 10 wt.%, mainly visible on the right side of the image depicted as white spots. Also, the agglomerates tend to increase in size when the weight percentage is increased, which is in line with previous findings by Zhang and colleagues [128]. In addition, Figure 5.5c,d present the morphology of the UDR printed samples. Here, the presence of fillers seems to be less predominantly existing. Possibly, due to the lower weight percentage of powders used, but the effect can also be explained by the smaller particle size which means they are more difficult to observe.

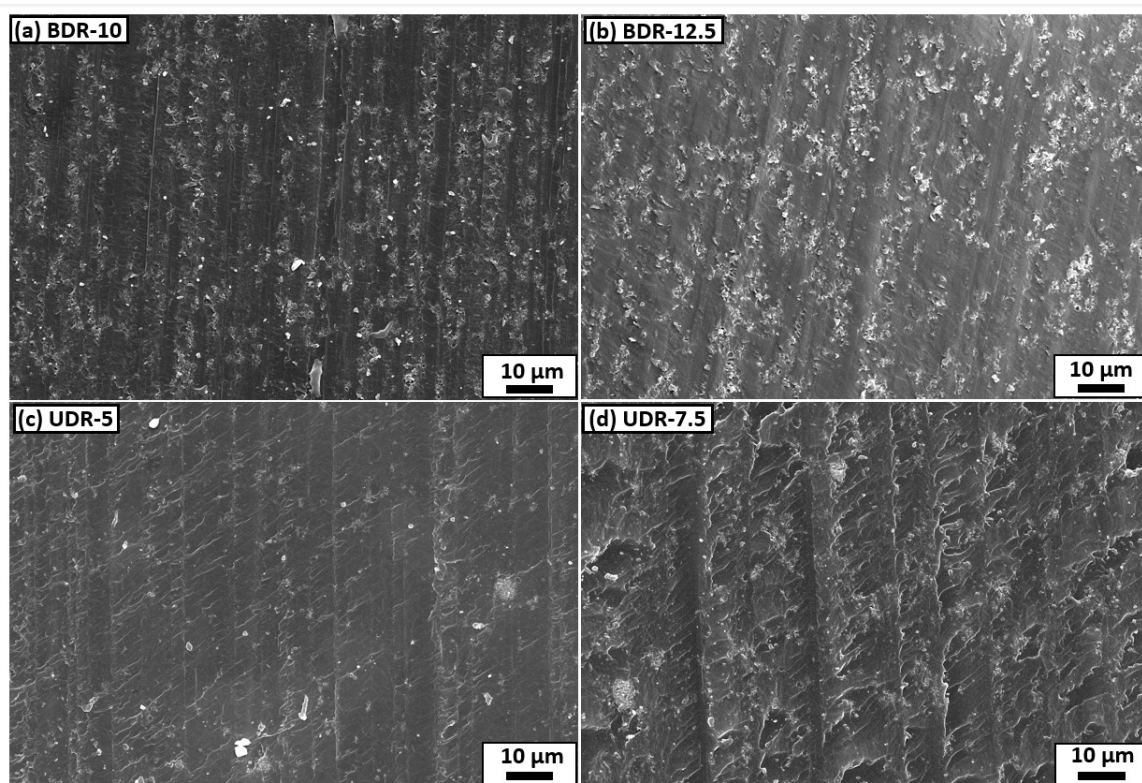


Figure 5.5: SEM images of the fracture surface of different 3-D printed samples: (a) BDR-10, (b) BDR-12.5, (c) UDR-5, and (d) UDR-7.5.

5.2.3 Mechanical, electrical and electrochemical characterization

The addition of BDD reinforcements to the SLA resin will have significant impact on various properties of the composite samples. This section will present, discuss and evaluate the effect of the BDD particles on the mechanical, electrical and the electrochemical properties of the flexible photoreactive polymer.

Mechanical characterization

The values of Young's modulus, tensile strength and elongation at break of the materials studied are reported in Figure 5.6 and Table 5.1. Figure 5.6 represents the stress-strain curves of all tested composites. The figure reveals that all 3-D printed composites show a similar stress-strain curve. However, one can distinguish each sample by a change in the slope and stress. Neat Flex80 resin exhibited a Young's modulus of 2.40 MPa, a tensile strength of 2.25 MPa, and an elongation at break of 93.6 %. The data in Table 5.1 evidence that the tensile strength of the composites was in the same range and mostly exceeded that of the Flex80 resin. It should therefore be recognized that the addition of the BDD particles alters the microstructure of the material and allows it to maximize the interaction with the polymer matrix, resulting in a better resistance against high stresses, if properly implemented. Moreover, the increase in tensile strength, which is present for all composites, was also accompanied by a surprising increase in elongation compared to the Flex80 resin. This would indicate that the addition of micro-diamond particles increases the strength of the composite without compromising the elongation. Toughening of the polymer by addition of BDD fillers, allowing it to absorb more energy, is therefore well recognized. Nevertheless, it is unexpected that the sample with the lowest elongation is the one without reinforcements, Flex80. This can possibly be attributed to the absence of post-treatment to the photoreactive composite samples. Due to the presence of amounts of unreactive groups which are left inside the manufactured sample, the stability, and strength of the 3-D printed product are affected. Post-curing processes integrating UV and heat guaranty the conversion of the unreacted groups and enhance the mechanical properties of the 3-D printed parts [113, 129]. For this reason, the same experiment had also been conducted with mild annealing (70°C) and curing for 1 hour of the measured samples. The results

from this experiment concluded that the effect of post-treatment (mild annealing with curing) significantly influences the mechanical properties of all composites, with the Flex80 resin being most heavily affected. The results can be found in Table B.1. In brief, an opposite trend (i.e., deteriorated mechanical properties as function of filler content) was observed for the post-treated samples.

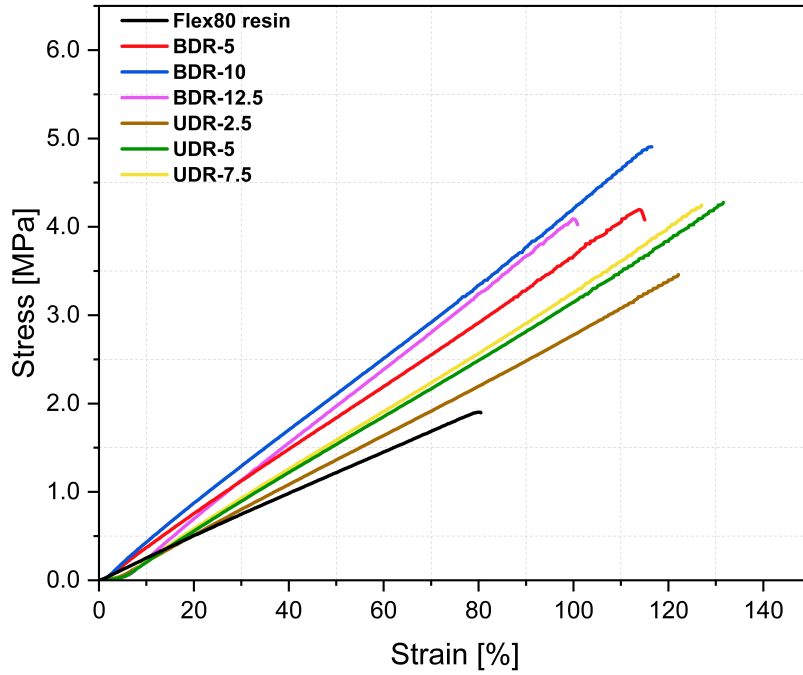


Figure 5.6: Stress-strain curves of SLA-printed composite samples.

The Young's modulus of all composites (without post-treatment) was improved in comparison to the Flex80 resin, and it also enlarged with increasing filler content (visibly presented in Figure 5.7). The largest increase in Young's modulus, by up to 175 %, was found for the BDR-12.5 composite, also having the highest wt.% of BDD fillers. This result was expected, as the higher the weight percent, the more rigid links are between the polymer and diamond in the composite matrix, making it stronger, but at the same time decreasing its ductility. Another interesting observation can be made when comparing the different weight percentages for each of the two BDD samples. For both BDD composites (BDR and UDR), the increase in Young's modulus tends to decrease when it is approaching the highest reported weight percentage. This effect can plausibly be attributed to the formation of aggregated or clustered particles. As previously observed from the SEM images presented in Figure 5.5, the BDR-12.5 images show more clustered areas where there is a concentrated presence of BDDs compared to the lower weight percent sample. An increase in aggregated particles creates local stress concentration points which deteriorate the mechanical properties of the material [130]. Moreover, this can be explained by the effect of filler-filler or filler-polymer interactions. At lower filler concentrations, or in situations where the inter-filler interaction is not favorable over the filler-polymer interaction, mechanical stiffening of the material occurs (when there is a homogeneous dispersion), visible by comparing Flex80, BDR-5 and BDR-10. While at a higher filler concentration (BDR-12.5), filler particles are more prone to interact with each other as compared to with the polymer molecules, leading to localization of interacting fillers. This could also explain the decrease in tensile strength of BDR-12.5 compared to BDR-10 (4.75 MPa vs 4.08 MPa).

Other researchers similarly reported an enhanced Young's modulus with increasing filler content using micro- and nanodiamond particles [119, 131–133]. This observed effect can be explained by the way the fillers interact with the photoreactive polymer. For all reported findings, the addition of diamond reinforcements increased the Young's modulus from 50 % up to 400 %, depending on the particle size and weight percentage. Zubrowska et al. [131] more specifically investigated the effect of micro- and nanodiamond size and their weight percentages on the mechanical properties of a polymer. Although their findings concluded that the Young's modulus increased when the weight percentage of diamond also increased, they reported no significant effect of the change of particle size on the mechanical properties. Similar conclusions can be drawn when

comparing the mechanical properties of the BDR-5 and UDR-5 samples. The presented Young's modulus, tensile strength, and elongation at break have close resemblance and show only minor deviations. Still, it should be noted that the size of the BDR and UDR particles did not significantly differ from each other in order to make substantial conclusions about the effect of size on the mechanical properties.

Even though reports on carbon-based additives to improve mechanical properties of photoreactive resins are rather limited, some researches have successfully reported great results. Lin et al. [114] fabricated a composite resin containing 0.2 wt.% of GO (graphene oxide) without post-treatment of the samples. It was found that compared with pure polymer resin, the tensile strength increased 62.2 % and the elongation was increased by 12.8 %. Xiao et al. [115] used a combination of carbon fiber and graphene oxide to reinforce a photoreactive polymer resin. The tensile test showed that when the weight percent of fillers was increased, the material behaved more stiff, lowering its ductility, and is comparable to the results of this study. These two studies show that even with relatively low additive loadings (0.2 wt.% and 0.8 wt.% respectively), the additives already provide a substantial increase in mechanical properties such as tensile strength and stiffness. So far, extensive literature data on low additive loadings of diamond micro/nano powders, and how they affect the mechanical properties of SLA-printed composites, is missing.

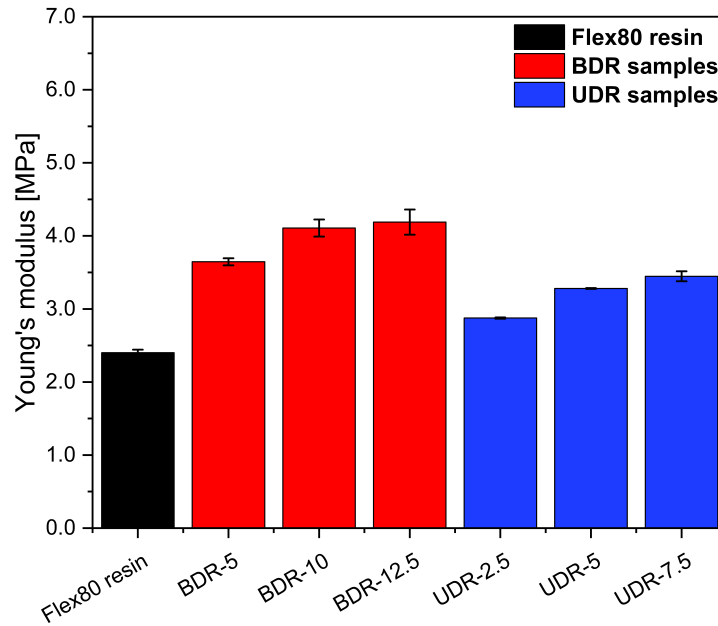


Figure 5.7: Young's modulus of all SLA-printed composite samples.

Table 5.1: Material properties calculated from tensile and electrical tests of all SLA-printed composite samples.

Samples	Young's modulus (MPa)	Tensile strength (MPa)	Elongation (%)	Conductivity (S/cm)
Flex80	2.40 ± 0.04	2.25 ± 0.45	93.6 ± 17	Not measurable
BDR-5	3.65 ± 0.05	4.37 ± 0.18	120 ± 5.1	Not measurable
BDR-10	4.11 ± 0.12	4.75 ± 0.17	115 ± 2.4	Not measurable
BDR-12.5	4.19 ± 0.17	4.08 ± 0.15	97.2 ± 3.1	Not measurable
UDR-2.5	2.88 ± 0.01	3.47 ± 0.07	123 ± 1.5	Not measurable
UDR-5	3.28 ± 0.01	4.30 ± 0.19	129 ± 3.9	Not measurable
UDR-7.5	3.45 ± 0.07	4.33 ± 0.2	123 ± 3.6	Not measurable

Electrical and electrochemical properties

Presented in [Table 5.1](#) and [Table B.1](#), the electrical conductivity of all SLA-printed samples was not measurable with the applied equipment. Even though silver ink was applied to increase the contact conductivity between the measuring probes and the sample surface, and samples were immersed in acetone, the resistance was still above the maximum detectable threshold of 200 M Ω . One possible reason for this insulating behavior is that the weight percentage of the used particles is too low to facilitate a conductive network through the material. It means that the particles inside the polymer matrix are too far apart from each other, which would restrict the transfer of electrons to take place. However, another viable reason for the high resistivity of the SLA-printed samples could simply be the lack of electrical conductivity of the boron-doped diamond particles themselves. Taking into account the earlier presented Raman spectra ([Figure 5.3a](#)) which concluded that the boron doping level is relatively low, and far from conductive, it is more likely that the insulating behavior can be attributed to the very low level of doping. In addition to that, the earlier presented SEM images showed good dispersion of the BDD particles and only a few aggregations were observed.

Nevertheless, electrochemical measurements were carried out in order to validate the previously made observations, considering the electrical conductivity of the samples. The SLA-printed samples with the highest weight percentage of BDD fillers were chosen to be tested to investigate their electrochemical response. Unfortunately, but not unexpected, both samples (BDR-12.5 and UDR-7.5) showed no response to a standard electrochemical characterization in 0.5 M KNO₃ solution. The results can be found in [Figure B.3](#).

5.3 FDM-based Composites: Fabrication and Characterization

5.3.1 Fabrication

Composite formulation

A schematic illustration of the composite formulation process, including photos of the respective materials and solutions in the various steps, is presented in [Figure 5.8](#). The manufacturing process involved different complex steps which made it challenging and thus required close monitoring, and constant reiteration of the various steps. Some examples are proper dissolution of the polymer, ensuring homogeneous dispersion of added particles and proper removal of solvent. Optimization of the different process parameters such as choice of solvent, stirring temperature, stirring time and stirring speed proved important, but also other parameters such as, size of magnetic stirrer, size of beaker and powder preparation procedure were found to be critical. The presented process parameters in [Figure 5.8](#) have been carefully chosen for these specific manufacturing conditions and were partially inspired by previously reported procedures in the literature. An overview of these is presented in [Table B.2](#).

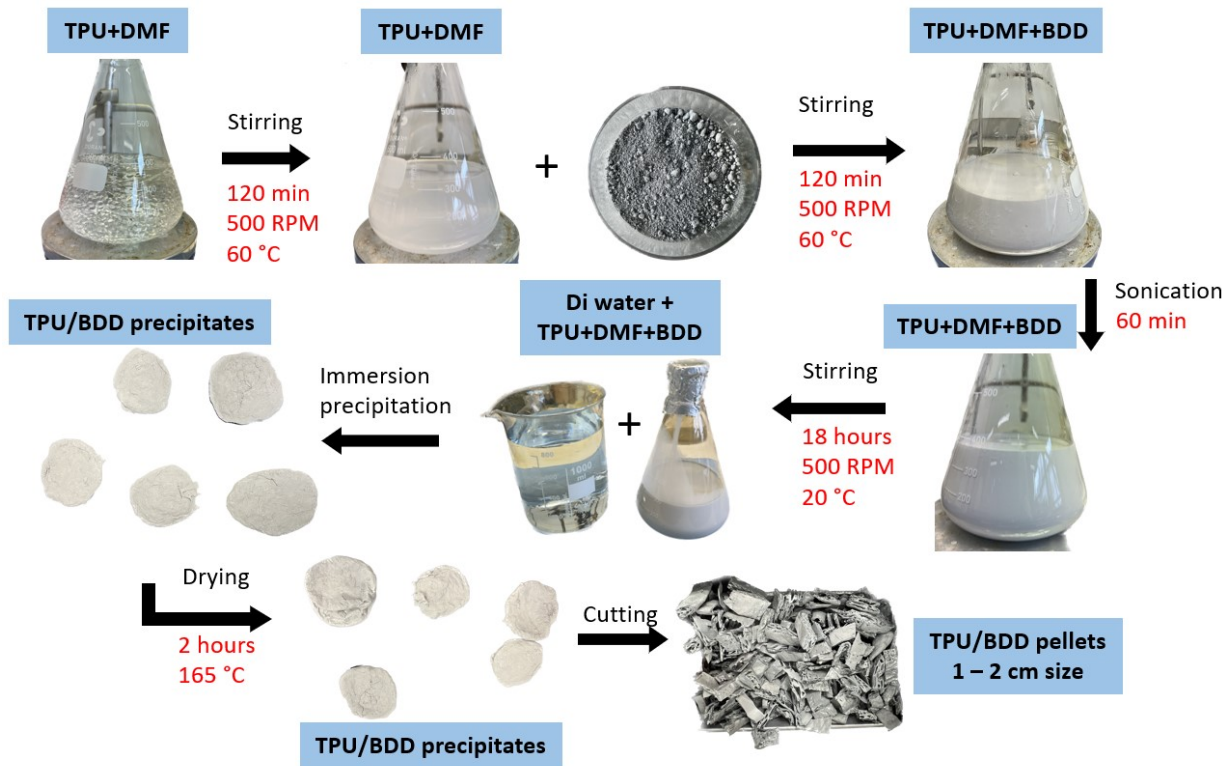


Figure 5.8: Schematic illustration of the FDM-based composite formulation process.

Extruding and 3-D printing

After successfully formulating the different composites, each composition had to be individually formed as a printable filament material. An overview of all extruded filaments used in this study is provided in Figure 5.9. For this process, the manufactured pellets were fed to the hopper element of the extruder, and extruded via a 1.75 mm nozzle. Similar to the composite formulation process, the process of extruding a composite filament, in order to achieve a homogeneous, dense and straight material, required to be meticulously approached.

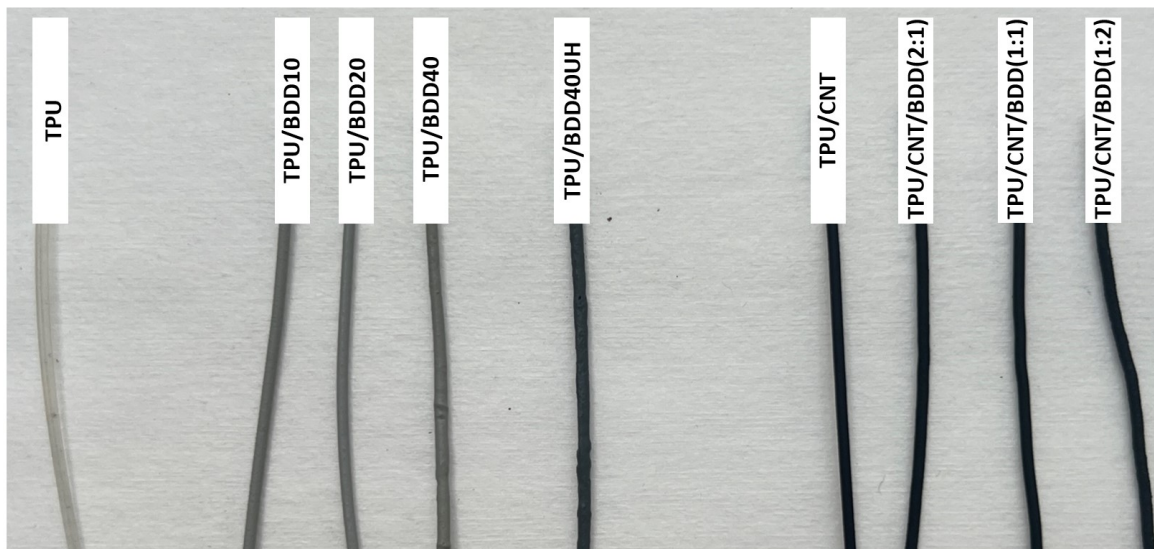


Figure 5.9: Overview image of all manufactured FDM-based filament composites.

Parameters such as extrusion temperature, screw RPM and spool speed were each carefully optimized and their effect on the filament quality was closely monitored. The filament quality, which is mostly determined by the uniformity of the filaments' diameter, is the most critical factor in the process of 3-D printing, as it determines the success rate of the 3-D printed object. For each sample composition, roughly 35 grams of pellets were manufactured, which provided sufficient material to optimize the extrusion conditions and fabricate a sophisticated filament.

In general, the diameter of a filament is determined by a combination of the extrusion temperature, screw speed and spool speed. For neat TPU, without the addition of particles, the extrusion settings had been established by the manufacturer of the used machine. Moreover, the effect of extrusion temperature and screw speed on the filament diameter has been studied in literature as well. Liu et al. [134] found a correlation between these two parameters and the filament thickness. Their data showed that when the extrusion temperature was kept constant, the filaments' diameter grows as the screw speed increases. This is because the melt volume extruded out of the die increases as the screw speed increases, causing a pronounced swelling of melt and a larger diameter in the subsequent cooling process. They also found a reduction in filament thickness when the temperature was increased, while keeping the screw speed constant.

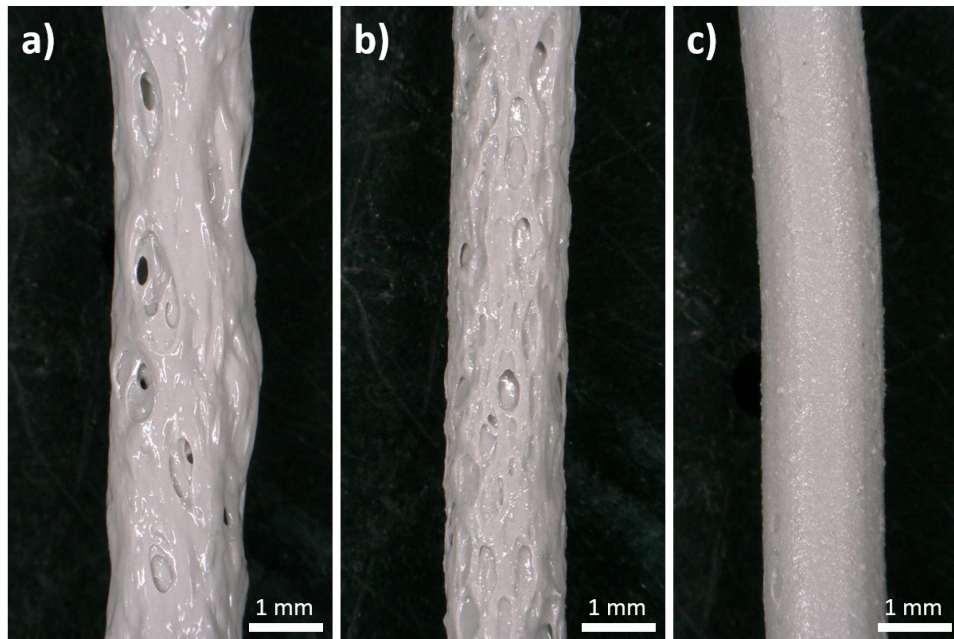


Figure 5.10: Effect of the number of extrusions on the filament surface roughness: (a) 1, (b) 3, (c) 5 extrusion steps.

Filaments extruded only once were significantly ruptured and porous (Figure 5.10a), with an inconsistent diameter, reflecting a nonuniform distribution of BDD particles within the pellets. Voided structures were still evident in the filaments extruded for the third time (Figure 5.10b), although these reduced in size and number drastically, following the fourth extrusion. After the final fifth extrusion, the filament was dense with an evenly distributed diamond loading, and consistent filament diameter (Figure 5.10c). Furthermore, the cross-sections of the filament were each investigated by optical microscopy to visualize the degree of porosity inside the material. Optical images showing the effect of number of extrusions on the filament cross-section are presented in Figure 5.11. Equivalent observations were made by Kalsoom and colleagues [119] who similarly investigated the effect of number of extrusions on the porosity of the filament. They reported a minimum number of six extrusions that were required to obtain a dense, non-porous filament. Their observations were similar to the ones presented in this study, and they also mentioned the presence of voids and a non-homogeneous diameter, which slowly improved as the filament was re-extruded. One should however consider the effect of material degradation as a result of the amount of extrusion times due to the numerous exposure to the high temperatures. A study that deeply investigated the effects of the re-extruding filament was conducted by Cieslik and colleagues [135]. They investigated the effects of extrusion temperature (190 °C-200 °C) and reprocessing steps on the rheology, morphology, thermal and electrochemical properties

of a conductive PLA 3-D printing filament. Based on their research, several findings were reported. Multiple cycles of reprocessing resulted in degradation of the polymer matrix. As the number of reprocessing cycles was increased, the more reduced the electrical conductivity was, but also the electrochemical properties were deteriorating as the cycles increased. Both events were reportedly attributed to the formation of conductive aggregates during the re-extruding process. From this research, one should therefore carefully consider the effects of the re-extrusion on the material properties and limit the number of extrusions as much as possible.

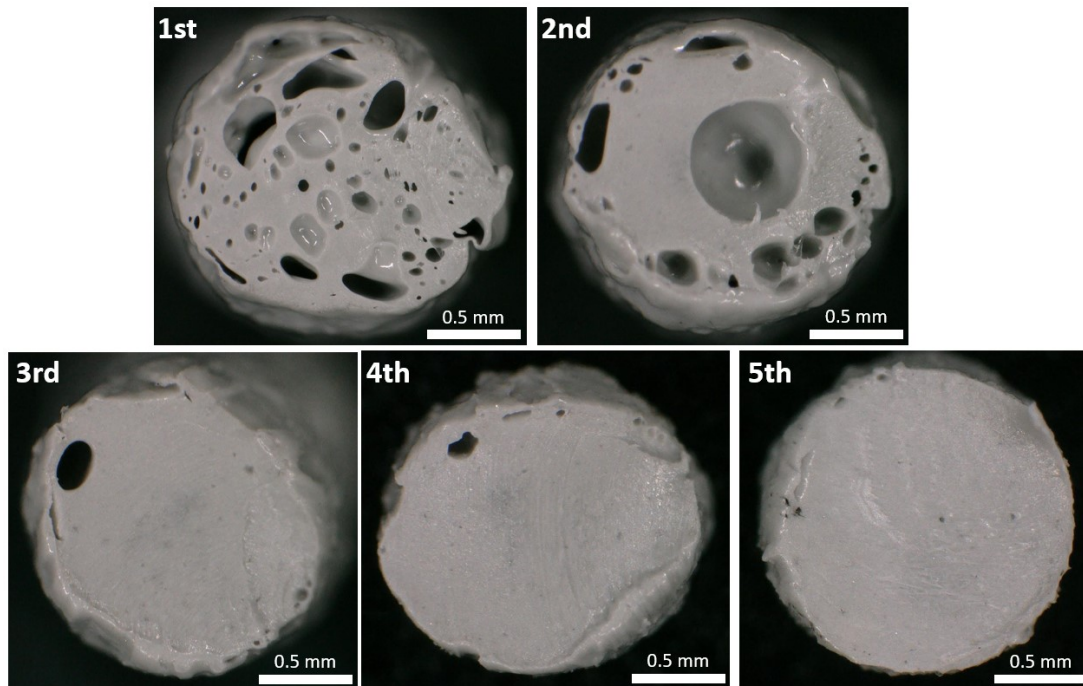


Figure 5.11: Effect of the number of extrusions on the filament cross-section.

After successfully extruding the composite filaments necessary for this study, the filaments were used in the 3-D printer to print several, standard electrode designs.

5.3.2 Mechanical characterization

Figure 5.12 demonstrates the stress-strain curves of various composite samples tested (presented in Figure 5.13). TPU with no BDD fillers exhibited 22 MPa of tensile strength and an elongation at break of 1458 %, which can be seen in Figure 5.12a. It is confirmed that the addition of BDD particles causes a decrease in tensile strain, and lowers the maximum tensile strength of the material. With 10 wt.% added BDD particles, the tensile strength was already decreased by 30% and the elongation by almost 50%. When the BDD concentration was increased to 40 wt.%, there was a detrimental effect on all mechanical properties. A definite decrease of 86% of the original tensile strength was observed, while the elongation was reduced with an astounding 99% compared to the neat TPU. These results present conclusive evidence that there is a significant effect of the addition of BDD particles on the tensile strength and elongation of the composite. A clear trend can be observed once we compare the tensile strength, and elongation values with the different weight percentages of BDD. The higher the weight percent, the lower the elongation of the material, and the lower the tensile strength of the composite material becomes. The effect of the lowered elongation can be easily explained. As reinforcements are added, the material will become stronger, and it will reduce the plastic flow of material during the loading and causes the elongation to drop. As the strength of the material goes up, there will be a corresponding drop in elongation. This effect is consistent with reported literature findings that used similar thermoplastics with carbon-based additives. [90, 91, 103, 109, 119].

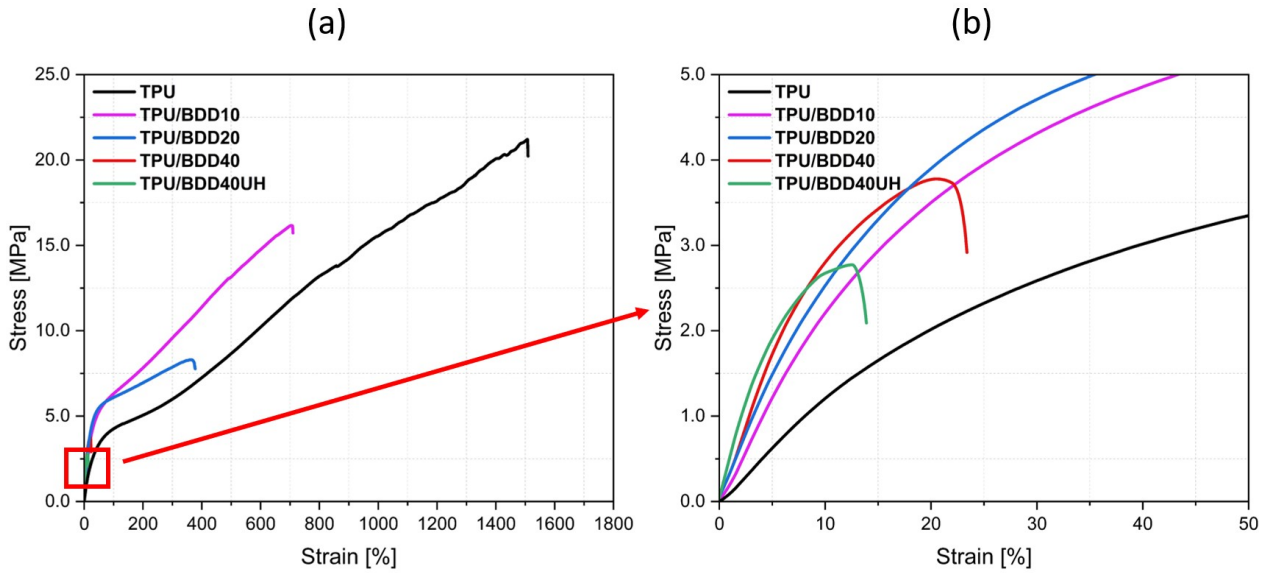


Figure 5.12: Stress-strain graph of the various FDM-printed composite samples; (b) shows a magnified view of the lower strain range, indicated by the red box and arrow in (a).

The reduction in tensile strength with increasing BDD content is inconsistent with the composite theory, that suggests strength improvement under the condition of homogeneous dispersion. The effect could be explained by different things. First, poor dispersion of the BDD particles in the TPU matrix, which creates BDD clusters in the polymer. In this case, the clustered BDD sites will introduce local stress concentrations making it more susceptible to failure, and therefore will reduce tensile strength. Second, it could be that the interface between the BDD particles and the polymer matrix is too weak, meaning insufficient binding between the particles and the polymer [136, 137]. It will result in failure of directed load transfer and restrict stresses to be efficiently transferred to the fillers during deformation due to poor interface between the polymer and particles. This will create local stress concentrations which are critical for the tensile strength. Third, the ratio of BDD to polymer is simply too high which will subsequently introduce poor dispersed particles, resulting in aggregation.

Different publications reported comparable findings regarding a decrease in tensile strength for increasing filler content. Tzounis and colleagues [91] fabricated a flexible, conductive TPU/CNT composite with up to 5 wt.% of fillers. They reported that the tensile strength of each composite decreased after every increase in weight percent. The reasoning for this behavior was reported to be a possible result of the weak interfacial strength of the interlayer bonds, which create stress concentration sites. Studies by Kim [103] and Christ et al. [90] found comparable mechanical behavior and similarly attributed this to the possible effect of a decreased interfacial strength between the polymer and additives. It should also be mentioned that equal behavior was observed for other thermoplastic polymers [108–110]. In a work focused on understanding the relationship between filler size and properties of PLA/GNP nanocomposites, the tensile strength was increased for the composites containing up to 7 wt.% of filler, but beyond this value, the tensile strength was decreased due to the presence of aggregates [111].

From Figure 5.12, the effect of BDD fillers on the stiffness of the composites was also observed. The slope of each curve in the elastic deformation region was differentiated, and TPU/BDD/40UH has the highest fragility, followed by TPU/BDD/40, TPU/BDD/20 and TPU/BDD/10. In general, the stiffness of all FDM-printed composites increased with the addition of BDD compared to neat TPU, being in good agreement with different results presented in the literature [90, 91, 119]. The increase in stiffness can be explained as follows: when inorganic fillers such as BDD are loaded into thermoplastic polymers such as TPU, they are capable of playing the role of a skeleton in the matrix. Therefore, the movement of the macromolecular chains is limited due to several physical cross-linking points between them and the polymer chains, thus improving the composite's stiffness.

An overview of all mechanical properties calculated from the tensile tests is presented in Table 5.2.

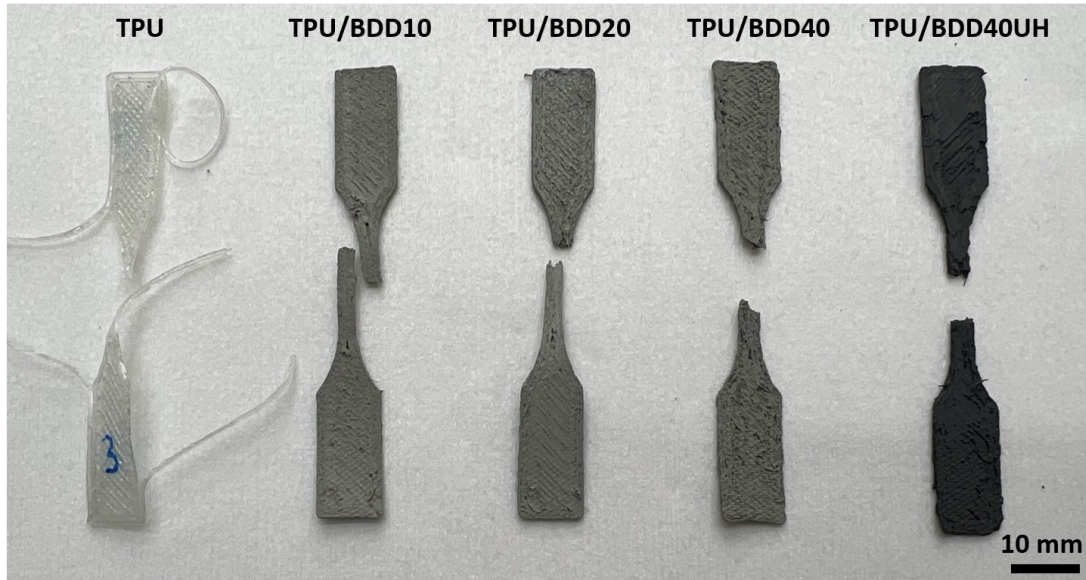


Figure 5.13: Image of composite samples used for tensile test.

Table 5.2: Material properties calculated from the tensile and electrical tests of the studied FDM-printed composites.

Samples	Young's modulus (MPa)	Tensile strength (MPa)	Elongation (%)	Conductivity (S/cm)
TPU	13.3 ± 0.5	21.8 ± 6.55	1458 ± 389	Not measurable
TPU/BDD10	24.3 ± 1.2	15.7 ± 0.41	716 ± 25.9	Not measurable
TPU/BDD20	29.9 ± 0.7	8.51 ± 0.38	359 ± 7.1	Not measurable
TPU/BDD40	35.4 ± 2.9	3.28 ± 0.75	17.8 ± 2.3	Not measurable
TPU/BDD40UH	43.9 ± 7.1	2.99 ± 0.29	12.4 ± 0.9	Not measurable

5.3.3 Electrical characterization

TPU/BDD composites

The 3-D printed composites, previously used for mechanical characterization, were also used for electrical characterization. The results of the characterization are presented in Table 5.2. Unfortunately, their resistance (above 200 M Ω) was not measurable with the equipment employed for this investigation, and were therefore considered poor electrode material, not suitable for its application. There was no electrically conductive network present in order to promote electron transfer, even with the use of silver ink to increase surface conductivity between the probes and the material surface.

TPU/CNT/BDD composites

Due to the results obtained from the previous section, changes had to be made in the composite composition in order to achieve the objective of this study, which focused on flexible and electrically conductive 3-D printable BDD-based electrodes. Materials that have widely been implemented in 3-D printed electrode composites, show excellent electrical properties, and are recognized as diamond's allotrope, are CNTs. More specifically, multiwalled carbon nanotubes (MWCNTs) had been chosen in this study, as they retain excellent electrical properties and have proven to be an attractive material for 3-D printed electrode composites [83, 88, 89, 93]. For the remaining part of this study, different composite compositions were produced using the same manufacturing procedure as depicted in Figure 5.8. In this case, MWCNTs were first added to the TPU-DMF, stirred and sonicated, and then the BDD particles were added, stirred and sonicated. Through this way,

four different compositions were formulated which were used for the remaining part of this study. They are presented in Table 5.3.

Table 5.3: Summary of different manufactured composites containing MWCNTs.

Sample name	Weight ratio MWCNT:BDD	Wt.% of total composite TPU/MWCNT/BDD
TPU/CNT	1:0	90/10/0
TPU/CNT/BDD (2:1)	2:1	85.7/9.5/4.8
TPU/CNT/BDD (1:1)	1:1	81.8/9.1/9.1
TPU/CNT/BDD (1:2)	1:2	75/8.3/16.7

Each of the four newly formulated composites were subjected to an electrical characterization. Initially, different samples were taken from each filament composition and their resistance was measured. After that, the resistance of the 3-D printed composites was also investigated. The results for the composite filaments are presented in Table 5.4a, and for the 3-D printed electrodes, the resistance was measured in-plane and is presented in Table 5.4b. For the composite filament containing only TPU, its calculated volume resistivity was above the detectable threshold, which confirms the insulating property of the polymer. When the CNTs were introduced in the composite, there was an immediate drop in the resistivity observed. Clearly, the CNT concentration is well above the percolation threshold, and is also well above the thresholds (0.5 - 3.2 wt.%) reported in the literature that used CNTs with similar aspect ratio and properties [92, 138, 139]. The percolation threshold is defined as the minimal percentage of conductive filler required to be added to transform an insulating polymer into a semi-conductive one. It is one of the main parameters that scientists need to consider when formulating conducting composites for electrode materials. It is worth mentioning that the electrical percolation threshold is much lower than the mechanical percolation. The presence of a tunneling mechanism causes this phenomenon. Electron connections or electron transfer could arise from two different types of mechanisms; mechanical contact between two conductive particles from which exchange of an electron arises, or by electron tunneling effect which relies on electron hopping. The main point here is that it is possible that a pair of conductive particles dispersed in an insulating polymer can facilitate electron transfer, even if there is no physical connection between them [140–142]. More information regarding the percolation theory can be found in Figure B.2.

After introducing BDD particles in the filament composite, a clear trend was observed which shows a decrease in resistivity with increasing BDD concentration (see Table 5.4a). Starting with 757 Ω -cm for the composite without BDD, the volume resistivity was eventually reduced by 88 % to 92 Ω -cm for the TPU/CNT/BDD (1:2) sample. The BDD particles possibly act as an extended electron traveling network. Their presence within the composite is favorable to the electron transfer kinetics and subsequently increases the conductivity of the sample. Moreover, this effect can possibly be supported by the synergistic effect of the MWCNTs and BDD particles that together form a coherent conductive network, promoting better electron transfer as compared to the MWCNTs by themselves. In general, most researchers reported the use of a single conductive particle in their composite, whereas this research is focused on two. The combination of using a binary conductive particle dispersion has earlier been conceptualized [103]. Kim suggested that the electrical conductivity through the formation of a conductive path is enhanced by the different geometric characteristics of the dispersed particles or distributed clusters. His observations support the results from this study.

An overview of the calculated conductivities obtained from the electrical measurements of the various filaments is presented in Figure 5.14. The highest reported conductivity is for the TPU/CNT/BDD (1:2) sample, which is roughly 1.2 S/m. The composite, containing 10 wt.% of MWCNTs and TPU, was measured with a conductivity of 0.13 S/m, about one order of magnitude lower than the sample with maximum BDD filler content.

Table 5.4: Electrical properties of (a) extruded filament (n=10) and (b) 3-D printed electrodes (n=3).

(a)		(b)	
Filament		3-D printed electrode	
Sample	Volume resistivity ($\Omega\text{-cm}$)	Sample	Resistance ($k\Omega$)
TPU	>200 M	TPU	>200 k
TPU/CNT	757 ± 69	TPU/CNT	22 ± 2.9
TPU/CNT/BDD (2:1)	241 ± 39	TPU/CNT/BDD (2:1)	-
TPU/CNT/BDD (1:1)	181 ± 22	TPU/CNT/BDD (1:1)	4.18 ± 0.86
TPU/CNT/BDD (1:2)	92 ± 9	TPU/CNT/BDD (1:2)	1.58 ± 0.29

Since the electrical conductivity is highly dependent on the degree of homogeneity of the dispersed CNTs, the values reported in the literature concerning the volume resistivity are rather extensive. Kim [103] presented a conductivity of 0.58 S/m for a similar fabricated composite containing 10 wt.% MWCNTs and 90 wt.% of TPU. Other studies, however, revealed values which slightly deviate from the values obtained in this study. Tzounis and colleagues [91] found a conductivity of 20 S/m for a TPU polymer with only 5 wt.% of MWCNTs. Christ et al. [90] revealed that the printing direction is strongly related to the degree of conductivity of the 3-D printed samples, since the printing process imparts some degree of orientation of the MWCNTs in the layer print direction. They reported a conductivity of 2 S/m for their highest loaded TPU/CNT composite, which had 5 wt.% of MWCNTs. Likewise, Podsiadly and colleagues [93] fabricated an ABS/CNT composite that exhibited a conductivity of 6.7 S/m for a 9.1 wt.% loading.

These findings are, in general, at least one order of magnitude higher than the ones obtained from this research, and may be attributed to different things. The first factor is the degree of homogeneity of the dispersed particles, which is highly susceptible to process variations. Ensuring a well-dispersed composite is the main challenge in the fabrication of conductive composites and strongly depends on the mixing conditions. These challenges could therefore explain the wide range of reported values in the literature, which show the high degree of complexity that is involved in their fabrication. The application of SEM should provide a good indication of the dispersion, but does not guarantee complete certainty, since the measurements are generally performed on a localized region. Second, it should be highlighted that the measured electrical properties are highly dependent on the used methodology. For this characterization, a standard two-probe set-up connected to a multimeter was used to measure the sample resistance. To limit the involvement of methodological errors, 10 different samples were each taken from the extruded filament. Still, the used equipment could be replaced by a more advanced set up, such as a two-point probe system with independent current meter and voltage source. In this set-up, different voltages can be applied to the specimen and their respective currents can then be measured, from which the resistivity and conductivity can be calculated. At last, other factors that could affect the differences in measurements are mainly material-related. Variations between the used MWCNTs in terms of size, purity, and surface modifications, may also contribute to the observed conductivity deviations.

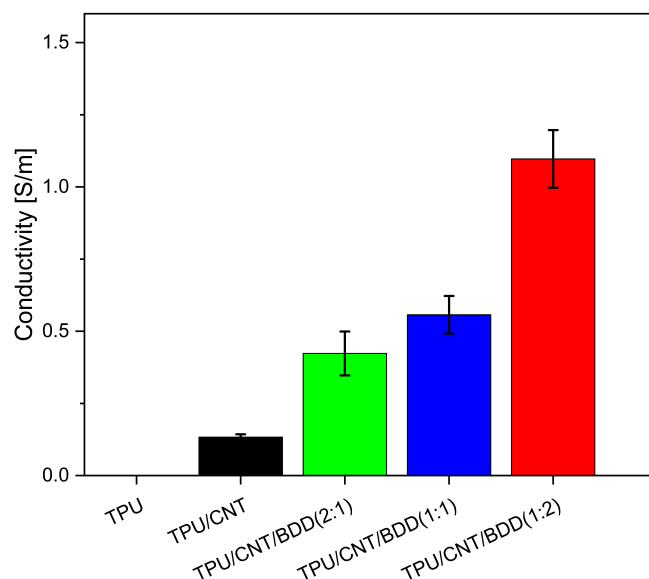


Figure 5.14: Conductivity of the different manufactured filament sample compositions (n=10).

Regarding the measurements performed on the 3-D printed electrodes, their results are presented in [Table 5.4b](#). Unfortunately, due to technical problems with the printer, no samples for the TPU/CNT/BDD(2:1) composition had successfully been printed and could therefore not be evaluated. For all other samples, the resistance was measured in-plane, meaning perpendicular to the electrode surface and through the printed layers (1 mm thickness). The 3-D printed electrode with the highest resistance was TPU/CNT, and was similar to the result obtained from the filament resistivity. Likewise, the lowest reported resistance was measured for the TPU/CNT/BDD(1:2) composition, supporting the trend previously observed with the filament characterization. These results again show a decrease in resistance as the content of BDD increases, with the resistance decreasing 93 % from 22 k Ω to 1.58 k Ω . Together with the results from the filament characterization, these numbers strongly support an increased electron transfer effect due to the presence of the BDD particles. These findings are further investigated, through the use of an electrochemical characterization procedure, in [Section 5.3.5](#).

5.3.4 Morphological and surface characterization

High-magnification SEM images of the four composites and neat TPU can be seen in [Figure 5.15](#), each acquired from a fractured filament cross-section. [Figure 5.15a](#) shows the morphology of the neat TPU while [Figure 5.15b,c,d,e](#) show the morphology of each CNT-containing composite with their respective BDD loadings reported in the figure. The SEM images from the neat TPU present a high degree of smoothness and show a homogeneous surface. In [Figure 5.15b](#), the morphology of the TPU/CNT is presented and a similar degree of smoothness can be observed. In addition, tiny white spots are noticed throughout the material, which are circled in red. These bright spots are often affiliated with conductive particles [90, 92, 96, 143], and represent in these images the presence of CNTs. Moreover, no clear appearance of aggregated or clustered CNTs is noticed, which would imply that the CNTs are homogeneously dispersed. Once the BDD particles are added to the composite, significant changes in the SEM images can be observed. The cross-section surface starts to become more rough, with the roughness gradually increasing with higher BDD concentrations, as shown in [Figure 5.15c,d,e](#). This increase is accompanied by rise in porosity, especially visible in [Figure 5.15d,e](#). Next to that, the BDD particles tend to appear more often with rising filler concentrations and their distribution remains relatively homogeneous. The BDD particles are circled in blue to indicate their presence.

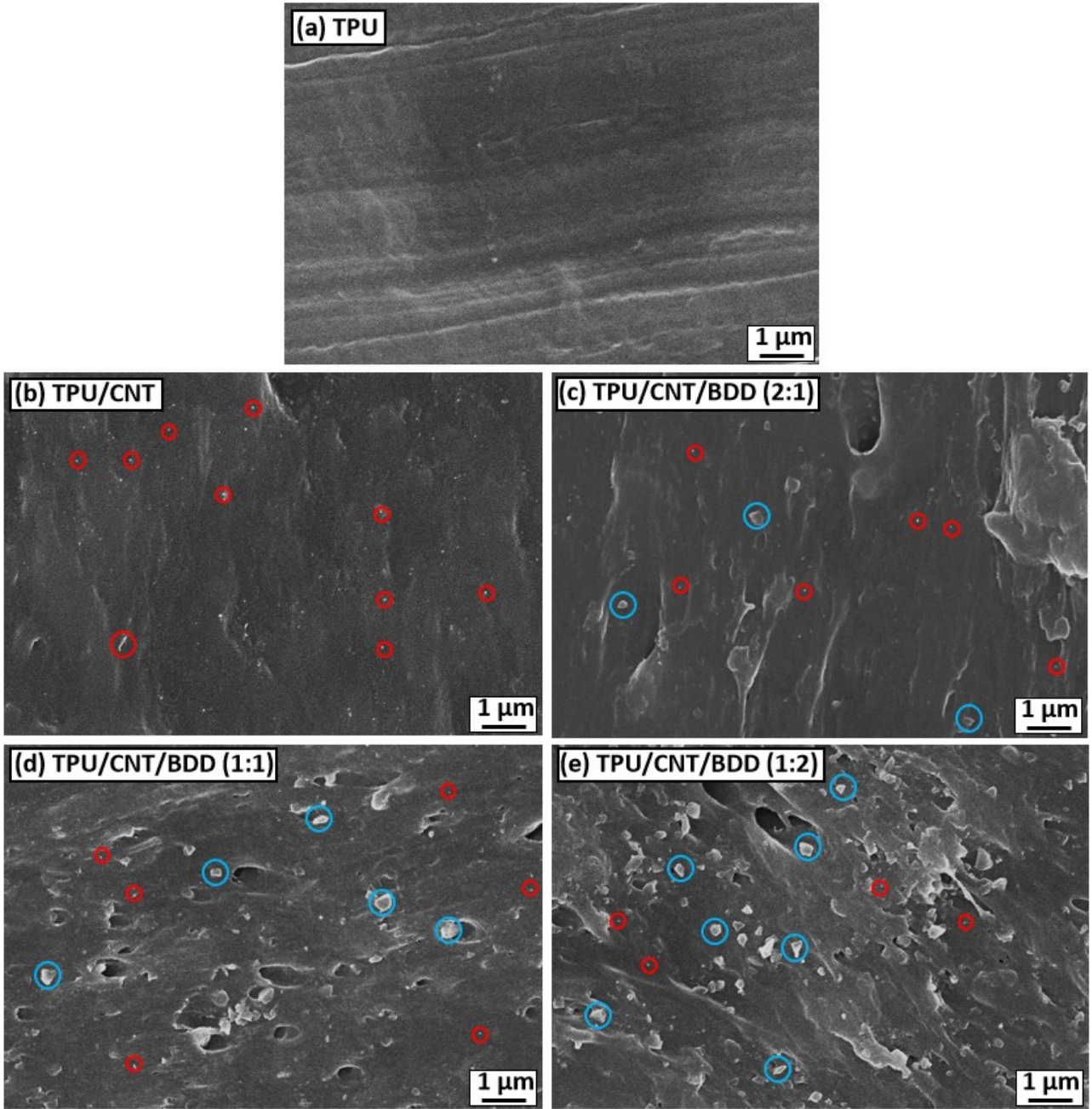


Figure 5.15: Cross-section SEM images of different manufactured TPU-based composites at 10000x magnification.

When comparing both particles, the BDD particles are easier to notice as their size is much larger compared to the CNTs. Consequently, the elevated roughness and porosity previously notified, can logically be attributed to the difference in size and degree of concentration of the particles. The presence of pores had earlier been reported by other researchers [93, 144] and were attributed to the manufacturing procedure. In both examples, the researchers used a similar composite formulation technique as used in this study, and the existence of the pores was likely induced by the evaporation of the solvent. In the same way, multiple studies [92, 96, 109] reported similar porosity in their composite cross-sections. Contrary to the studies that used solvent evaporation, these studies used a different composite formulation technique, namely one which relies on melt-blending and does not involve the use of solvents. It should be emphasized that the occurrence of pores or voids does not necessarily need to be caused by the choice of manufacturing process. The porosity may be a consequence of the particle pull-outs resulting from the cross-section cut.

5.3.5 Electrochemical characterization

To verify previously observed results regarding the electrical properties, the TPU/BDD samples were first subjected to a standard electrochemical measurement set-up using cyclic voltammetry. The results confirmed that the material is indeed too insulating to be used as an electrode material. The CV scans can be found in [Figure B.4](#). Following, three different compositions of as-printed electrodes were used for the electrochemical characterization procedure, namely TPU/CNT, TPU/CNT/BDD(1:1) and TPU/CNT/BDD(1:2).

Electrode surface treatment

During the electrochemical characterization process, it was observed that the as-printed electrodes did not display the desired electrochemical behavior which was expected. Composite electrodes often require surface treatments before sensing applications because the conductive material is covered with the used thermoplastic polymer. Thus, different strategies such as chemical [145–148], biological [149] and electrochemical [150, 151] activations have been developed to partially remove the insulating polymer exposed at the electrode surface. In addition, other, more environmentally friendly approaches have successfully been proposed as well, such as mechanical polishing [145, 151] and thermal annealing [152]. All of these literature studies reported the use of PLA, specifically, as the main polymer in their composite. No reports have so far been published on the use of TPU as the main polymer in 3-D printed electrodes for electrochemical detection.

Before the most suitable electrode treatment procedure was established, different other treatment procedures were also employed. First, an electrochemical treatment was applied to the as-printed electrodes, which has earlier been used [153]. Each electrode was subjected to +1.4 V and -1.0 V in 1 M NaOH for 200 seconds at each potential. No differences in electrochemical response were detected compared to the electrode before treatment. The same experiment was conducted, but this time for 300 seconds at each potential. Still, no changes were observed compared to the initial as-printed electrode response. The particular electrochemical treatment procedure to activate the electrode surface was proven to be effective for PLA-containing composites [145–148, 154]. The NaOH activates the electrodes by saponification of the aliphatic ester groups in PLA, thus exposing more of the conductive particles. The hydroxide groups will break the PLA into smaller polymer chains and ultimately in lactate. TPU is not susceptible to this chemical decomposition process [155], which makes this specific electrochemical treatment not a suitable activation method.

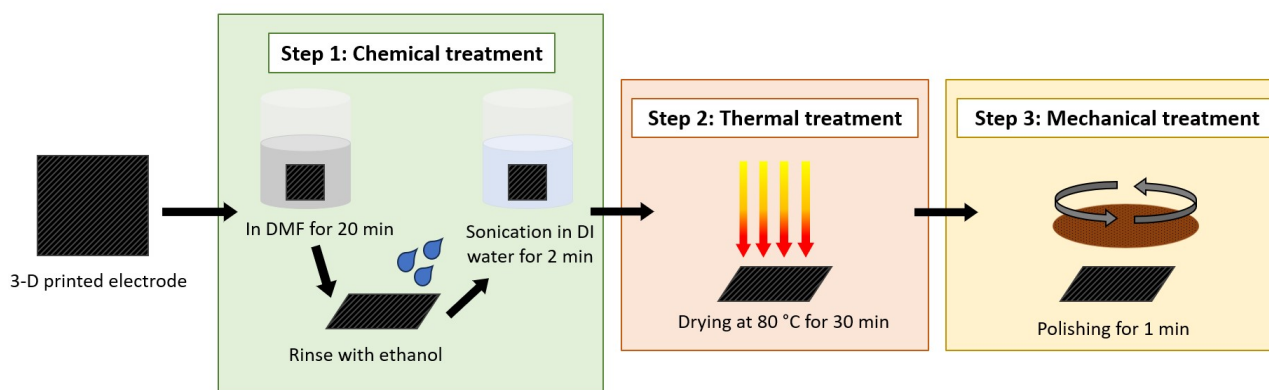


Figure 5.16: Schematic illustration of the electrode surface treatment procedure.

Other treatment procedures were evaluated, and more specifically chemical treatment of the electrode surface. Gusmao and colleagues [146] investigated the effect of five different chemicals on the capacitance and electron transfer of a graphene/PLA electrode. They reported that the responses in ferrocyanide and the supercapacitor properties of the 3-D printed electrodes differ significantly depending on the solvent selected for activation. Polar aprotic solvents (DMF and acetone) presented superior activation capabilities compared to polar protic solvents (ethanol, DI water and methanol). The distinguishing feature is the presence of an -OH group, which is the most common characteristic of a protic solvent. Including the knowledge that was gathered from the composite formulation process, where acetone proved to be very poor in dissolving TPU,

the decision was made to use DMF as chemical for surface activation. Different time periods were investigated (150 s, 300 s, 450 s, 600 s and 1200 s) and considering the rest of the treatment procedures as well, 1200 s proved to be the most effective. After removal from DMF, the electrode was rinsed with ethanol, to remove the excessive DMF [148]. Initially, the electrodes were rinsed with DI water after removal from DMF, but precipitation of TPU at the surface of the electrode was observed [Figure B.7](#). The precipitation was significantly reduced when ethanol was used. Next, the electrodes were sonicated for 2 min in DI water and then placed in an oven at 80 °C for 30 min to remove excessive water. Lastly, the electrodes were polished for roughly 1 minute with a fine-grained (240 grit) sandpaper to smoothen the surface and remove any existing polymer precipitates (see [Figure B.8](#)). Presented in [Figure 5.16](#) is the electrode surface treatment procedure which has been used for this study. This treatment process was also partly inspired by the reported procedures in the literature [156, 157]. After treatment of the electrodes, their size was significantly reduced (visible in [Figure B.9](#)) and also their porosity increased (see [Figure B.10](#)). Still, the electrodes possessed a high degree of flexibility, as can be seen in [Figure 5.17](#), which is an essential property of these 3-D printed composites.

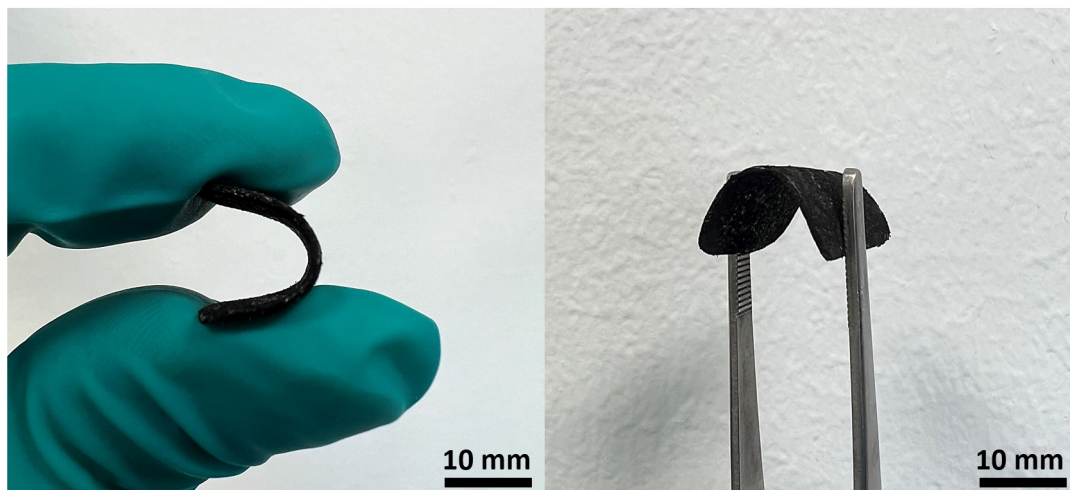


Figure 5.17: Image displaying the degree of flexibility of TPU/CNT/BDD(1:1) after DMF treatment.

Characterization in supporting electrolyte

Before applying any surface treatment, the electrodes were characterized in a supporting electrolyte 0.5 M KNO_3 and their cyclic voltammetry responses are presented in [Figure 5.18a](#). From this graph, we notice that the background current for the BDD-containing samples is higher than without BDD. Moreover, the measured currents are higher for the BDD-containing electrodes compared to the TPU/CNT electrode. This indicates that the addition of BDD, definitely promotes electron transfer, which results in the BDD-containing electrodes to be more conductive compared to the one without. Nevertheless, we can observe that the measured currents of the TPU/CNT/BDD(1:1) and the TPU/CNT/BDD(1:2) are very much alike. The findings reported here follow the same trend as the results obtained for the investigated electrical properties, which imply that BDD particles enhance the conductivity. Presented in [Figure 5.18b](#) are the cyclic voltammograms of the three samples treated with DMF for 20 minutes. As can be seen, the treated TPU/CNT electrode (red line) still provided the lowest background currents compared to the other two BDD-containing electrodes. When the BDD was added to the electrodes, an increase in conductivity and background current was observed with increasing BDD content. Even though this behavior was not observed for the untreated electrodes, after the treatment procedure, the electrodes tend to show similar conductive behavior as to what was witnessed in the electrical characterization ([Table 5.4](#)) and follow the same trend. Comparing the untreated samples with the treated electrodes, there is significant increase in measured current for the treated samples. This is explained by the treatment process, where solvent immersion and polishing was used, which ensures a smoother surface and aims to expose conductive particles by removing excessive polymer. Moreover, the immersion in DMF may also contribute to an increase in porosity of the treated electrodes. This would allow for more surface to be involved in the electrochemical reaction, providing higher activity and thus possibly promoting the electrical conductivity. Optical images presented in [Figure B.10](#) present the effect of treatment on the surface morphology of each composite sample.

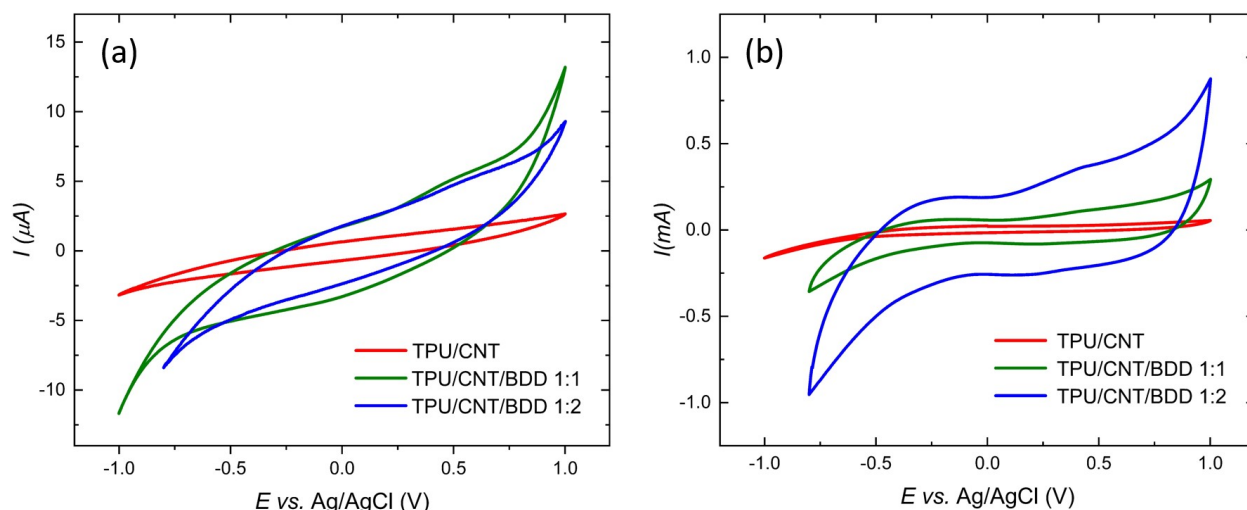


Figure 5.18: Cyclic voltammograms of 0.5 M KNO_3 , recorded on (a) untreated and (b) treated electrodes. Scan rate: 100 mV/s.

The corresponding double-layer capacitances (C_{dl}) were calculated (see Equation 4.2) from the CV curves for all electrodes, as summarized in Table 5.5. The overall observed trends are consistent with the results from the CVs. For all electrodes, a significant increase in C_{dl} values was observed. For the untreated TPU/CNT/BDD(1:1) and TPU/CNT/BDD(1:2) electrodes, the evaluated C_{dl} are in line with the observed behavior from Figure 5.18, which concluded only a slightly better conductivity for the TPU/CNT/BDD(1:1) electrode. Nevertheless, once we compare the two capacitances after the treatment of the electrodes, much more prominent differences are revealed; in particular, the C_{dl} for TPU/CNT/BDD(1:2) electrode shows a significant increase (4500 vs 1440 $\mu\text{F}\cdot\text{cm}^{-2}$) compared to the TPU/CNT/BDD(1:1) electrode. This observation is correlated to the earlier presented conductivity results which confirm that the surface treatment of the electrodes will at first, increase the conductivity, and secondly, strongly emphasize the difference in composition of the two BDD-containing electrodes with their subsequent effects. Gusmao and colleagues [146] reported findings that support these results regarding the treatment effects on the double-layer capacitance. Their research revealed that the double-layer capacitance of each electrode strongly depended on the choice of solvent. They reported C_{dl} values in the range of 1 to 10 $\text{mF}\cdot\text{cm}^{-2}$ for their samples treated in DMF. The recorded increase in capacitance between the treated and untreated electrodes was on average 1250%, whereas the enhancement was much stronger in this study (24900% for the TPU/CNT/BDD(1:2)). These differences are likely attributed to time of immersion, which was only 7 minutes [146] compared to 20 minutes in this study. The TPU/CNT electrodes show a much smaller capacitance, for both treated and the untreated samples, which is most likely due to the absence of the BDD particles. Again, the presence of BDD particles seems to introduce appealing electrochemical behavior, which intensifies with an increase in the BDD-content.

Table 5.5: Calculated double layer capacitance for untreated and treated electrodes in KNO_3 (-0.5 V – 0.5 V). Calculated electrochemical active surface area for treated electrodes.

Sample name	Untreated	Treated	
	C_{dl} ($\mu\text{F}\cdot\text{cm}^{-2}$)	C_{dl} ($\mu\text{F}\cdot\text{cm}^{-2}$)	A_{eff} (cm^2)
TPU/CNT	6	376	0.35
TPU/CNT/BDD (1:1)	23	1440	0.71
TPU/CNT/BDD (1:2)	18	4500	0.91

Characterization with standard redox markers

The electrochemical properties of the 3-D printed composite electrodes were evaluated using two commonly used redox markers, $[\text{Ru}(\text{NH}_3)_6]^{3+/2+}$ (RuHex) and $[\text{Fe}(\text{CN})_6]^{3-/4-}$ (ferrocyanide). Their electrochemical behavior is investigated by cyclic voltammetry and is presented in Figure 5.19. In general, all presented graphs display better developed peaks with surface treatment, compared to no treatment. In addition to that, the TPU/CNT and TPU/CNT/BDD(1:2) electrodes present for both for redox probes better visible peak appearance once the treatment was extended from 10 minutes to 20 minutes. Moreover, these samples recorded higher currents and exhibited higher background currents, which can be devoted to the removal of insulating polymer at the surface, and thus exposing the BDD and CNT particles. Contrary to the effect previously observed, the CV graph of the TPU/CNT/BDD(1:1) in ferrocyanide (Figure 5.19d) implies, that 20 minutes of treatment surprisingly start to reduce the background current, and generates more poorly developed peaks. For the RuHex marker, there is only a small difference observed in the peak distribution and height for the 10 and 20 minute treatment (Figure 5.19c). Thus, 10 minutes of treatment seems to be already sufficient for the TPU/CNT/BDD(1:1) composite.

Moreover, it is important to distinguish between the two redox probes in terms of their electron transfer mechanism. Where RuHex promotes outer-sphere reactions and their electrons exchange is based upon a tunneling mechanism, ferrocyanide is surface sensitive and promotes inner-sphere reactions that rely on direct interaction with the electrode surface for electrons exchange. The obtained CV data from the samples recorded in RuHex (displayed in Figure 5.19a,c,e) present well-developed peaks for all three treated electrodes, with the two BDD-containing electrodes displaying even stronger peak development. The CV scans of the three electrode composition recorded in ferrocyanide is presented Figure 5.19b,d,f. Overall, the graphs present more poorly developed peaks and show a weaker electrochemical response to the recorded redox probe. For ferrocyanide, only the TPU/CNT/BDD(1:1) sample, presented in Figure 5.19d, displays a strong peak development. The differences in peak development of the tested samples for RuHex and ferrocyanide can be attributed to their difference in electron transfer mechanism. Due to the surface sensitivity of ferrocyanide, variations in the electrode surface, such as roughness and porosity, may contribute to the relatively poor electrochemical response as compared to RuHex. The variations in electrode surface are mainly caused by the different operations in the surface treatment process.

Since electrical conductivity is obtained in the composite via CNT and BDD percolation paths, the influence of the concentration of BDD in two redox markers is illustrated in Figure 5.20a for RuHex and Figure 5.20b for ferrocyanide. The cyclic voltammetry analysis in both graphs reveals more ill-shaped signals with smaller current intensities without the addition of BDD fillers, which is expected, considering the higher resistivity of the TPU/CNT sample (Table 5.4). As mentioned, the TPU/CNT composite was taken as the basis for the BDD additions. The addition of any amount of BDD (9.1 and 16.7 wt.%), resulted in a significant enhancement of the redox processes, which manifested as a considerable increase in anodic peak current ($i_{P,A}$) and cathodic peak current ($i_{P,C}$) for RuHex. For example, the $i_{P,A}$ value reaches 54.86 μA for the TPU/CNT/BDD(1:1) and 34.19 μA for the TPU/CNT/BDD(1:2), more than 2X higher compared to the original TPU/CNT. Remarkably, even though the TPU/CNT contains 10 wt.% of conductive CNTs, the obtained current peaks are still higher for the TPU/CNT/BDD(1:1) and TPU/CNT/BDD(1:2), containing lower loadings (9.1 and 9.5 wt.%, respectively) of CNTs. This effect can, similarly to the results presented in Section 5.3.3, be associated with the synergistic behavior of the MWCNTs and BDD particles that together form a coherent conductive network, promoting better electron transfer as compared to the MWCNTs by themselves.

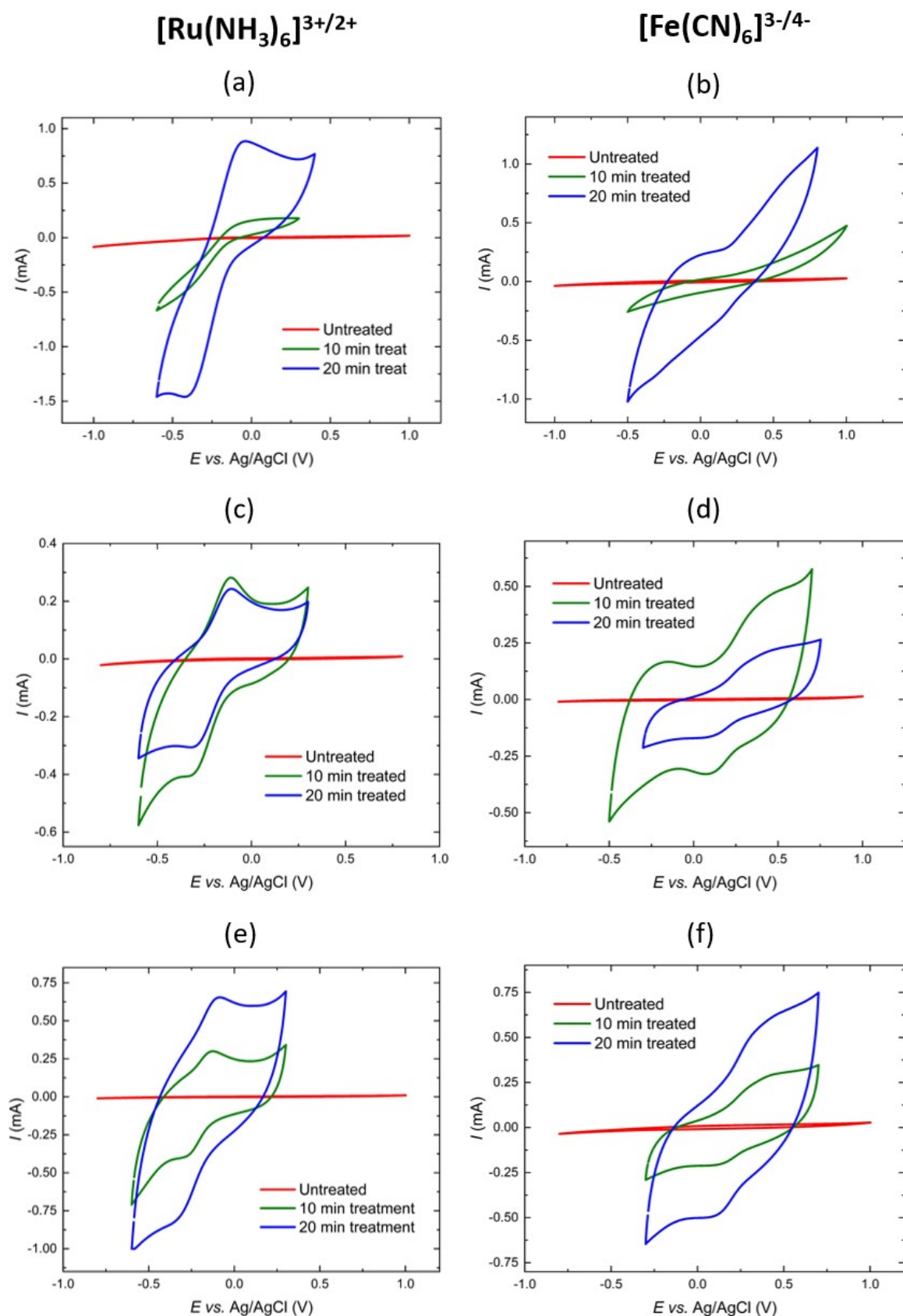


Figure 5.19: Cyclic voltammograms recorded in the solutions of 1mM RuHex in 0.5 M KNO_3 (a,c,e) and 1mM ferrocyanide in 0.5 M KNO_3 (b,d,f) on the following electrodes: TPU/CNT (a,b), TPU/CNT/BDD(1:1) (c,d), and TPU/CNT/BDD(1:2) (e,f). Scan rate is 100 mV/s.

Concerning the measurements in a ferrocyanide solution, a vast increase in peak current intensities is also visible (Figure 5.20b). For the TPU/CNT electrode, no peak parameters could be measured from the obtained CVs at 10 mV/s, due to the poorly developed shape of the CV. The $i_{p,A}$ value reaches 43.2 μA for the TPU/CNT/BDD(1:1) and 62.06 μA for the TPU/CNT/BDD(1:2), and are visibly better developed than for the TPU/CNT. This behavior corresponds to an earlier reported study, conducted by Cieslik and colleagues [150], who investigated the addition of detonation nanodiamonds (DNDs) and boron-doped carbon nanowalls (BCNWs) to a 3-D printed PLA/CB electrode. They also observed an increase in peak height and reported better developed peaks for ferrocyanide when their PLA/CB composites were enriched with 5 wt.% of DNDs and BCNWs. This effect was caused by lower redox activation overpotential at the DND electrode surface compared to the CB.

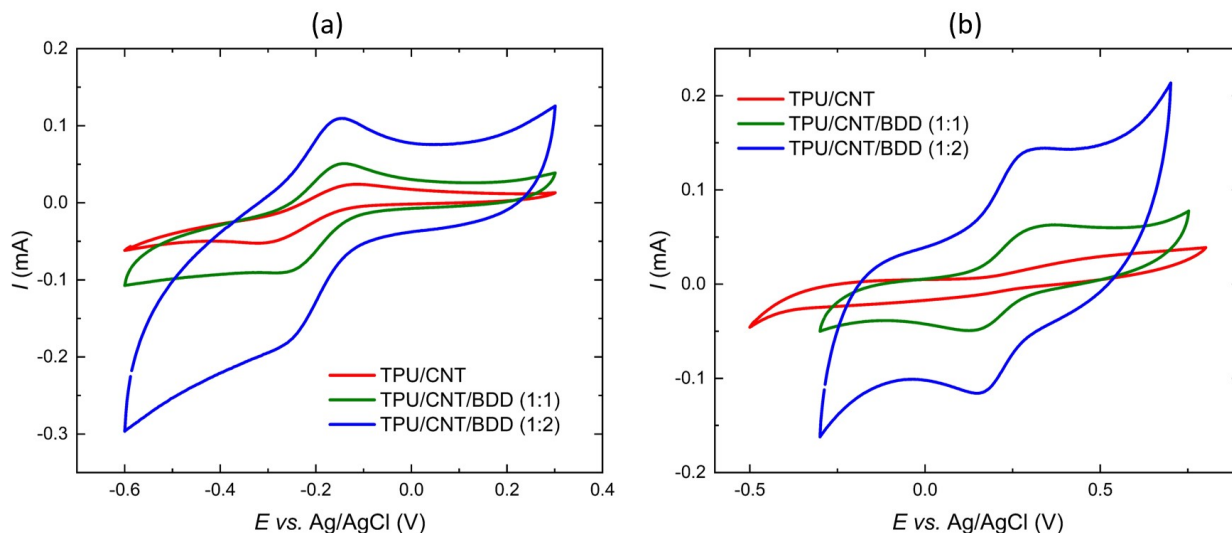


Figure 5.20: Cyclic voltammograms recorded on all three electrodes after 20 min treatment in the presence of: (a) 1 mM RuHex and (b) 1 mM ferrocyanide in 0.5 M KNO_3 . Scan rate: 10 mV/s.

The most valuable parameter, i.e., the peak-to-peak separation (ΔE_p), serves as electron transfer rate indicator and was determined from the measurements. A prominent drop in ΔE_p was noticed in both composite formulations for RuHex redox marker for 10 mV/s. From 178 mV, it decreased to 127 mV and 110 mV for TPU/CNT/BDD(1:1) and TPU/CNT/BDD(1:2) respectively, indicating a more reversible charge transfer mechanism and faster electron transfer kinetics. In addition, a scan rate study was performed (presented in Figure B.5) for both redox markers to investigate the effect of scan rate on the electrochemical response, more specifically in terms of peak separation and peak height. The scan rate study performed with RuHex was, due to better reversibility parameters and much better developed pairs of redox peaks, used to determine the effective electrode surface area (A_{eff}) using Equation 4.3. Presented in Figure B.6 are the graphs presenting the linear relationship between the $i_{p,C}$ and square root of scan rate, which confirm that the redox processes of RuHex are controlled by diffusion. The slope value of the linear relationship is also used in Equation 4.3. The results for the calculated A_{eff} are presented in Table 5.5. The value obtained for the TPU/CNT electrode is 0.354 cm^2 , which is almost 3 times lower than the geometric surface area ($A_{\text{geom}} = 1 \text{ cm}^2$). When comparing the TPU/CNT electrode to the other two BDD-containing values, it is clear these electrodes have stronger electrochemical activity at their surface. The A_{eff} calculated for the TPU/CNT/BDD(1:1) composite is twice the value of the TPU/CNT, whereas the TPU/CNT/BDD(1:2) electrode has an electroactive surface area almost three times the size of the TPU/CNT electrode. This effect can be supported by the enhanced electrical conductivity earlier discussed in Section 5.3.3, but can also be related to the increase in porosity of the electrodes (see Figure B.10). In particular, the TPU/CNT/BDD(1:2) reports the highest A_{eff} of all three samples, and interestingly also presented the highest degree of porosity after treatment (Figure B.10).

The variations in ΔE_p evaluated for RuHex and ferrocyanide as a function of the scan rate for all three samples are presented in Figure 5.21 and Figure B.11, respectively. In general, a low ΔE_p is associated with good reversibility, better electrode quality and faster electron transfer kinetics. For all measured scan rates presented in Figure 5.21, the TPU/CNT electrode supports a significant worse reversibility of the redox

reaction compared to the TPU/CNT/BDD(1:1) and TPU/CNT/BDD(1:2). Moreover, both BDD-containing composites present a higher degree of reversibility for every scan rate and can therefore be considered more efficient electrodes. These results clearly demonstrate the enhancing effect of the addition of BDD-particles to TPU/CNT composite, and thus result in better reversibility.

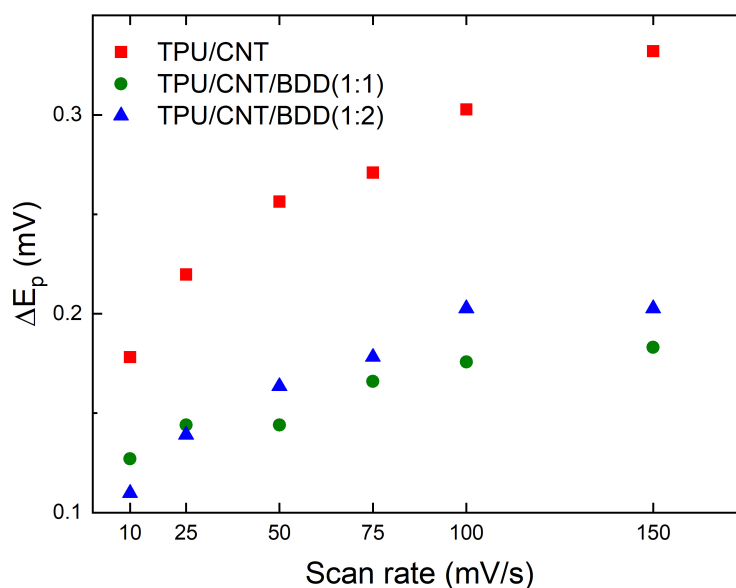


Figure 5.21: Plots of ΔE_p versus the scan rate recorded in 1mM RuHex in 0.5M KNO_3 .

Detection of organic analyte

Finally, the 3-D printed composite electrodes, namely TPU/CNT, TPU/CNT/BDD(1:1) and TPU/CNT/BDD(1:2) each treated for 20 minutes, were evaluated for electrochemical detection of 1mM dopamine in a PBS solution (10 mM, pH 7.4). Dopamine was selected due to its biologically relevant role in the human body, as it is an important neurotransmitter and is a commonly detected compound in the literature [150, 158, 159] with a well-known redox mechanism. Presented in Figure 5.22 are the DPV graphs of each of the tested composites, with the corresponding oxidation peak heights. No oxidation peak was observed for the TPU/CNT electrode, only a minor increase in measured current of 300 nA. Addition of the BDD shows significant improvement of the detection of dopamine, and well-developed peaks appear. The oxidation peak for TPU/CNT/BDD(1:1) is positioned at +0.173 V and reaches a peak height of 10.9 μA . In comparison, the oxidation peak of TPU/CNT/BDD(1:2) is situated around +0.142 V with a peak height of 7.5 μA . Both BDD-containing electrodes present detection of the organic analyte of dopamine at similar potential, with the TPU/CNT/BDD(1:1) presenting a slightly higher, better developed oxidation peak, and a more stable response. It should be mentioned that the detection of dopamine is, similar to ferrocyanide, surface sensitive. More specifically, both promote inner-sphere reactions and their electrons exchange strongly depends on the electrode surface [160]. Therefore, the effect of porosity of the electrode may likely be involved in the degree of detection. Supported by optical microscopy images, the increased porosity of the TPU/CNT/BDD(1:2) electrode could very likely be one of the reasons for the deviation and could additionally explain the presence of varying currents at elevated voltages.

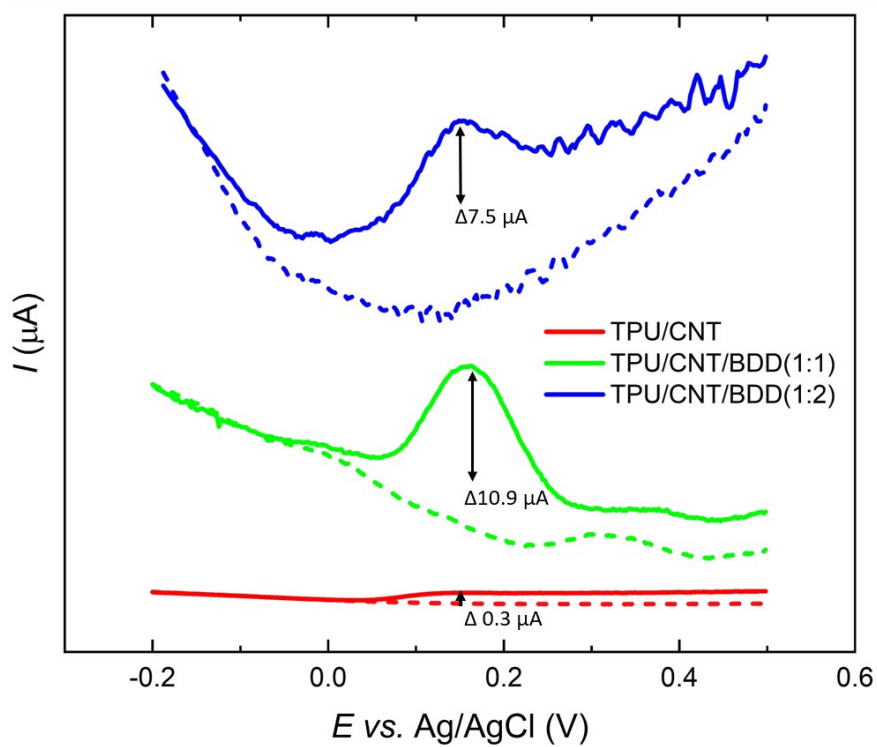


Figure 5.22: DPV scans for 1 mM dopamine in PBS (10 mM, pH 7.4) for different composite electrodes: (red) TPU/CNT, (green) TPU/CNT/BDD(1:1), and (blue) TPU/CNT/BDD(1:2). The dashed line corresponds to supporting electrolyte.

6 Conclusion and Outlook

This study examined the mechanical, morphological, electrical and electrochemical behavior of different manufactured, BDD-based 3-D printed composites. The primary conclusions drawn from this study are summarized as follows:

6.1 Powder characterization

- Both BDD powders presented significant levels of sp^3 in their material composition.
- The Boromond BDD powder presented a negligible amount of boron, whereas the Ultrahard BDD powder did present an asymmetric diamond line, combined with a weak 500 cm^{-1} band that could indicate low boron doping levels.
- Both BDD powders had dimensions which were in the sub-micron range, with the Ultrahard BDD particles being slightly smaller.
- Both BDD powders presented a high degree of electrical resistance (i.e., $>200\text{ M}\Omega$), which forced an adjustment of the composite composition by introducing CNTs.

6.2 SLA-printed composites

- SLA-printed composites presented an excellent, smooth surface after printing.
- The addition of BDD particles enforces the polymer's properties by an increase in Young's modulus (44 % and 75 %) and tensile strength (92% and 81 %) both for UDR-7.5 and BDR-12.5, respectively.
- The effect of post-treatment in terms of annealing and curing significantly increases the mechanical properties, to such an extent that adding BDD particles only reduced the composite's mechanical characteristics.
- 12.5 wt.% was the highest achievable loading of BDD particles that could be introduced without adjusting the photopolymer composition.

6.3 FDM-printed composites

- FDM allows higher wt.% of BDD particles to be introduced in the polymer as compared to SLA (40 wt.% vs 12.5 wt.%).
- The composite formulation process requires close monitoring of all process parameters (stirring speed, stirring time, stirring temperature) to ensure a homogeneous, well-dispersed composite.
- Optimizing the 3-D printing process and applying specific adjustments to the 3-D printer, such as nozzle diameter, printing temperature and printing speed, need to be carefully considered when printing with high-loaded composites.
- Obtaining a constant and correct filament diameter is essential in the process of 3-D printing with composites, and needs to be carefully monitored by controlling speed and temperature during the extrusion-based fabrication process.

- From mechanical observations, all FDM-printed composites containing BDD showed an increase in Young's modulus and saw a decline in elongation at break, which is attributed to the increased filler concentration and polymer-BDD connections.
- The presence of BDD particles in the TPU/CNT composite clearly enhanced the electrical conductivity, which indicates a better electron transfer even though the CNT concentration was reduced.
- Surface treatment is crucial when working with 3-D printed electrodes for electrochemical sensing purposes and was achieved by a sequential chemical, thermal and mechanical treatment.
- The addition of BDD particles allowed the 3-D printed electrode to successfully detect dopamine as compared to the electrodes without BDD particles, which emphasizes the essential presence of the particles.
- Both BDD-containing electrodes achieved successful detection of dopamine. The TPU/CNT/BDD(1:1) electrode achieved a slightly higher peak response ($10.9 \mu\text{A}$ vs $7.5 \mu\text{A}$) which may be induced by an increase in porosity of the TPU/CNT/BDD(1:2) electrode surface.

6.4 Recommendations for future work

- Since the currently employed BDD particles present a low degree of boron doping (i.e., 300 – 710 ppm), it needs to be validated whether the increase in electrical and electrochemical behavior is attributed to the boron doping, or not. Therefore, I suggest a composite formulation where BDD is replaced by undoped micro or nanodiamond to verify the effect of boron doping.
- More attention needs to be paid towards optimizing the filament and 3-D printing process, as these are in general very susceptible to errors and may restrict the production of the electrodes. Among others, the extrusion speed and temperature, but also the 3-D printing parameters, such as printing temperature, printing speed and layer thickness.
- More work needs to be done on the composition of the current composites and how different ratios of CNTs and BDD affect the electrical and electrochemical properties.
- Additional mechanical characterization of the TPU/CNT/BDD composites is needed to study the effects of the two fillers on the mechanical properties, since CNTs are in general significantly softer as compared to diamond particles. Also, the effect on the flexibility of each of the compositions needs to be further investigated.
- The electrode surface treatment procedure might also be optimized, as the current established procedure has been developed in a very short period of time. Prolonging the immersion in DMF is a suggestion to see how long it will take before the electrodes really start to degrade. Also, the heat treatment procedure requires a more sophisticated investigation. A suggestion would be to modify the temperature and time of heat exposure.
- It is recommended to adjust the resin composition of the SLA-composites in order to achieve better curability and subsequently achieve higher weight percent of fillers that can be introduced. The addition of photoinitiator to the current resin formulation would allow the composite to accomplish better curing, which is currently restricted by the added BDD particles.

Bibliography

- [1] Chris J.H. Wort and Richard S. Balmer. "Diamond as an electronic material". en. In: *Materials Today* 11.1-2 (Jan. 2008), pp. 22–28. ISSN: 13697021. DOI: [10.1016/S1369-7021\(07\)70349-8](https://doi.org/10.1016/S1369-7021(07)70349-8). URL: <https://linkinghub.elsevier.com/retrieve/pii/S1369702107703498> (visited on 11/14/2022).
- [2] Paul W. May. "Diamond thin films: a 21st-century material". en. In: *Philosophical Transactions of the Royal Society of London. Series A: Mathematical, Physical and Engineering Sciences* 358.1766 (Jan. 2000). Ed. by J. M. T. Thompson, pp. 473–495. ISSN: 1364-503X, 1471-2962. DOI: [10.1098/rsta.2000.0542](https://doi.org/10.1098/rsta.2000.0542). URL: <https://royalsocietypublishing.org/doi/10.1098/rsta.2000.0542> (visited on 10/14/2022).
- [3] Abha Misra et al. "Hexagonal diamond synthesis on h-GaN strained films". en. In: *Applied Physics Letters* 89.7 (Aug. 2006), p. 071911. ISSN: 0003-6951, 1077-3118. DOI: [10.1063/1.2218043](https://doi.org/10.1063/1.2218043). URL: <http://aip.scitation.org/doi/10.1063/1.2218043> (visited on 11/10/2022).
- [4] Ravi Divakaran. *In diamond cubic unit cell alternate tetrahedral voidposition are also occupied*. 2020. URL: <https://www.quora.com/In-Diamond-Cubic-Unit-Cell-Alternate-Tetrahedral-voidposition-are-also-occupied-Can-anyone-tell-me-how-to-visualise-alternate-Tetrahedral-void-position>.
- [5] Ansys. *GRANTA EduPack software*. 2022. URL: www.ansys.com/materials.
- [6] Sharif Khan. *Difference Between Diamond and Graphite*. 2021. URL: <https://www.petrageoms.com/blog/difference-between-diamond-and-graphite/>.
- [7] K. Nassau and J. Nassau. "The history and present status of synthetic diamond". en. In: *Journal of Crystal Growth* 46.2 (Feb. 1979), pp. 157–172. ISSN: 00220248. DOI: [10.1016/0022-0248\(79\)90052-6](https://doi.org/10.1016/0022-0248(79)90052-6). URL: <https://linkinghub.elsevier.com/retrieve/pii/0022024879900526> (visited on 11/11/2022).
- [8] *Diagrams representing the positions of the atoms in diamond and graphite*. 2013. URL: lucychemistry.blogspot.com.
- [9] Larissa F. Dobrzynetska. "Microdiamonds — Frontier of ultrahigh-pressure metamorphism: A review". en. In: *Gondwana Research* 21.1 (Jan. 2012), pp. 207–223. ISSN: 1342937X. DOI: [10.1016/j.gr.2011.07.014](https://doi.org/10.1016/j.gr.2011.07.014). URL: <https://linkinghub.elsevier.com/retrieve/pii/S1342937X11002061> (visited on 11/14/2022).
- [10] Smithson Tennant. "Iv. on the nature of the diamond". In: *Philosophical Transactions of the Royal Society of London* 87 (1797), pp. 123–127. DOI: [10.1098/rstl.1797.0005](https://doi.org/10.1098/rstl.1797.0005).
- [11] Amanda M. Schrand, Suzanne A. Ciftan Hens, and Olga A. Shenderova. "Nanodiamond Particles: Properties and Perspectives for Bioapplications". en. In: *Critical Reviews in Solid State and Materials Sciences* 34.1-2 (May 2009), pp. 18–74. ISSN: 1040-8436, 1547-6561. DOI: [10.1080/10408430902831987](https://doi.org/10.1080/10408430902831987). URL: <https://www.tandfonline.com/doi/full/10.1080/10408430902831987> (visited on 11/16/2022).
- [12] Sally Eaton-Magana, James E. Shigley, and Christopher M. Breeding. "Observations on HPHT-Grown Synthetic Diamonds: A Review". In: *Gems & Gemology* 53.3 (Nov. 2017), pp. 262–284. ISSN: 0016626X. DOI: [10.5741/GEMS.53.3.262](https://doi.org/10.5741/GEMS.53.3.262). URL: <https://www.gia.edu/gems-gemology/fall-2017-observations-hpht-grown-synthetic-diamonds> (visited on 11/17/2022).
- [13] Ulrika F. S. D'Haenens-Johansson, James E. Butler, and Andrey N. Katrusha. "Synthesis of Diamonds and Their Identification". en. In: *Reviews in Mineralogy and Geochemistry* 88.1 (July 2022), pp. 689–753. ISSN: 1529-6466. DOI: [10.2138/rmg.2022.88.13](https://doi.org/10.2138/rmg.2022.88.13). URL: <https://pubs.geoscienceworld.org/rimg/article/88/1/689/614940/Synthesis-of-Diamonds-and-Their-Identification> (visited on 11/16/2022).
- [14] Kenji K. Hirakuri et al. "Influence of the methane concentration on HF-CVD diamond under atmospheric pressure". en. In: *Vacuum* 63.3 (Aug. 2001), pp. 449–454. ISSN: 0042207X. DOI: [10.1016/S0042-207X\(01\)00365-7](https://doi.org/10.1016/S0042-207X(01)00365-7). URL: <https://linkinghub.elsevier.com/retrieve/pii/S0042207X01003657> (visited on 11/14/2022).

- [15] K. Fabisiak et al. "The influence of working gas on CVD diamond quality". en. In: *Materials Science and Engineering: B* 177.15 (Sept. 2012), pp. 1352–1357. ISSN: 09215107. DOI: 10.1016/j.mseb.2011.12.013. URL: <https://linkinghub.elsevier.com/retrieve/pii/S0921510711005289> (visited on 11/14/2022).
- [16] Jian-guo Zhang et al. "Effect of deposition parameters on micro- and nano-crystalline diamond films growth on WC–Co substrates by HFCVD". en. In: *Transactions of Nonferrous Metals Society of China* 24.10 (Oct. 2014), pp. 3181–3188. ISSN: 10036326. DOI: 10.1016/S1003-6326(14)63458-0. URL: <https://linkinghub.elsevier.com/retrieve/pii/S1003632614634580> (visited on 11/14/2022).
- [17] Jean-Charles Arnault, Samuel Saada, and Victor Ralchenko. "Chemical Vapor Deposition Single-Crystal Diamond: A Review". en. In: *physica status solidi (RRL) – Rapid Research Letters* 16.1 (Jan. 2022), p. 2100354. ISSN: 1862-6254, 1862-6270. DOI: 10.1002/pssr.202100354. URL: <https://onlinelibrary.wiley.com/doi/10.1002/pssr.202100354> (visited on 01/17/2023).
- [18] J. E. Field, ed. *The Properties of natural and synthetic diamond*. London ; San Diego: Academic Press, 1992. ISBN: 978-0-12-255352-3.
- [19] J. P. Goss, R. J. Eyre, and P. R. Briddon. "Theoretical models for doping diamond for semiconductor applications". en. In: *physica status solidi (b)* 245.9 (Sept. 2008), pp. 1679–1700. ISSN: 03701972, 15213951. DOI: 10.1002/pssb.200744115. URL: <https://onlinelibrary.wiley.com/doi/10.1002/pssb.200744115> (visited on 11/22/2022).
- [20] Yuting Zheng et al. "Diamond with nitrogen: states, control, and applications". en. In: *Functional Diamond* 1.1 (Jan. 2021), pp. 63–82. ISSN: 2694-1112, 2694-1120. DOI: 10.1080/26941112.2021.1877021. URL: <https://www.tandfonline.com/doi/full/10.1080/26941112.2021.1877021> (visited on 11/22/2022).
- [21] Michael N. R. Ashfold et al. "Nitrogen in Diamond". en. In: *Chemical Reviews* 120.12 (June 2020), pp. 5745–5794. ISSN: 0009-2665, 1520-6890. DOI: 10.1021/acs.chemrev.9b00518. URL: <https://pubs.acs.org/doi/10.1021/acs.chemrev.9b00518> (visited on 11/21/2022).
- [22] Allan Collins. "The optical and electronic properties of semiconducting diamond". en. In: *Philosophical Transactions of the Royal Society of London. Series A: Physical and Engineering Sciences* 342.1664 (Feb. 1993), pp. 233–244. ISSN: 0962-8428, 2054-0299. DOI: 10.1098/rsta.1993.0017. URL: <https://royalsocietypublishing.org/doi/10.1098/rsta.1993.0017> (visited on 11/21/2022).
- [23] E.A. Burgemeister. "Thermal conductivity of natural diamond between 320 and 450 K". en. In: *Physica B+C* 93.2 (Feb. 1978), pp. 165–179. ISSN: 03784363. DOI: 10.1016/0378-4363(78)90123-7. URL: <https://linkinghub.elsevier.com/retrieve/pii/0378436378901237> (visited on 11/22/2022).
- [24] Jan Isberg et al. "High Carrier Mobility in Single-Crystal Plasma-Deposited Diamond". en. In: *Science* 297.5587 (Sept. 2002), pp. 1670–1672. ISSN: 0036-8075, 1095-9203. DOI: 10.1126/science.1074374. URL: <https://www.science.org/doi/10.1126/science.1074374> (visited on 11/22/2022).
- [25] Satoshi Koizumi et al., eds. *Power electronics device applications of diamond semiconductors*. Woodhead Publishing series in electronic and optical materials. Duxford [England] ; Cambridge, MA: Woodhead Publishing, 2018. ISBN: 978-0-08-102183-5.
- [26] Hitoshi Umezawa. "Recent advances in diamond power semiconductor devices". en. In: *Materials Science in Semiconductor Processing* 78 (May 2018), pp. 147–156. ISSN: 13698001. DOI: 10.1016/j.mssp.2018.01.007. URL: <https://linkinghub.elsevier.com/retrieve/pii/S1369800117322217> (visited on 11/24/2022).
- [27] Michael W. Geis et al. "Progress Toward Diamond Power Field-Effect Transistors". en. In: *physica status solidi (a)* 215.22 (Nov. 2018), p. 1800681. ISSN: 18626300. DOI: 10.1002/pssa.201800681. URL: <https://onlinelibrary.wiley.com/doi/10.1002/pssa.201800681> (visited on 11/24/2022).
- [28] R.S Balmer et al. "Unlocking diamond's potential as an electronic material". en. In: *Philosophical Transactions of the Royal Society A: Mathematical, Physical and Engineering Sciences* 366.1863 (Jan. 2008), pp. 251–265. ISSN: 1364-503X, 1471-2962. DOI: 10.1098/rsta.2007.2153. URL: <https://royalsocietypublishing.org/doi/10.1098/rsta.2007.2153> (visited on 11/24/2022).
- [29] C. Descamps et al. "Nitrogen-doped diamond: Thermoluminescence and dosimetric applications". en. In: *Diamond and Related Materials* 15.4-8 (Apr. 2006), pp. 833–837. ISSN: 09259635. DOI: 10.1016/j.diamond.2005.12.042. URL: <https://linkinghub.elsevier.com/retrieve/pii/S0925963505006412> (visited on 11/22/2022).

- [30] Mitsuhiro Kataoka et al. "Thermionic electron emission from nitrogen-doped homoepitaxial diamond". en. In: *Diamond and Related Materials* 19.2-3 (Feb. 2010), pp. 110–113. ISSN: 09259635. DOI: [10.1016/j.diamond.2009.09.002](https://doi.org/10.1016/j.diamond.2009.09.002). URL: <https://linkinghub.elsevier.com/retrieve/pii/S0925963509002465> (visited on 11/22/2022).
- [31] Daria Majchrowicz et al. "Nitrogen-Doped Diamond Film for Optical Investigation of Hemoglobin Concentration". en. In: *Materials* 11.1 (Jan. 2018), p. 109. ISSN: 1996-1944. DOI: [10.3390/ma11010109](https://doi.org/10.3390/ma11010109). URL: <http://www.mdpi.com/1996-1944/11/1/109> (visited on 11/22/2022).
- [32] Mark J. Jackson and Waqar Ahmed. "Fabrication and wear of nitrogen-doped diamond microtools". en. In: *International Journal of Nanomanufacturing* 1.3 (2007), p. 439. ISSN: 1746-9392, 1746-9406. DOI: [10.1504/IJNM.2007.013685](https://doi.org/10.1504/IJNM.2007.013685). URL: <http://www.inderscience.com/link.php?id=13685> (visited on 11/22/2022).
- [33] J. M. Taylor et al. "High-sensitivity diamond magnetometer with nanoscale resolution". en. In: *Nature Physics* 4.10 (Oct. 2008), pp. 810–816. ISSN: 1745-2473, 1745-2481. DOI: [10.1038/nphys1075](https://doi.org/10.1038/nphys1075). URL: <http://www.nature.com/articles/nphys1075> (visited on 01/12/2023).
- [34] V. M. Acosta et al. "Diamonds with a high density of nitrogen-vacancy centers for magnetometry applications". en. In: *Physical Review B* 80.11 (Sept. 2009), p. 115202. ISSN: 1098-0121, 1550-235X. DOI: [10.1103/PhysRevB.80.115202](https://doi.org/10.1103/PhysRevB.80.115202). URL: <https://link.aps.org/doi/10.1103/PhysRevB.80.115202> (visited on 01/12/2023).
- [35] John F. Barry et al. "Optical magnetic detection of single-neuron action potentials using quantum defects in diamond". en. In: *Proceedings of the National Academy of Sciences* 113.49 (Dec. 2016), pp. 14133–14138. ISSN: 0027-8424, 1091-6490. DOI: [10.1073/pnas.1601513113](https://doi.org/10.1073/pnas.1601513113). URL: <https://pnas.org/doi/full/10.1073/pnas.1601513113> (visited on 01/12/2023).
- [36] Sébastien Pezzagna and Jan Meijer. "Quantum computer based on color centers in diamond". en. In: *Applied Physics Reviews* 8.1 (Mar. 2021), p. 011308. ISSN: 1931-9401. DOI: [10.1063/5.0007444](https://doi.org/10.1063/5.0007444). URL: <https://aip.scitation.org/doi/10.1063/5.0007444> (visited on 01/12/2023).
- [37] R. M. Chrenko. "Boron, the Dominant Acceptor in Semiconducting Diamond". en. In: *Physical Review B* 7.10 (May 1973), pp. 4560–4567. ISSN: 0556-2805. DOI: [10.1103/PhysRevB.7.4560](https://doi.org/10.1103/PhysRevB.7.4560). URL: <https://link.aps.org/doi/10.1103/PhysRevB.7.4560> (visited on 11/14/2022).
- [38] P.W. May et al. "Raman and conductivity studies of boron-doped microcrystalline diamond, faceted nanocrystalline diamond and cauliflower diamond films". en. In: *Diamond and Related Materials* 17.2 (Feb. 2008), pp. 105–117. ISSN: 09259635. DOI: [10.1016/j.diamond.2007.11.005](https://doi.org/10.1016/j.diamond.2007.11.005). URL: <https://linkinghub.elsevier.com/retrieve/pii/S0925963507004694> (visited on 03/14/2023).
- [39] Gufei Zhang et al. "Metal-Bosonic Insulator-Superconductor Transition in Boron-Doped Granular Diamond". en. In: *Physical Review Letters* 110.7 (Feb. 2013), p. 077001. ISSN: 0031-9007, 1079-7114. DOI: [10.1103/PhysRevLett.110.077001](https://doi.org/10.1103/PhysRevLett.110.077001). URL: <https://link.aps.org/doi/10.1103/PhysRevLett.110.077001> (visited on 11/22/2022).
- [40] Merve Yence et al. "Boron-Doped Diamond Electrodes: Recent Developments and Advances in View of Electrochemical Drug Sensors". en. In: *Critical Reviews in Analytical Chemistry* 52.5 (July 2022), pp. 1122–1138. ISSN: 1040-8347, 1547-6510. DOI: [10.1080/10408347.2020.1863769](https://doi.org/10.1080/10408347.2020.1863769). URL: <https://www.tandfonline.com/doi/full/10.1080/10408347.2020.1863769> (visited on 10/21/2022).
- [41] Shoko Tago et al. "Flexible Boron-Doped Diamond (BDD) Electrodes for Plant Monitoring". en. In: *Sensors* 17.7 (July 2017), p. 1638. ISSN: 1424-8220. DOI: [10.3390/s17071638](https://doi.org/10.3390/s17071638). URL: <http://www.mdpi.com/1424-8220/17/7/1638> (visited on 10/17/2022).
- [42] Muthaiah Shellaiah and Kien Wen Sun. "Diamond-Based Electrodes for Detection of Metal Ions and Anions". en. In: *Nanomaterials* 12.1 (Dec. 2021), p. 64. ISSN: 2079-4991. DOI: [10.3390/nano12010064](https://doi.org/10.3390/nano12010064). URL: <https://www.mdpi.com/2079-4991/12/1/64> (visited on 10/14/2022).
- [43] Yunita Triana, Genki Ogata, and Yasuaki Einaga. "Application of boron doped diamond electrodes to electrochemical gas sensor". en. In: *Current Opinion in Electrochemistry* 36 (Dec. 2022), p. 101113. ISSN: 24519103. DOI: [10.1016/j.coelec.2022.101113](https://doi.org/10.1016/j.coelec.2022.101113). URL: <https://linkinghub.elsevier.com/retrieve/pii/S2451910322001788> (visited on 11/25/2022).
- [44] Peng Wang et al. "A Nanometer-Sized Graphite/Boron-Doped Diamond Electrochemical Sensor for Sensitive Detection of Acetaminophen". In: *ACS Omega* 6.9 (Mar. 2021). Publisher: American Chemical Society, pp. 6326–6334. DOI: [10.1021/acsomega.0c06141](https://doi.org/10.1021/acsomega.0c06141). URL: <https://doi.org/10.1021/acsomega.0c06141> (visited on 11/02/2022).

- [45] Yang Xie et al. "Diamond thin films integrated with flexible substrates and their physical, chemical and biological characteristics". In: *Journal of Physics D: Applied Physics* 54.38 (Sept. 2021), p. 384004. ISSN: 0022-3727, 1361-6463. DOI: [10.1088/1361-6463/ac0de6](https://doi.org/10.1088/1361-6463/ac0de6). URL: <https://iopscience.iop.org/article/10.1088/1361-6463/ac0de6> (visited on 10/17/2022).
- [46] Tomohiro Matsunaga et al. "Sensitive electrochemical detection of L-Cysteine at a screen-printed diamond electrode". en. In: *Carbon* 173 (Mar. 2021), pp. 395–402. ISSN: 00086223. DOI: [10.1016/j.carbon.2020.10.096](https://doi.org/10.1016/j.carbon.2020.10.096). URL: <https://linkinghub.elsevier.com/retrieve/pii/S0008622320310770> (visited on 10/17/2022).
- [47] Ignacio Sanjuán et al. "Boron-doped diamond electrodes explored for the electroanalytical detection of 7-methylguanine and applied for its sensing within urine samples". en. In: *Electrochimica Acta* 197 (Apr. 2016), pp. 167–178. ISSN: 00134686. DOI: [10.1016/j.electacta.2015.11.026](https://doi.org/10.1016/j.electacta.2015.11.026). URL: <https://linkinghub.elsevier.com/retrieve/pii/S0013468615307994> (visited on 10/17/2022).
- [48] Jing Zhang et al. "Preparation of boron-doped diamond foam film for supercapacitor applications". en. In: *Applied Surface Science* 506 (Mar. 2020), p. 144645. ISSN: 01694332. DOI: [10.1016/j.apsusc.2019.144645](https://doi.org/10.1016/j.apsusc.2019.144645). URL: <https://linkinghub.elsevier.com/retrieve/pii/S0169433219334610> (visited on 11/25/2022).
- [49] Clément Trellu et al. "Environmental Applications of Boron-Doped Diamond Electrodes: 2. Soil Remediation and Sensing Applications". en. In: *ChemElectroChem* 6.8 (Apr. 2019), pp. 2143–2156. ISSN: 2196-0216, 2196-0216. DOI: [10.1002/celec.201801877](https://doi.org/10.1002/celec.201801877). URL: <https://onlinelibrary.wiley.com/doi/10.1002/celec.201801877> (visited on 11/25/2022).
- [50] Fengbin Liu et al. "Study on the wastewater disinfection at the boron-doped diamond film electrode". en. In: *Procedia Environmental Sciences* 12 (2012), pp. 116–121. ISSN: 18780296. DOI: [10.1016/j.proenv.2012.01.255](https://doi.org/10.1016/j.proenv.2012.01.255). URL: <https://linkinghub.elsevier.com/retrieve/pii/S1878029612002563> (visited on 11/25/2022).
- [51] R. Bogdanowicz et al. "Determination of Chemical Oxygen Demand (COD) at Boron-doped Diamond (BDD) Sensor by Means of Amperometric Technique". en. In: *Procedia Engineering* 47 (2012), pp. 1117–1120. ISSN: 18777058. DOI: [10.1016/j.proeng.2012.09.347](https://doi.org/10.1016/j.proeng.2012.09.347). URL: <https://linkinghub.elsevier.com/retrieve/pii/S1877705812044104> (visited on 11/28/2022).
- [52] Hongbin Yu et al. "Amperometric determination of chemical oxygen demand using boron-doped diamond (BDD) sensor". en. In: *Electrochemistry Communications* 9.9 (Sept. 2007), pp. 2280–2285. ISSN: 13882481. DOI: [10.1016/j.elecom.2007.06.037](https://doi.org/10.1016/j.elecom.2007.06.037). URL: <https://linkinghub.elsevier.com/retrieve/pii/S138824810700269X> (visited on 11/30/2022).
- [53] Julie V. Macpherson. "A practical guide to using boron doped diamond in electrochemical research". en. In: *Physical Chemistry Chemical Physics* 17.5 (2015), pp. 2935–2949. ISSN: 1463-9076, 1463-9084. DOI: [10.1039/C4CP04022H](https://doi.org/10.1039/C4CP04022H). URL: <http://xlink.rsc.org/?DOI=C4CP04022H> (visited on 11/28/2022).
- [54] M. Iwaki et al. "Electrical conductivity of nitrogen and argon implanted diamond". en. In: *Nuclear Instruments and Methods in Physics Research* 209-210 (May 1983), pp. 1129–1133. ISSN: 01675087. DOI: [10.1016/0167-5087\(83\)90930-4](https://doi.org/10.1016/0167-5087(83)90930-4). URL: <https://linkinghub.elsevier.com/retrieve/pii/0167508783909304> (visited on 11/21/2022).
- [55] K. Nishimura, K. Das, and J. T. Glass. "Material and electrical characterization of polycrystalline boron doped diamond films grown by microwave plasma chemical vapor deposition". In: *Journal of Applied Physics* 69.5 (1991), pp. 3142–3148. DOI: [10.1063/1.348582](https://doi.org/10.1063/1.348582).
- [56] S. Majdi et al. "Single crystal diamond for infrared sensing applications". en. In: *Applied Physics Letters* 105.16 (Oct. 2014), p. 163510. ISSN: 0003-6951, 1077-3118. DOI: [10.1063/1.4899278](https://doi.org/10.1063/1.4899278). URL: <http://aip.scitation.org/doi/10.1063/1.4899278> (visited on 01/17/2023).
- [57] Zhichao Liu et al. "Heavily boron-doped diamond grown on scalable heteroepitaxial quasi-substrates: A promising single crystal material for electrochemical sensing applications". en. In: *Carbon* 201 (Jan. 2023), pp. 1229–1240. ISSN: 00086223. DOI: [10.1016/j.carbon.2022.10.023](https://doi.org/10.1016/j.carbon.2022.10.023). URL: <https://linkinghub.elsevier.com/retrieve/pii/S0008622322008442> (visited on 02/22/2023).
- [58] Tomohiro Matsunaga et al. "Sensitive electrochemical detection of ciprofloxacin at screen-printed diamond electrodes". en. In: *Carbon* 159 (Apr. 2020), pp. 247–254. ISSN: 00086223. DOI: [10.1016/j.carbon.2019.12.051](https://doi.org/10.1016/j.carbon.2019.12.051). URL: <https://linkinghub.elsevier.com/retrieve/pii/S0008622319312862> (visited on 10/17/2022).

- [59] Boron-doped diamond electrodes. URL: <https://www.egr.msu.edu/fraunhofer-usa-cmw/projects/boron-doped-diamond-electrodes>.
- [60] Yasuaki Einaga. "Development of Electrochemical Applications of Boron-Doped Diamond Electrodes". en. In: *Bulletin of the Chemical Society of Japan* 91.12 (Dec. 2018), pp. 1752–1762. ISSN: 0009-2673, 1348-0634. DOI: 10.1246/bcsj.20180268. URL: <http://www.journal.csj.jp/doi/10.1246/bcsj.20180268> (visited on 11/28/2022).
- [61] Yasuaki Einaga. "Introduction". en. In: *Diamond Electrodes*. Ed. by Yasuaki Einaga. Singapore: Springer Singapore, 2022, pp. 1–8. ISBN: 9789811678332 9789811678349. DOI: 10.1007/978-981-16-7834-9_1. URL: https://link.springer.com/10.1007/978-981-16-7834-9_1 (visited on 11/28/2022).
- [62] Takeshi Kondo et al. "Screen-printed diamond electrode: A disposable sensitive electrochemical electrode". en. In: *Electrochemistry Communications* 13.12 (Dec. 2011), pp. 1546–1549. ISSN: 13882481. DOI: 10.1016/j.elecom.2011.10.013. URL: <https://linkinghub.elsevier.com/retrieve/pii/S1388248111004280> (visited on 01/27/2023).
- [63] Peng Chang et al. "3D printed electrochemical energy storage devices". en. In: *Journal of Materials Chemistry A* 7.9 (2019), pp. 4230–4258. ISSN: 2050-7488, 2050-7496. DOI: 10.1039/C8TA11860D. URL: <http://xlink.rsc.org/?DOI=C8TA11860D> (visited on 10/14/2022).
- [64] Bin Fan et al. "Flexible, diamond-based microelectrodes fabricated using the diamond growth side for neural sensing". en. In: *Microsystems & Nanoengineering* 6.1 (July 2020), p. 42. ISSN: 2055-7434. DOI: 10.1038/s41378-020-0155-1. URL: <https://www.nature.com/articles/s41378-020-0155-1> (visited on 01/19/2023).
- [65] Clément Hébert et al. "Monitoring the evolution of boron doped porous diamond electrode on flexible retinal implant by OCT and in vivo impedance spectroscopy". en. In: *Materials Science and Engineering: C* 69 (Dec. 2016), pp. 77–84. ISSN: 09284931. DOI: 10.1016/j.msec.2016.06.032. URL: <https://linkinghub.elsevier.com/retrieve/pii/S0928493116306014> (visited on 01/19/2023).
- [66] M. Rycewicz et al. "Low-strain sensor based on the flexible boron-doped diamond-polymer structures". en. In: *Carbon* 173 (Mar. 2021), pp. 832–841. ISSN: 00086223. DOI: 10.1016/j.carbon.2020.11.071. URL: <https://linkinghub.elsevier.com/retrieve/pii/S0008622320311507> (visited on 01/19/2023).
- [67] Tiankuo Chu, Soyeon Park, and Kun (Kelvin) Fu. "3D printing-enabled advanced electrode architecture design". en. In: *Carbon Energy* 3.3 (July 2021), pp. 424–439. ISSN: 2637-9368, 2637-9368. DOI: 10.1002/cey2.114. URL: <https://onlinelibrary.wiley.com/doi/10.1002/cey2.114> (visited on 01/23/2023).
- [68] Ian Gibson et al. *Additive manufacturing technologies*. eng. Third edition. Cham, Switzerland: Springer, 2021. ISBN: 978-3-030-56126-0 978-3-030-56129-1.
- [69] Adriano Ambrosi and Martin Pumera. "3D-printing technologies for electrochemical applications". en. In: *Chemical Society Reviews* 45.10 (2016), pp. 2740–2755. ISSN: 0306-0012, 1460-4744. DOI: 10.1039/C5CS00714C. URL: <http://xlink.rsc.org/?DOI=C5CS00714C> (visited on 10/14/2022).
- [70] Dave Marmik and Shiraj Sunasara. "Advanced Manufacturing Technique: 3D Printing". In: 2 (Mar. 2015), pp. 2393–9877.
- [71] Xufei Lu et al. "3D printing well organized porous iron-nickel/polyaniline nanocages multiscale supercapacitor". en. In: *Journal of Alloys and Compounds* 760 (Sept. 2018), pp. 78–83. ISSN: 09258388. DOI: 10.1016/j.jallcom.2018.05.165. URL: <https://linkinghub.elsevier.com/retrieve/pii/S0925838818318760> (visited on 12/08/2022).
- [72] Adriano Ambrosi, James Guo Sheng Moo, and Martin Pumera. "Helical 3D-Printed Metal Electrodes as Custom-Shaped 3D Platform for Electrochemical Devices". en. In: *Advanced Functional Materials* 26.5 (Feb. 2016), pp. 698–703. ISSN: 1616301X. DOI: 10.1002/adfm.201503902. URL: <https://onlinelibrary.wiley.com/doi/10.1002/adfm.201503902> (visited on 12/08/2022).
- [73] Changyong Liu et al. "3D printing technologies for flexible tactile sensors toward wearable electronics and electronic skin". In: *Polymers* 10.6 (2018), p. 629. DOI: 10.3390/polym10060629.
- [74] Jie Zhang et al. "Resistivity and Its Anisotropy Characterization of 3D-Printed Acrylonitrile Butadiene Styrene Copolymer (ABS)/Carbon Black (CB) Composites". en. In: *Applied Sciences* 7.1 (Jan. 2017), p. 20. ISSN: 2076-3417. DOI: 10.3390/app7010020. URL: <http://www.mdpi.com/2076-3417/7/1/20> (visited on 10/27/2022).

- [75] Steven Shaffer et al. "On reducing anisotropy in 3D printed polymers via ionizing radiation". en. In: *Polymer* 55.23 (Nov. 2014), pp. 5969–5979. ISSN: 00323861. DOI: 10.1016/j.polymer.2014.07.054. URL: <https://linkinghub.elsevier.com/retrieve/pii/S0032386114006636> (visited on 12/21/2022).
- [76] Angel R. Torrado et al. "Characterizing the effect of additives to ABS on the mechanical property anisotropy of specimens fabricated by material extrusion 3D printing". en. In: *Additive Manufacturing* 6 (Apr. 2015), pp. 16–29. ISSN: 22148604. DOI: 10.1016/j.addma.2015.02.001. URL: <https://linkinghub.elsevier.com/retrieve/pii/S2214860415000111> (visited on 12/21/2022).
- [77] *Electrifi conductive filament*. Feb. 2022. URL: <https://www.multi3d11c.com/product/electrifi/>.
- [78] *Eel 3D printer filament (90a)*. Apr. 2021. URL: <https://ninjatek.com/shop/eel/>.
- [79] *Electrically conductive composite PLA*. URL: <https://www.proto-pasta.com/products/conductive-pla>.
- [80] *Recreus filaflex conductivo*. URL: <https://recreus.com/gb/filaments/3-21-filaflex-conductivo.html>.
- [81] Dejana Pejak Simunec and Antonella Sola. "Emerging Research in Conductive Materials for Fused Filament Fabrication: A Critical Review". en. In: *Advanced Engineering Materials* 24.7 (July 2022), p. 2101476. ISSN: 1438-1656, 1527-2648. DOI: 10.1002/adem.202101476. URL: <https://onlinelibrary.wiley.com/doi/10.1002/adem.202101476> (visited on 11/07/2022).
- [82] Tobias Beran et al. "Nozzle clogging factors during fused filament fabrication of spherical particle filled polymers". en. In: *Additive Manufacturing* 23 (Oct. 2018), pp. 206–214. ISSN: 22148604. DOI: 10.1016/j.addma.2018.08.009. URL: <https://linkinghub.elsevier.com/retrieve/pii/S2214860418303609> (visited on 12/22/2022).
- [83] Asma Almazrouei et al. "Robust Surface-Engineered Tape-Cast and Extrusion Methods to Fabricate Electrically-Conductive Poly(vinylidene fluoride)/Carbon Nanotube Filaments for Corrosion-Resistant 3D Printing Applications". en. In: *Scientific Reports* 9.1 (Dec. 2019), p. 9618. ISSN: 2045-2322. DOI: 10.1038/s41598-019-45992-5. URL: <http://www.nature.com/articles/s41598-019-45992-5> (visited on 11/07/2022).
- [84] Hongyi Yao, Jieqiong Wang, and Shengli Mi. "Photo Processing for Biomedical Hydrogels Design and Functionality: A Review". en. In: *Polymers* 10.1 (Dec. 2017), p. 11. ISSN: 2073-4360. DOI: 10.3390/polym10010011. URL: <http://www.mdpi.com/2073-4360/10/1/11> (visited on 12/16/2022).
- [85] H. Wu et al. "Recent developments in polymers/polymer nanocomposites for additive manufacturing". en. In: *Progress in Materials Science* 111 (June 2020), p. 100638. ISSN: 00796425. DOI: 10.1016/j.pmatsci.2020.100638. URL: <https://linkinghub.elsevier.com/retrieve/pii/S0079642520300025> (visited on 11/02/2022).
- [86] Zishen Wang et al. "Three-Dimensional Printing of Polyaniline/Reduced Graphene Oxide Composite for High-Performance Planar Supercapacitor". en. In: *ACS Applied Materials & Interfaces* 10.12 (Mar. 2018), pp. 10437–10444. ISSN: 1944-8244, 1944-8252. DOI: 10.1021/acsami.7b19635. URL: <https://pubs.acs.org/doi/10.1021/acsami.7b19635> (visited on 12/15/2022).
- [87] Adam E. Jakus et al. "Three-Dimensional Printing of High-Content Graphene Scaffolds for Electronic and Biomedical Applications". en. In: *ACS Nano* 9.4 (Apr. 2015), pp. 4636–4648. ISSN: 1936-0851, 1936-086X. DOI: 10.1021/acs.nano.5b01179. URL: <https://pubs.acs.org/doi/10.1021/acs.nano.5b01179> (visited on 12/15/2022).
- [88] A. Dorigato et al. "Electrically conductive nanocomposites for fused deposition modelling". en. In: *Synthetic Metals* 226 (Apr. 2017), pp. 7–14. ISSN: 03796779. DOI: 10.1016/j.synthmet.2017.01.009. URL: <https://linkinghub.elsevier.com/retrieve/pii/S0379677917300097> (visited on 11/01/2022).
- [89] Z. C. Kennedy et al. "3D-printed poly(vinylidene fluoride)/carbon nanotube composites as a tunable, low-cost chemical vapour sensing platform". en. In: *Nanoscale* 9.17 (2017), pp. 5458–5466. ISSN: 2040-3364, 2040-3372. DOI: 10.1039/C7NR00617A. URL: <http://xlink.rsc.org/?DOI=C7NR00617A> (visited on 10/27/2022).
- [90] Josef F. Christ et al. "3D printed highly elastic strain sensors of multiwalled carbon nanotube/thermoplastic polyurethane nanocomposites". en. In: *Materials & Design* 131 (Oct. 2017), pp. 394–401. ISSN: 02641275. DOI: 10.1016/j.matdes.2017.06.011. URL: <https://linkinghub.elsevier.com/retrieve/pii/S0264127517305944> (visited on 11/03/2022).

- [91] Lazaros Tzounis et al. "3D Printed Thermoelectric Polyurethane/Multiwalled Carbon Nanotube Nanocomposites: A Novel Approach towards the Fabrication of Flexible and Stretchable Organic Thermoelectrics". en. In: *Materials* 13.12 (June 2020), p. 2879. ISSN: 1996-1944. DOI: [10.3390/ma13122879](https://doi.org/10.3390/ma13122879). URL: <https://www.mdpi.com/1996-1944/13/12/2879> (visited on 11/02/2022).
- [92] Cameron J. Hohimer et al. "3D printed conductive thermoplastic polyurethane/carbon nanotube composites for capacitive and piezoresistive sensing in soft pneumatic actuators". en. In: *Additive Manufacturing* 34 (Aug. 2020), p. 101281. ISSN: 22148604. DOI: [10.1016/j.addma.2020.101281](https://doi.org/10.1016/j.addma.2020.101281). URL: <https://linkinghub.elsevier.com/retrieve/pii/S2214860420306539> (visited on 11/07/2022).
- [93] Bartłomiej Podsiadły et al. "Carbon Nanotube-Based Composite Filaments for 3D Printing of Structural and Conductive Elements". en. In: *Applied Sciences* 11.3 (Jan. 2021), p. 1272. ISSN: 2076-3417. DOI: [10.3390/app11031272](https://doi.org/10.3390/app11031272). URL: <https://www.mdpi.com/2076-3417/11/3/1272> (visited on 11/02/2022).
- [94] Sithiprumnea Dul, Luca Fambri, and Alessandro Pegoretti. "Filaments Production and Fused Deposition Modelling of ABS/Carbon Nanotubes Composites". en. In: *Nanomaterials* 8.1 (Jan. 2018), p. 49. ISSN: 2079-4991. DOI: [10.3390/nano8010049](https://doi.org/10.3390/nano8010049). URL: <https://www.mdpi.com/2079-4991/8/1/49> (visited on 10/25/2022).
- [95] K. Gnanasekaran et al. "3D printing of CNT- and graphene-based conductive polymer nanocomposites by fused deposition modeling". en. In: *Applied Materials Today* 9 (Dec. 2017), pp. 21–28. ISSN: 23529407. DOI: [10.1016/j.apmt.2017.04.003](https://doi.org/10.1016/j.apmt.2017.04.003). URL: <https://linkinghub.elsevier.com/retrieve/pii/S2352940717300586> (visited on 11/02/2022).
- [96] Xin Ye et al. "Effect of annealing and carbon nanotube infill on the mechanical and electrical properties of additively manufactured polyether-ether-ketone nanocomposites via fused filament fabrication". en. In: *Additive Manufacturing* 59 (Nov. 2022), p. 103188. ISSN: 22148604. DOI: [10.1016/j.addma.2022.103188](https://doi.org/10.1016/j.addma.2022.103188). URL: <https://linkinghub.elsevier.com/retrieve/pii/S2214860422005772> (visited on 11/08/2022).
- [97] Wang Wang Yu et al. "Incorporation of graphitic nano-filler and poly(lactic acid) in fused deposition modeling". en. In: *Journal of Applied Polymer Science* 134.15 (Apr. 2017). ISSN: 00218995. DOI: [10.1002/app.44703](https://doi.org/10.1002/app.44703). URL: <https://onlinelibrary.wiley.com/doi/10.1002/app.44703> (visited on 10/17/2022).
- [98] Xiaojun Wei et al. "3D Printable Graphene Composite". en. In: *Scientific Reports* 5.1 (Sept. 2015), p. 11181. ISSN: 2045-2322. DOI: [10.1038/srep11181](https://doi.org/10.1038/srep11181). URL: <http://www.nature.com/articles/srep11181> (visited on 10/17/2022).
- [99] Di Zhang et al. "Fabrication of highly conductive graphene flexible circuits by 3D printing". en. In: *Synthetic Metals* 217 (July 2016), pp. 79–86. ISSN: 03796779. DOI: [10.1016/j.synthmet.2016.03.014](https://doi.org/10.1016/j.synthmet.2016.03.014). URL: <https://linkinghub.elsevier.com/retrieve/pii/S0379677916300649> (visited on 10/24/2022).
- [100] Simon J. Leigh et al. "A Simple, Low-Cost Conductive Composite Material for 3D Printing of Electronic Sensors". en. In: *PLoS ONE* 7.11 (Nov. 2012). Ed. by Jeongmin Hong, e49365. ISSN: 1932-6203. DOI: [10.1371/journal.pone.0049365](https://doi.org/10.1371/journal.pone.0049365). URL: <https://dx.plos.org/10.1371/journal.pone.0049365> (visited on 10/20/2022).
- [101] Feng Zhang et al. "3D printing technologies for electrochemical energy storage". en. In: *Nano Energy* 40 (Oct. 2017), pp. 418–431. ISSN: 22112855. DOI: [10.1016/j.nanoen.2017.08.037](https://doi.org/10.1016/j.nanoen.2017.08.037). URL: <https://linkinghub.elsevier.com/retrieve/pii/S221128551730513X> (visited on 10/18/2022).
- [102] Sen Wai Kwok et al. "Electrically conductive filament for 3D-printed circuits and sensors". en. In: *Applied Materials Today* 9 (Dec. 2017), pp. 167–175. ISSN: 23529407. DOI: [10.1016/j.apmt.2017.07.001](https://doi.org/10.1016/j.apmt.2017.07.001). URL: <https://linkinghub.elsevier.com/retrieve/pii/S235294071730152X> (visited on 10/25/2022).
- [103] Namsoo Peter Kim. "3D-Printed Conductive Carbon-Infused Thermoplastic Polyurethane". en. In: *Polymers* 12.6 (May 2020), p. 1224. ISSN: 2073-4360. DOI: [10.3390/polym12061224](https://doi.org/10.3390/polym12061224). URL: <https://www.mdpi.com/2073-4360/12/6/1224> (visited on 11/02/2022).
- [104] Hadil M. Elbardisy et al. "Versatile additively manufactured (3D printed) wall-jet flow cell for high performance liquid chromatography-amperometric analysis: application to the detection and quantification of new psychoactive substances (NBOMes)". en. In: *Analytical Methods* 12.16 (2020), pp. 2152–2165. ISSN: 1759-9660, 1759-9679. DOI: [10.1039/D0AY00500B](https://doi.org/10.1039/D0AY00500B). URL: <http://xlink.rsc.org/?DOI=D0AY00500B> (visited on 10/20/2022).

- [105] Christopher W. Foster et al. "Additively manufactured graphitic electrochemical sensing platforms". en. In: *Chemical Engineering Journal* 381 (Feb. 2020), p. 122343. ISSN: 13858947. DOI: 10.1016/j.cej.2019.122343. URL: <https://linkinghub.elsevier.com/retrieve/pii/S1385894719317462> (visited on 10/17/2022).
- [106] Shrenik Kumar Jain and Yonas Tadesse. "Fabrication of Polylactide/Carbon Nanopowder Filament using Melt Extrusion and Filament Characterization for 3D Printing". en. In: *International Journal of Nanoscience* 18.05 (Oct. 2019), p. 1850026. ISSN: 0219-581X, 1793-5350. DOI: 10.1142/S0219581X18500266. URL: <https://www.worldscientific.com/doi/abs/10.1142/S0219581X18500266> (visited on 10/17/2022).
- [107] Zuhayr Rymansaib et al. "All-Polystyrene 3D-Printed Electrochemical Device with Embedded Carbon Nanofiber-Graphite-Polystyrene Composite Conductor". en. In: *Electroanalysis* 28.7 (July 2016), pp. 1517–1523. ISSN: 10400397. DOI: 10.1002/elan.201600017. URL: <https://onlinelibrary.wiley.com/doi/10.1002/elan.201600017> (visited on 10/20/2022).
- [108] Dingchun Zhu et al. "Thermal and mechanical properties of polyamide 12/graphene nanoplatelets nanocomposites and parts fabricated by fused deposition modeling: ARTICLE". en. In: *Journal of Applied Polymer Science* 134.39 (Oct. 2017), p. 45332. ISSN: 00218995. DOI: 10.1002/app.45332. URL: <https://onlinelibrary.wiley.com/doi/10.1002/app.45332> (visited on 11/03/2022).
- [109] Nour-Alhoda Masarra et al. "Fabrication of PLA/PCL/Graphene Nanoplatelet (GNP) Electrically Conductive Circuit Using the Fused Filament Fabrication (FFF) 3D Printing Technique". en. In: *Materials* 15.3 (Jan. 2022), p. 762. ISSN: 1996-1944. DOI: 10.3390/ma15030762. URL: <https://www.mdpi.com/1996-1944/15/3/762> (visited on 11/07/2022).
- [110] Akshay Potnuru and Yonas Tadesse. "Investigation of polylactide and carbon nanocomposite filament for 3D printing". en. In: *Progress in Additive Manufacturing* 4.1 (Mar. 2019), pp. 23–41. ISSN: 2363-9512, 2363-9520. DOI: 10.1007/s40964-018-0057-z. URL: <http://link.springer.com/10.1007/s40964-018-0057-z> (visited on 12/23/2022).
- [111] Yuqing Gao et al. "Influence of filler size on the properties of poly(lactic acid) (PLA)/graphene nanoplatelet (GNP) nanocomposites". en. In: *European Polymer Journal* 86 (Jan. 2017), pp. 117–131. ISSN: 00143057. DOI: 10.1016/j.eurpolymj.2016.10.045. URL: <https://linkinghub.elsevier.com/retrieve/pii/S0014305716309387> (visited on 01/06/2023).
- [112] Alexis Maurel et al. "Highly Loaded Graphite-Polylactic Acid Composite-Based Filaments for Lithium-Ion Battery Three-Dimensional Printing". en. In: *Chemistry of Materials* 30.21 (Nov. 2018), pp. 7484–7493. ISSN: 0897-4756, 1520-5002. DOI: 10.1021/acs.chemmater.8b02062. URL: <https://pubs.acs.org/doi/10.1021/acs.chemmater.8b02062> (visited on 10/18/2022).
- [113] Jill Z. Manapat et al. "High-Strength Stereolithographic 3D Printed Nanocomposites: Graphene Oxide Metastability". en. In: *ACS Applied Materials & Interfaces* 9.11 (Mar. 2017), pp. 10085–10093. ISSN: 1944-8244, 1944-8252. DOI: 10.1021/acsami.6b16174. URL: <https://pubs.acs.org/doi/10.1021/acsami.6b16174> (visited on 12/19/2022).
- [114] Dong Lin et al. "3D stereolithography printing of graphene oxide reinforced complex architectures". In: *Nanotechnology* 26.43 (Oct. 2015), p. 434003. ISSN: 0957-4484, 1361-6528. DOI: 10.1088/0957-4484/26/43/434003. URL: <https://iopscience.iop.org/article/10.1088/0957-4484/26/43/434003> (visited on 12/19/2022).
- [115] Ran Xiao et al. "Stereolithography (SLA) 3D printing of carbon fiber-graphene oxide (CF-GO) reinforced polymer lattices". In: *Nanotechnology* 32.23 (June 2021), p. 235702. ISSN: 0957-4484, 1361-6528. DOI: 10.1088/1361-6528/abe825. URL: <https://iopscience.iop.org/article/10.1088/1361-6528/abe825> (visited on 11/29/2022).
- [116] Gustavo Gonzalez et al. "Development of 3D printable formulations containing CNT with enhanced electrical properties". en. In: *Polymer* 109 (Jan. 2017), pp. 246–253. ISSN: 00323861. DOI: 10.1016/j.polymer.2016.12.051. URL: <https://linkinghub.elsevier.com/retrieve/pii/S0032386116311429> (visited on 12/16/2022).
- [117] Quanyi Mu et al. "Digital light processing 3D printing of conductive complex structures". en. In: *Additive Manufacturing* 18 (Dec. 2017), pp. 74–83. ISSN: 22148604. DOI: 10.1016/j.addma.2017.08.011. URL: <https://linkinghub.elsevier.com/retrieve/pii/S2214860417300398> (visited on 12/19/2022).

- [118] Umme Kalsoom, Sidra Waheed, and Brett Paull. "Fabrication of Humidity Sensor Using 3D Printable Polymer Composite Containing Boron-Doped Diamonds and LiCl". en. In: *ACS Applied Materials & Interfaces* 12.4 (Jan. 2020), pp. 4962–4969. issn: 1944-8244, 1944-8252. doi: [10.1021/acsami.9b22519](https://doi.org/10.1021/acsami.9b22519). (Visited on 10/14/2022).
- [119] Sidra Waheed et al. "Three-Dimensional Printing of Abrasive, Hard, and Thermally Conductive Synthetic Microdiamond-Polymer Composite Using Low-Cost Fused Deposition Modeling Printer". en. In: *ACS Applied Materials & Interfaces* 11.4 (Jan. 2019), pp. 4353–4363. issn: 1944-8244, 1944-8252. doi: [10.1021/acsami.8b18232](https://doi.org/10.1021/acsami.8b18232). URL: <https://pubs.acs.org/doi/10.1021/acsami.8b18232> (visited on 10/24/2022).
- [120] U. Kalsoom et al. "A 3D printable diamond polymer composite: a novel material for fabrication of low cost thermally conducting devices". en. In: *RSC Advances* 6.44 (2016), pp. 38140–38147. issn: 2046-2069. doi: [10.1039/C6RA05261D](https://doi.org/10.1039/C6RA05261D). URL: <http://xlink.rsc.org/?DOI=C6RA05261D> (visited on 10/18/2022).
- [121] Catharina Kahrs and Jan Schwellenbach. "Membrane formation via non-solvent induced phase separation using sustainable solvents: A comparative study". en. In: *Polymer* 186 (Jan. 2020), p. 122071. issn: 00323861. doi: [10.1016/j.polymer.2019.122071](https://doi.org/10.1016/j.polymer.2019.122071). URL: <https://linkinghub.elsevier.com/retrieve/pii/S0032386119310778> (visited on 10/02/2023).
- [122] Steven Praver and Robert J. Nemanich. "Raman spectroscopy of diamond and doped diamond". en. In: *Philosophical Transactions of the Royal Society of London. Series A: Mathematical, Physical and Engineering Sciences* 362.1824 (Nov. 2004), pp. 2537–2565. issn: 1364-503X, 1471-2962. doi: [10.1098/rsta.2004.1451](https://doi.org/10.1098/rsta.2004.1451). URL: <https://royalsocietypublishing.org/doi/10.1098/rsta.2004.1451> (visited on 03/14/2023).
- [123] Carlos F. Ruiz-Valdez et al. "Raman and Thermoluminescence Studies of HPHT Synthetic Nanodiamond Powders". en. In: *physica status solidi (a)* 215.22 (Nov. 2018), p. 1800267. issn: 18626300. doi: [10.1002/pssa.201800267](https://doi.org/10.1002/pssa.201800267). URL: <https://onlinelibrary.wiley.com/doi/10.1002/pssa.201800267> (visited on 03/28/2023).
- [124] Koichi Ushizawa et al. "Boron concentration dependence of Raman spectra on {100} and {111} facets of B-doped CVD diamond". en. In: *Diamond and Related Materials* 7.11-12 (Dec. 1998), pp. 1719–1722. issn: 09259635. doi: [10.1016/S0925-9635\(98\)00296-9](https://doi.org/10.1016/S0925-9635(98)00296-9). URL: <https://linkinghub.elsevier.com/retrieve/pii/S0925963598002969> (visited on 08/04/2023).
- [125] V. Mortet et al. "Analysis of heavily boron-doped diamond Raman spectrum". en. In: *Diamond and Related Materials* 88 (Sept. 2018), pp. 163–166. issn: 09259635. doi: [10.1016/j.diamond.2018.07.013](https://doi.org/10.1016/j.diamond.2018.07.013). URL: <https://linkinghub.elsevier.com/retrieve/pii/S0925963518303467> (visited on 10/02/2023).
- [126] Xing-Zhong Zhao et al. "Downshift of Raman peak in diamond powders". en. In: *Journal of Materials Research* 13.7 (July 1998), pp. 1974–1976. issn: 0884-2914, 2044-5326. doi: [10.1557/JMR.1998.0277](https://doi.org/10.1557/JMR.1998.0277). URL: <http://link.springer.com/10.1557/JMR.1998.0277> (visited on 03/28/2023).
- [127] Yuewei Li et al. "Vat polymerization-based 3D printing of nanocomposites: A mini review". In: *Frontiers in Materials* 9 (Jan. 2023), p. 1118943. issn: 2296-8016. doi: [10.3389/fmats.2022.1118943](https://doi.org/10.3389/fmats.2022.1118943). URL: <https://www.frontiersin.org/articles/10.3389/fmats.2022.1118943/full> (visited on 08/16/2023).
- [128] Yuanyuan Zhang et al. "Additive manufacturing of carbon nanotube-photopolymer composite radar absorbing materials". en. In: *Polymer Composites* 39.S2 (May 2018), E671–E676. issn: 02728397. doi: [10.1002/pc.24117](https://doi.org/10.1002/pc.24117). URL: <https://onlinelibrary.wiley.com/doi/10.1002/pc.24117> (visited on 12/16/2022).
- [129] Hengky Eng et al. "Development of CNTs-filled photopolymer for projection stereolithography". en. In: *Rapid Prototyping Journal* 23.1 (Jan. 2017), pp. 129–136. issn: 1355-2546. doi: [10.1108/RPJ-10-2015-0148](https://doi.org/10.1108/RPJ-10-2015-0148). URL: <https://www.emerald.com/insight/content/doi/10.1108/RPJ-10-2015-0148/full/html> (visited on 09/24/2023).
- [130] Mahmoud M Shokrieh, Ali Saeedi, and Majid Chitsazzadeh. "Mechanical properties of multi-walled carbon nanotube/polyester nanocomposites". en. In: *Journal of Nanostructure in Chemistry* 3.1 (Dec. 2013), p. 20. issn: 2008-9244, 2193-8865. doi: [10.1186/2193-8865-3-20](https://doi.org/10.1186/2193-8865-3-20). URL: <http://link.springer.com/10.1186/2193-8865-3-20> (visited on 09/24/2023).
- [131] Anna Zubrowska et al. "Structure, thermal and mechanical properties of polypropylene composites with nano- and micro-diamonds". In: *Polimery* 60.05 (May 2015), pp. 331–336. issn: 00322725. doi: [10.14314/polimery.2015.331](https://doi.org/10.14314/polimery.2015.331). URL: <http://polimery.ichp.vot.pl/index.php/p/article/view/534> (visited on 11/29/2022).

- [132] Qingwei Zhang et al. "Mechanical properties and biomineralization of multifunctional nanodiamond-PLLA composites for bone tissue engineering". en. In: *Biomaterials* 33.20 (July 2012), pp. 5067–5075. ISSN: 01429612. DOI: [10.1016/j.biomaterials.2012.03.063](https://doi.org/10.1016/j.biomaterials.2012.03.063). URL: <https://linkinghub.elsevier.com/retrieve/pii/S0142961212003626> (visited on 09/22/2023).
- [133] Kristopher D. Behler et al. "Nanodiamond-Polymer Composite Fibers and Coatings". en. In: *ACS Nano* 3.2 (Feb. 2009), pp. 363–369. ISSN: 1936-0851, 1936-086X. DOI: [10.1021/nn800445z](https://doi.org/10.1021/nn800445z). URL: <https://pubs.acs.org/doi/10.1021/nn800445z> (visited on 09/22/2023).
- [134] Wenjie Liu et al. "Fabrication of PLA Filaments and its Printable Performance". In: *IOP Conference Series: Materials Science and Engineering* 275 (Dec. 2017), p. 012033. ISSN: 1757-8981, 1757-899X. DOI: [10.1088/1757-899X/275/1/012033](https://doi.org/10.1088/1757-899X/275/1/012033). URL: <https://iopscience.iop.org/article/10.1088/1757-899X/275/1/012033> (visited on 09/24/2023).
- [135] Mateusz Cieřlik et al. "Multiple Reprocessing of Conductive PLA 3D-Printing Filament: Rheology, Morphology, Thermal and Electrochemical Properties Assessment". en. In: *Materials* 16.3 (Feb. 2023), p. 1307. ISSN: 1996-1944. DOI: [10.3390/ma16031307](https://doi.org/10.3390/ma16031307). URL: <https://www.mdpi.com/1996-1944/16/3/1307> (visited on 09/24/2023).
- [136] Yan Zhang et al. "Morphological structure and mechanical properties of epoxy/polysulfone/cellulose nanofiber ternary nanocomposites". en. In: *Composites Science and Technology* 115 (Aug. 2015), pp. 66–71. ISSN: 02663538. DOI: [10.1016/j.compscitech.2015.05.003](https://doi.org/10.1016/j.compscitech.2015.05.003). URL: <https://linkinghub.elsevier.com/retrieve/pii/S0266353815001906> (visited on 09/26/2023).
- [137] Jingyu Wu et al. "Effect of the Addition of Thermoplastic Resin and Composite on Mechanical and Thermal Properties of Epoxy Resin". en. In: *Polymers* 14.6 (Mar. 2022), p. 1087. ISSN: 2073-4360. DOI: [10.3390/polym14061087](https://doi.org/10.3390/polym14061087). URL: <https://www.mdpi.com/2073-4360/14/6/1087> (visited on 09/26/2023).
- [138] Fenghua Su and Menghe Miao. "Effect of MWCNT dimension on the electrical percolation and mechanical properties of poly(vinylidene fluoride-hexafluoropropylene) based nanocomposites". en. In: *Synthetic Metals* 191 (May 2014), pp. 99–103. ISSN: 03796779. DOI: [10.1016/j.synthmet.2014.02.023](https://doi.org/10.1016/j.synthmet.2014.02.023). URL: <https://linkinghub.elsevier.com/retrieve/pii/S0379677914000782> (visited on 09/27/2023).
- [139] Lucas G. Pedroni et al. "Conductivity and mechanical properties of composites based on MWCNTs and styrene-butadiene-styrene blockTM copolymers". en. In: *Journal of Applied Polymer Science* 112.6 (June 2009), pp. 3241–3248. ISSN: 00218995, 10974628. DOI: [10.1002/app.29897](https://doi.org/10.1002/app.29897). URL: <https://onlinelibrary.wiley.com/doi/10.1002/app.29897> (visited on 09/27/2023).
- [140] S. Gong, Z. H. Zhu, and Z. Li. "Electron tunnelling and hopping effects on the temperature coefficient of resistance of carbon nanotube/polymer nanocomposites". en. In: *Physical Chemistry Chemical Physics* 19.7 (2017), pp. 5113–5120. ISSN: 1463-9076, 1463-9084. DOI: [10.1039/C6CP08115K](https://doi.org/10.1039/C6CP08115K). URL: <http://xlink.rsc.org/?DOI=C6CP08115K> (visited on 09/27/2023).
- [141] Razieh Razavi, Yasser Zare, and Kyong Yop Rhee. "The roles of interphase and filler dimensions in the properties of tunneling spaces between CNT in polymer nanocomposites". en. In: *Polymer Composites* 40.2 (Feb. 2019), pp. 801–810. ISSN: 0272-8397, 1548-0569. DOI: [10.1002/pc.24739](https://doi.org/10.1002/pc.24739). URL: <https://4spepublications.onlinelibrary.wiley.com/doi/10.1002/pc.24739> (visited on 09/27/2023).
- [142] Ning Hu et al. "Tunneling effect in a polymer/carbon nanotube nanocomposite strain sensor". en. In: *Acta Materialia* 56.13 (Aug. 2008), pp. 2929–2936. ISSN: 13596454. DOI: [10.1016/j.actamat.2008.02.030](https://doi.org/10.1016/j.actamat.2008.02.030). URL: <https://linkinghub.elsevier.com/retrieve/pii/S1359645408001602> (visited on 09/27/2023).
- [143] Kyuyoung Kim et al. "3D printing of multi-axial force sensors using carbon nanotube (CNT)/thermoplastic polyurethane (TPU) filaments". en. In: *Sensors and Actuators A: Physical* 263 (Aug. 2017), pp. 493–500. ISSN: 09244247. DOI: [10.1016/j.sna.2017.07.020](https://doi.org/10.1016/j.sna.2017.07.020). URL: <https://linkinghub.elsevier.com/retrieve/pii/S0924424717306027> (visited on 11/03/2022).
- [144] Qiyi Chen et al. "3D Printing Biocompatible Polyurethane/Poly(lactic acid)/Graphene Oxide Nanocomposites: Anisotropic Properties". en. In: *ACS Applied Materials & Interfaces* 9.4 (Feb. 2017), pp. 4015–4023. ISSN: 1944-8244, 1944-8252. DOI: [10.1021/acsami.6b11793](https://doi.org/10.1021/acsami.6b11793). URL: <https://pubs.acs.org/doi/10.1021/acsami.6b11793> (visited on 11/07/2022).

- [145] Rafael M. Cardoso et al. "3D-Printed graphene/polylactic acid electrode for bioanalysis: Biosensing of glucose and simultaneous determination of uric acid and nitrite in biological fluids". en. In: *Sensors and Actuators B: Chemical* 307 (Mar. 2020), p. 127621. ISSN: 09254005. DOI: 10.1016/j.snb.2019.127621. URL: <https://linkinghub.elsevier.com/retrieve/pii/S0925400519318209> (visited on 09/10/2023).
- [146] Rui Gusmão et al. "The capacitance and electron transfer of 3D-printed graphene electrodes are dramatically influenced by the type of solvent used for pre-treatment". en. In: *Electrochemistry Communications* 102 (May 2019), pp. 83–88. ISSN: 13882481. DOI: 10.1016/j.elecom.2019.04.004. URL: <https://linkinghub.elsevier.com/retrieve/pii/S1388248119300852> (visited on 09/10/2023).
- [147] C. Lorena Manzanares Palenzuela et al. "3D-Printed Graphene/Poly(lactic Acid) Electrodes Promise High Sensitivity in Electroanalysis". en. In: *Analytical Chemistry* 90.9 (May 2018), pp. 5753–5757. ISSN: 0003-2700, 1520-6882. DOI: 10.1021/acs.analchem.8b00083. URL: <https://pubs.acs.org/doi/10.1021/acs.analchem.8b00083> (visited on 09/10/2023).
- [148] Vinicius A.O.P. Silva et al. "3D-printed reduced graphene oxide/polylactic acid electrodes: A new prototyped platform for sensing and biosensing applications". en. In: *Biosensors and Bioelectronics* 170 (Dec. 2020), p. 112684. ISSN: 09565663. DOI: 10.1016/j.bios.2020.112684. URL: <https://linkinghub.elsevier.com/retrieve/pii/S0956566320306734> (visited on 10/20/2022).
- [149] Carmen Lorena Manzanares-Palenzuela et al. "Proteinase-sculptured 3D-printed graphene/polylactic acid electrodes as potential biosensing platforms: towards enzymatic modeling of 3D-printed structures". en. In: *Nanoscale* 11.25 (2019), pp. 12124–12131. ISSN: 2040-3364, 2040-3372. DOI: 10.1039/C9NR02754H. URL: <http://xlink.rsc.org/?DOI=C9NR02754H> (visited on 10/02/2023).
- [150] Mateusz Cieřlik et al. "Tailoring diamondised nanocarbon-loaded poly(lactic acid) composites for highly electroactive surfaces: extrusion and characterisation of filaments for improved 3D-printed surfaces". en. In: *Microchimica Acta* 190.9 (Sept. 2023), p. 370. ISSN: 0026-3672, 1436-5073. DOI: 10.1007/s00604-023-05940-7. URL: <https://link.springer.com/10.1007/s00604-023-05940-7> (visited on 09/29/2023).
- [151] Fabiano M. De Oliveira, Edmar I. De Melo, and Rodrigo A.B. Da Silva. "3D Pen: A low-cost and portable tool for manufacture of 3D-printed sensors". en. In: *Sensors and Actuators B: Chemical* 321 (Oct. 2020), p. 128528. ISSN: 09254005. DOI: 10.1016/j.snb.2020.128528. URL: <https://linkinghub.elsevier.com/retrieve/pii/S0925400520308741> (visited on 09/29/2023).
- [152] Filip Novotný et al. "Preserving Fine Structure Details and Dramatically Enhancing Electron Transfer Rates in Graphene 3D-Printed Electrodes via Thermal Annealing: Toward Nitroaromatic Explosives Sensing". en. In: *ACS Applied Materials & Interfaces* 11.38 (Sept. 2019), pp. 35371–35375. ISSN: 1944-8244, 1944-8252. DOI: 10.1021/acsami.9b06683. URL: <https://pubs.acs.org/doi/10.1021/acsami.9b06683> (visited on 10/02/2023).
- [153] Fakher M. Rabboh and Glen D. O'Neil. "Voltammetric pH Measurements in Unadulterated Foodstuffs, Urine, and Serum with 3D-Printed Graphene/Poly(Lactic Acid) Electrodes". en. In: *Analytical Chemistry* 92.22 (Nov. 2020), pp. 14999–15006. ISSN: 0003-2700, 1520-6882. DOI: 10.1021/acs.analchem.0c02902. URL: <https://pubs.acs.org/doi/10.1021/acs.analchem.0c02902> (visited on 10/02/2023).
- [154] Cristiane Kalinke et al. "Comparison of activation processes for 3D printed PLA-graphene electrodes: electrochemical properties and application for sensing of dopamine". en. In: *The Analyst* 145.4 (2020), pp. 1207–1218. ISSN: 0003-2654, 1364-5528. DOI: 10.1039/C9AN01926J. URL: <http://xlink.rsc.org/?DOI=C9AN01926J> (visited on 10/02/2023).
- [155] Aug. 2016. URL: <https://www.buitink-technology.com/pdf/tpu-chemical-resistance.pdf>.
- [156] Diego P. Rocha et al. "Posttreatment of 3D-printed surfaces for electrochemical applications: A critical review on proposed protocols". en. In: *Electrochemical Science Advances* 2.5 (Oct. 2022), e2100136. ISSN: 2698-5977, 2698-5977. DOI: 10.1002/elsa.202100136. URL: <https://chemistry-europe.onlinelibrary.wiley.com/doi/10.1002/elsa.202100136> (visited on 09/29/2023).
- [157] Pãmyla L. Dos Santos et al. "Enhanced performance of 3D printed graphene electrodes after electrochemical pre-treatment: Role of exposed graphene sheets". en. In: *Sensors and Actuators B: Chemical* 281 (Feb. 2019), pp. 837–848. ISSN: 09254005. DOI: 10.1016/j.snb.2018.11.013. URL: <https://linkinghub.elsevier.com/retrieve/pii/S0925400518319609> (visited on 09/29/2023).

- [158] Roger Domingo-Roca et al. "Integrated multi-material portable 3D-printed platform for electrochemical detection of dopamine and glucose". en. In: *The Analyst* 147.20 (2022), pp. 4598–4606. ISSN: 0003-2654, 1364-5528. DOI: [10.1039/D2AN00862A](https://doi.org/10.1039/D2AN00862A). URL: <http://xlink.rsc.org/?DOI=D2AN00862A> (visited on 10/01/2023).
- [159] Cheng Yang et al. "3D-Printed Carbon Electrodes for Neurotransmitter Detection". en. In: *Angewandte Chemie International Edition* 57.43 (Oct. 2018), pp. 14255–14259. ISSN: 1433-7851, 1521-3773. DOI: [10.1002/anie.201809992](https://doi.org/10.1002/anie.201809992). URL: <https://onlinelibrary.wiley.com/doi/10.1002/anie.201809992> (visited on 10/01/2023).
- [160] Michael C. Granger and Greg M. Swain. "The Influence of Surface Interactions on the Reversibility of Ferri/Ferrocyanide at Boron-Doped Diamond Thin-Film Electrodes". In: *Journal of The Electrochemical Society* 146.12 (Dec. 1999), pp. 4551–4558. ISSN: 0013-4651, 1945-7111. DOI: [10.1149/1.1392673](https://doi.org/10.1149/1.1392673). URL: <https://iopscience.iop.org/article/10.1149/1.1392673> (visited on 10/01/2023).
- [161] Haichang Guo et al. "Highly Thermally Conductive 3D Printed Graphene Filled Polymer Composites for Scalable Thermal Management Applications". en. In: *ACS Nano* 15.4 (Apr. 2021), pp. 6917–6928. ISSN: 1936-0851, 1936-086X. DOI: [10.1021/acsnano.0c10768](https://doi.org/10.1021/acsnano.0c10768). URL: <https://pubs.acs.org/doi/10.1021/acsnano.0c10768> (visited on 11/04/2022).
- [162] A J Marsden et al. "Electrical percolation in graphene-polymer composites". In: *2D Materials* 5.3 (June 2018), p. 032003. ISSN: 2053-1583. DOI: [10.1088/2053-1583/aac055](https://doi.org/10.1088/2053-1583/aac055). URL: <https://iopscience.iop.org/article/10.1088/2053-1583/aac055> (visited on 11/03/2022).

A Appendix 1

Table A.1: Resin composition experiments using different molds.

Resin ^{1, 2}	Additive	Weight percent	Mold material	Curing machine	Exposure time (min)	Temperature (°C)	Sample thickness (mm)	Cured	Remarks
A	-	-	PLA	Envision	60	50	2.5	yes	- Electrodes very hard, not flexible. Impossible to remove from mold, needs to be broken.
A	-	-	PLA	Envision	40	50	2.5	yes	- Electrodes very hard, not flexible. Impossible to remove from mold, needs to be broken.
A	-	-	PLA	Envision	20	40	2.5	yes	- Electrodes very hard, not flexible. Impossible to remove from mold, needs to be broken.
A	-	-	PLA	Envision	12	40	2.5	yes	- Electrodes very hard, not flexible. Impossible to remove from mold, needs to be broken.
A	-	-	Steel	Envision	10	40	1	yes	- Electrodes still not very flexible, but easier to remove and molds are reusable
A	-	-	Steel	Envision	10	0	1	yes	- Electrodes getting more flexible but still not as desired. Easy to remove.
A	-	-	Steel	Envision	8	45	1	yes	- Electrodes flexible but difficult to remove from mold.
A	-	-	Steel	Envision	4	45	1	yes	- Electrodes are flexible and easy to remove from mold.
A	Boromond BDD	10 wt. %	Steel	Envision	4	45	1	no	- Electrode not fully cured, increase exposure time.
A	Boromond BDD	10 wt. %	Steel	Envision	10	45	1	no	- Electrode not fully cured + shrinkage visible on top of the surface.
A	Boromond BDD	10 wt. %	Steel	Envision	30	0	1	no	- Adequate result, better curing, but still shrinkage on surface and not fully cured.

A	Boromond BDD	10 wt. %	Steel	Envison	30	0	1	no	- Better result, added glass plate on top of surface to reduce shrinkage. But samples curl up due to internal stress and not fully cured.
B	-	-	Steel	Envison	8	0	1	yes	- New flexible, transparent resin used and tested to see curability.
B	Boromond BDD	10 wt. %	Steel	Envison	50	0	1	no	- Not cured well, sample was torn.
B	Boromond BDD	10 wt. %	PMMA	Envison	50	0	2	yes	- Well cured, good sample.
B	Boromond BDD	20 wt. %	PMMA	Envison	45	0	2	no	- Top cured and bottom cured but in between still uncured resin present.
B	Boromond BDD	20 wt. %	PMMA	Envison	60 top 35 bottom	0	2	no	- Sample felt soft and wrinkly. In middle of sample still uncured resin left.
B	Boromond BDD	20 wt. %	PMMA	Envison	75 top 35 bottom	0	2	no	- Sample still only on top-side and bottom cured, but in between uncured resin.
B	Boromond BDD	15 wt. %	PMMA	Envison	80 top 50 bottom	0	2	no	- Sample still only on top-side and bottom cured, but in between uncured resin.
B	Boromond BDD (acetone dispersed)	15 wt. %	PMMA	Envison	90	0	1	no	- Bottom thinner than top was less cured. Still uncured resin in middle.
B	Boromond BDD (acetone dispersed)	15 wt. %	PMMA	Envison	90 top 45 bottom	0	1	no	- Still shrinkage on top, very little of uncured resin present.
B	Boromond BDD (ethanol dispersed)	15 wt. %	PMMA	Envison	90 top 45 bottom	0	1	no	- Still little uncured resin present in the mold. Samples seemed to stick more to the mold. Difficult to remove.
B	Boromond BDD (ethanol dispersed)	15 wt. %	PMMA	Envison	90 top 45 bottom	0	2	no	- More uncured resin present in mold. Difficult to remove samples.
B	Boromond BDD	1 wt. %	PMMA	Envison	12	0	2	yes	- Good result. Sample was well cured and no shrinkage on top.
B	Boromond BDD	0.5 wt. %	PMMA	Envison	12	0	2	yes	- Good result. Sample was well cured and no shrinkage on top.
B	Boromond BDD	0.25 wt. %	PMMA	Envison	12	0	2	yes	- Good result. Sample was well cured and no shrinkage on top.
B	Boromond BDD	15 wt. %	PMMA	Dentalfarm photopol	10 min 400 nm 13 min 320 nm	-	2	no	- Shrinkage on top of the sample. 320 nm mode generates substantial heat. Half way cured.
B	Boromond BDD	15 wt. %	PMMA	Dentalfarm photopol	40 min 400 nm 15 min 320 nm	-	1	no	- After 40 min, top still wet, not cured. Changed to 320 nm mode, but sample became very hot (60-80 °C). Shrinkage on top of sample.
B	Boromond BDD	15 wt. %	PMMA	Dentalfarm photopol	12 min 400 nm 8 min 320 nm	-	1	no	- Sample almost cured, little uncured resin left. Sample top added to prevent shrinkage.
B	Boromond BDD	15 wt. %	PMMA	Dentalfarm photopol	18 min 400 nm 10 min 320 nm	-	1	no	- Glass top added to prevent shrinkage. Top and bottom both cured but sample felt soft and inside still uncured resin.

B	Boromond BDD	12 wt. %	PMMA	Dentalfarm photopol	60 min 400 nm 25 min 320 nm	-	1	no	- After 60 min 400 nm mode top still wet and not cured. Shrinkage again appeared when switching to 320 nm mode. Layers coming off. Sample not fully cured. But sample not fully cured.
B	Boromond BDD	12 wt. %	PMMA	Envison	70 top 30 bottom	0	1	no	- After 30 min top was cured already.
B	Boromond BDD	12 wt. %	PMMA	Envison	90 top 30 bottom	0	1	no	- Little shrinkage. Intact, not damaged. Still uncured resin in middle.
B	Boromond BDD	12 wt. %	PMMA	Envison	90 top 30 bottom	0	2	no	- Little shrinkage. Intact, not damaged. Still uncured resin in middle.
B	Boromond BDD	12 wt. %	PMMA	Envison	120	0	1	no	- Sample almost fully cured, but still uncured resin inside sample.
B	Ultrahard BDD	5 wt. %	PMMA	Envison	75	0	1	yes	- Sample fully cured but only some damage possibly due to internal stresses.

¹Resin A = Prusa flexible transparent
²Resin B = Prusa Flex80 transparent

Table A.2: Experimental overview of all resin compositions used for SLA-printing.

Material	BDD wt. %	Initial layer exposure (s)	Next layer exposure (s)	Layer thickness (μm)	Tilting profile	Successful print
Flex resin	0	25	5	50	viscous	yes
BDR	10	50	10	50	viscous	no
BDR	10	100	20	50	viscous	yes
BDR	15	100	20	50	viscous	no
BDR	15	120	40	50	viscous	no
BDR	15	120	50	50	viscous	no
BDR	15	120	50	25	viscous	no
BDR	15	120	50	25	Highly viscous	no
BDR	12.5	120	30	50	Highly viscous	no
BDR	12.5	120	30	25	Highly viscous	yes
UDR	5	50	10	50	viscous	yes
UDR	15	120	30	25	Highly viscous	no
UDR	12.5	120	30	25	Highly viscous	no
UDR	10	120	30	25	Highly viscous	no
UDR	7.5	120	30	25	Highly viscous	yes

B Appendix 2

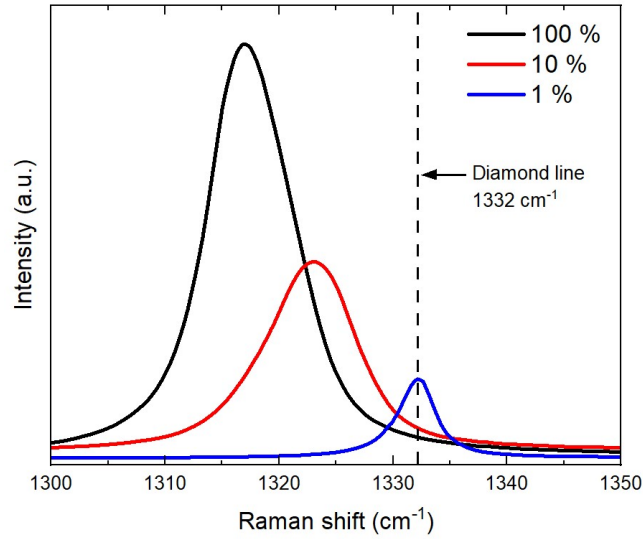


Figure B.1: Comparison of Raman peak of (Boromond) BDD samples measured with different laser power. A reference bulk diamond Raman line at 1332 cm⁻¹ is shown as a vertical dashed line.

Table B.1: Material properties calculated from tensile and electrical tests of all SLA-printed composite samples cured for 1 hour at 70 °C

Samples	Young's modulus (MPa)	Tensile strength (MPa)	Elongation (%)	Conductivity (S/cm)
Flex80	4.72 ± 0.06	9.74 ± 0.48	189 ± 8.1	Not measurable
BDR-5	4.71 ± 0.06	7.98 ± 0.35	165 ± 7.1	Not measurable
BDR-10	4.94 ± 0.12	8.19 ± 0.96	159 ± 11.3	Not measurable
BDR-12.5	4.86 ± 0.09	6.59 ± 0.19	133 ± 2.1	Not measurable
UDR-2.5	3.90 ± 0.16	6.48 ± 0.23	163 ± 4.4	Not measurable
UDR-5	3.78 ± 0.16	6.06 ± 0.95	152 ± 16.0	Not measurable
UDR-7.5	3.73 ± 0.05	5.44 ± 0.06	139 ± 2.5	Not measurable

Table B.2: Overview of process parameters for the formulation of FDM composites.

Polymer	Carbon additives	Solvent(s)	Mixing conditions	Evaporation conditions	Author(s)
TPU/PLA (7:3)	Graphite (treated) 0.5 – 2 wt.%	TPU in DMF (150 mg/ml) PLA in DCM (100 mg/ml) Graphite in DMF (5 mg/ml)	60 °C for 5 h (stirring). 20 °C for 10 h (stirring). Ultrasonication for 1 h. All solutions put together, stirred vigorously overnight.	Vacuum drying at 40 °C for 24 h	[144]
TPU	Graphene sheets 5 – 45 wt.%	TPU in DMF	20 °C for 12 h (stirring). Graphene added to solution (sonicated + stirred).	Drying at 120 °C for 24 h	[161]
PLA	Nanocarbon 1 – 20 wt.%	PLA in DCM (1:5 w/v ratio)	80 °C for 2 h (stirring) in airtight bottle. NC added and stirred for 30 min.	Solution poured in aluminum dish and dried overnight.	[106]
ABS	BDD + LiCl 37.5 wt.% and 60 wt.%	ABS in acetone BDD in acetone	Sonicated 80 min. Sonicated 80 min. Combined and mixed/sonicated for 80 min.	Dry overnight + 100 °C for 2 h.	[119]
PVDF	MWCNTs 1 – 15 wt.%	PVDF in DMF (0.1 g/ml)	Stirring at 60 °C until dissolved (no time). MWCNTs added and ultrasonic blended (probe) for 15 min.	Dried in oven at 75 °C for 16 h.	[89]
PLA	Graphite 50 – 70 wt.%	PLA in DCM (1:10 weight ratio)	20 °C for 1 h (stirring). Graphite added and stirred for 30 min extra.	Dried at room temperature for 3 h on glass with doctor blade. Poured in large area container and left overnight.	[112]
ABS	CNTs 0 – 10 wt.%	CNTs in acetone	Ultrasound mixing (probe) for 30 min. Polymer added to solution and stirred for 5 h.	Additional 100 °C for 1 hour.	[93]
PLA	Nanocarbon 0 – 15 wt.%	PLA in DCM (0.1 g/ml) for high wt.% of NC. PLA in DMC (0.2 g/ml) for low wt.% of NC.	Not mentioned	Dried 24 h at room temperature	[110]

Percolation threshold

The fundamental aspect of electrical conductivity within the printed composite electrodes will depend on the percolation threshold. Due to the insulating behavior of most (thermoplastic) polymers, a conductive composite can only be achieved by addition of sufficient conductive particles. For a random distribution of these conductive fillers, a conductive network will form in the composite material at a specific loading, known as the percolation threshold (ρ_c). At the percolation threshold, the change in conductivity with respect to the added weight percentage (or volume) of conductive fillers will be at a maximum. The trajectory of the conductivity is characterized by an S-shape, demonstrating three regimes: insulating, percolating and conductive (shown in Figure B.2).

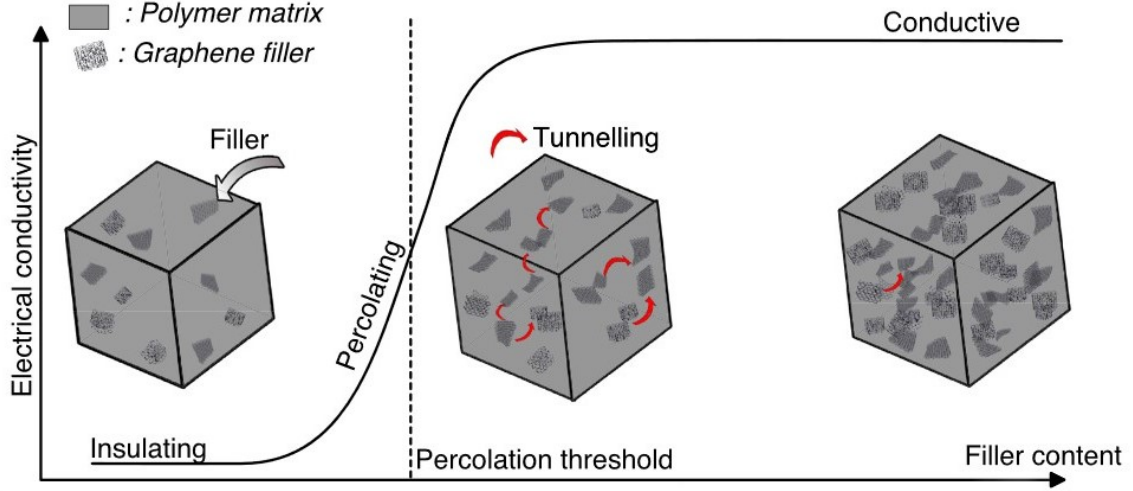


Figure B.2: A schematic of conduction mechanisms in a composite with increasing filler content [162].

The conductive behavior within these three regimes can be understood from the microstructure of the composite. When there is no conductive path formed, no charge can pass through the material, and the composite will show an insulating response. On the other hand, when there is a sufficient filler concentration present, a conductive path is formed through the material and the composite will be electrically conductive. In between these two phases, there is a region where the conduction is not induced by direct contact of the fillers, but by electrons "jumping" across the fillers through a process called electron tunneling. In this process, electrons will tunnel through an interface formed between the fillers and polymer matrix. The conductivity is in this case lower than when the fillers form direct contacts. The percolation threshold varies with respect to the polymer and filler types. Multiple other parameters also affect the percolation threshold of the composite, such as temperature [140] and filler dimensions [141].

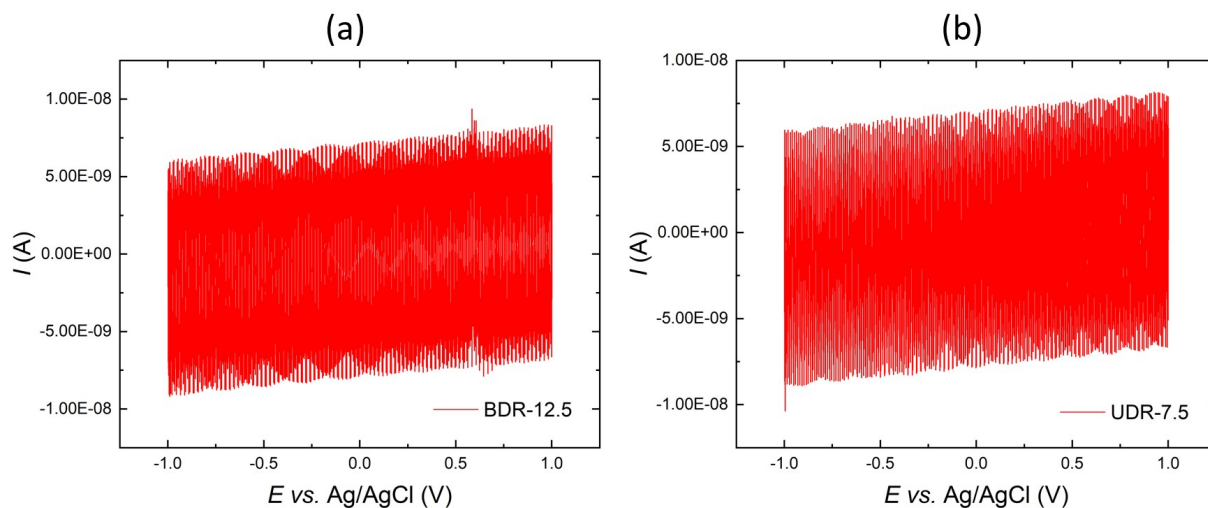


Figure B.3: Response obtained in 0.5 M KNO₃ on (a) BDR-12.5 and (b) UDR-7.5 composite. Scan rate 100 mV/s.

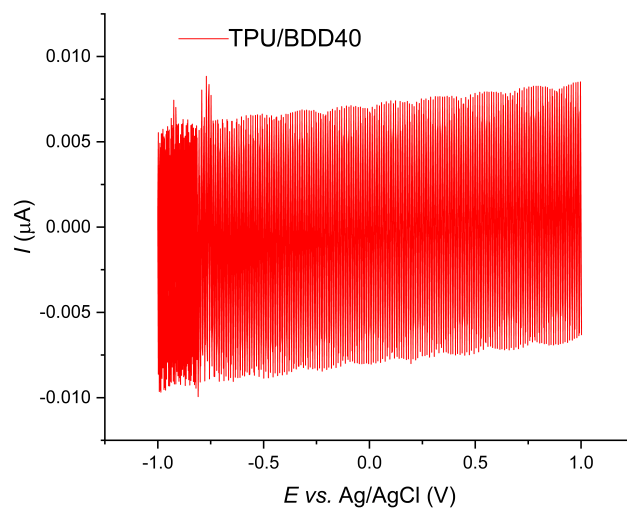


Figure B.4: Response obtained in 0.5 M KNO₃ on TPU/BDD40 composite. Scan rate 100 mV/s.

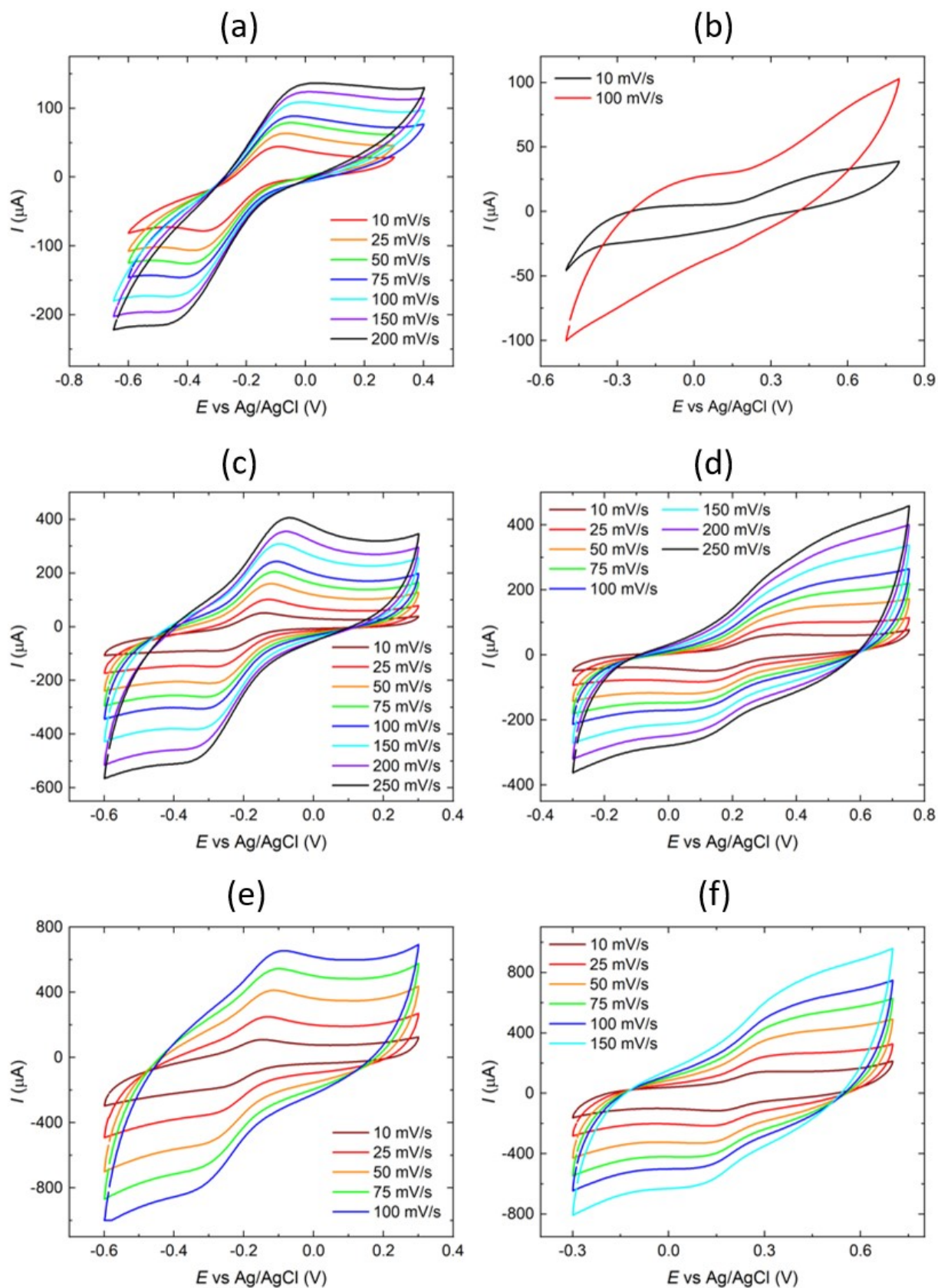


Figure B.5: Multiple scan rate voltammograms in 1mM RuHex (a,c,e) and 1mM ferrocyanide (b,d,f) for TPU/CNT (a,b), TPU/CNT/BDD(1:1) (c,d) and TPU/CNT/BDD(1:2) (e,f).

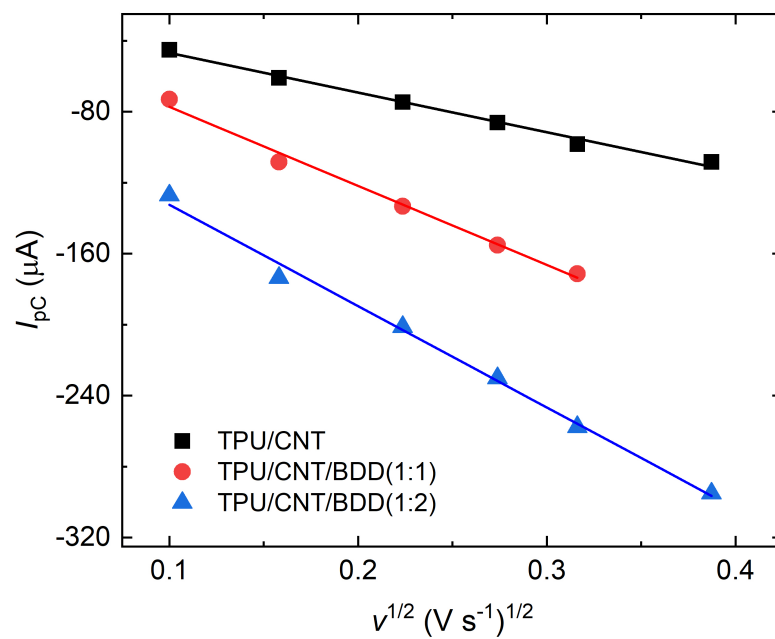


Figure B.6: Graph presenting the linear dependence of $i_{p,C}$ on square root of scan rate for three tested electrode compositions.

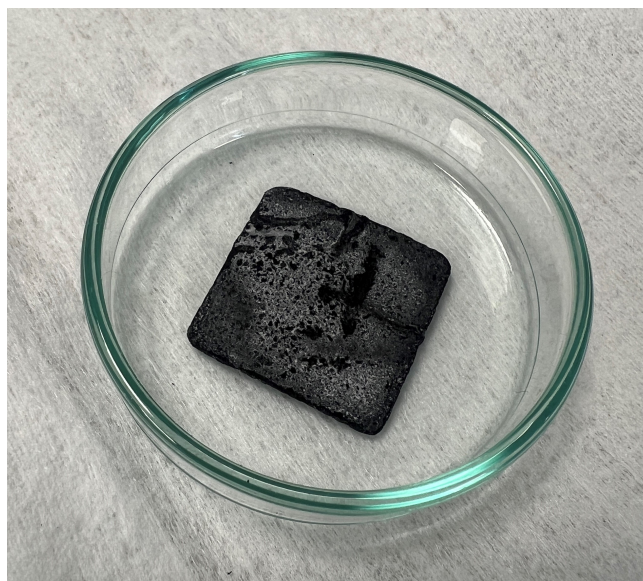


Figure B.7: Image of 3-D printed electrode after removal from DMF and rinsed with DI water. The white layer is presumably precipitated TPU.

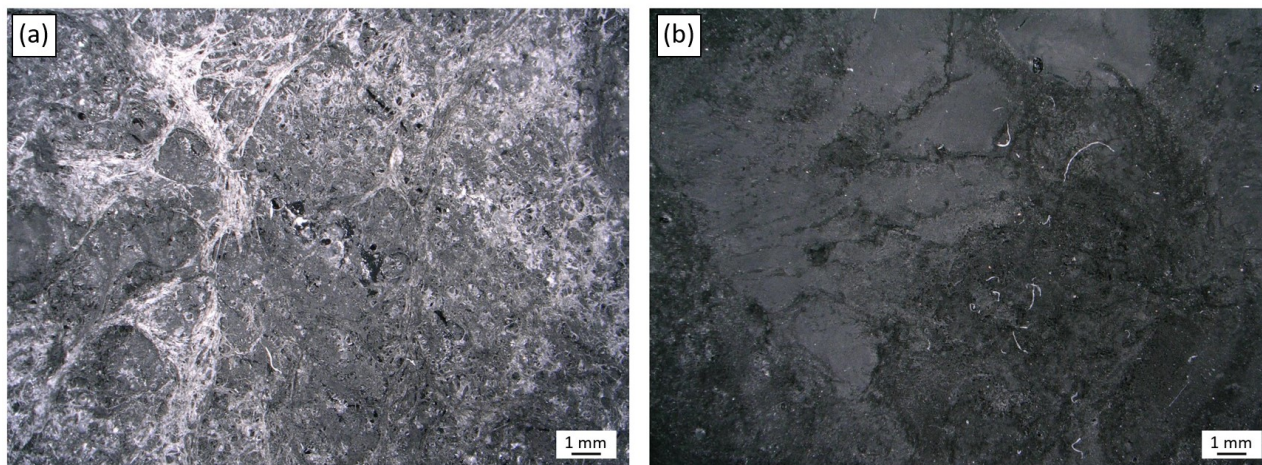


Figure B.8: Optical image of electrode surface after (a) and before (b) mechanical polishing.

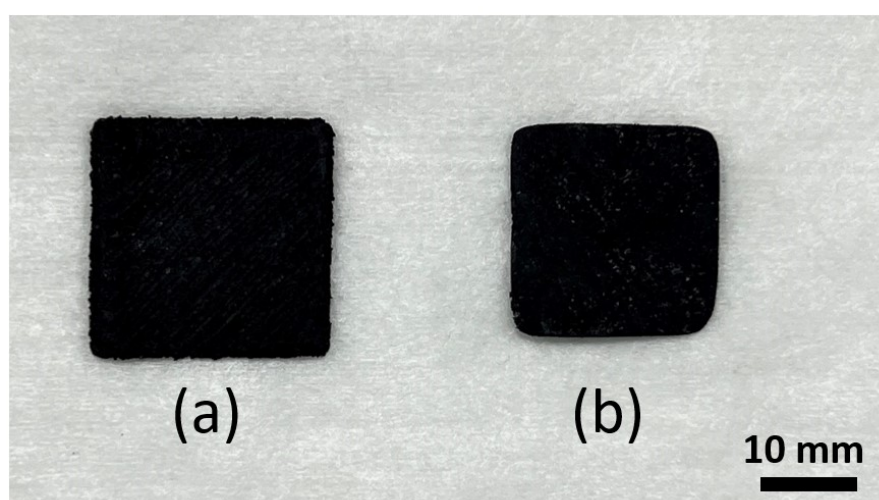


Figure B.9: Image of 3-D printed electrode (a) before and (b) after surface treatment.

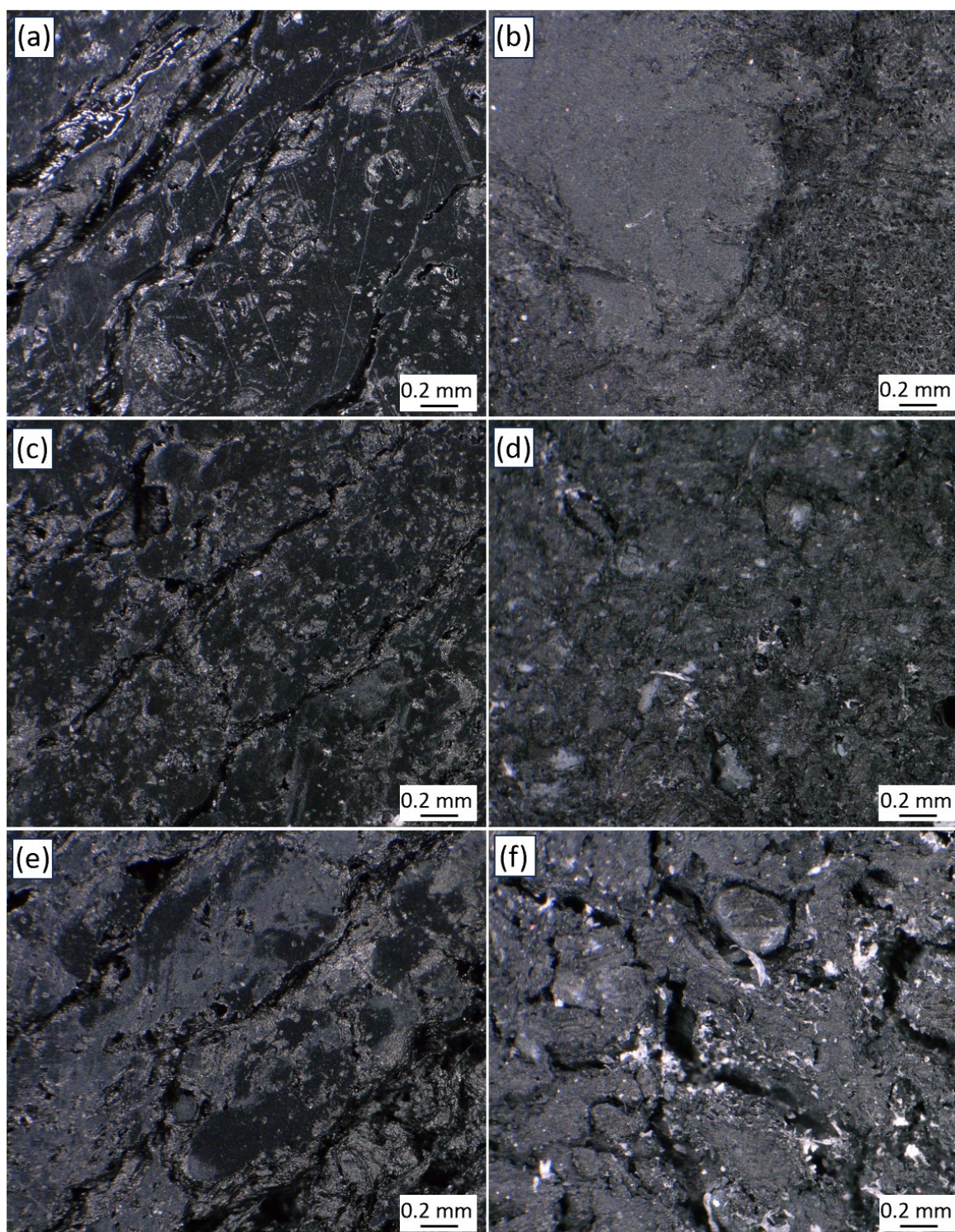


Figure B.10: Optical images of 3D-printed samples before (a,c,e) and after (b,d,f) electrode surface treatment. Electrodes are (a,b) TPU/CNT, (c,d) TPU/CNT/BDD(1:1) and (e,f) TPU/CNT/BDD(1:2).

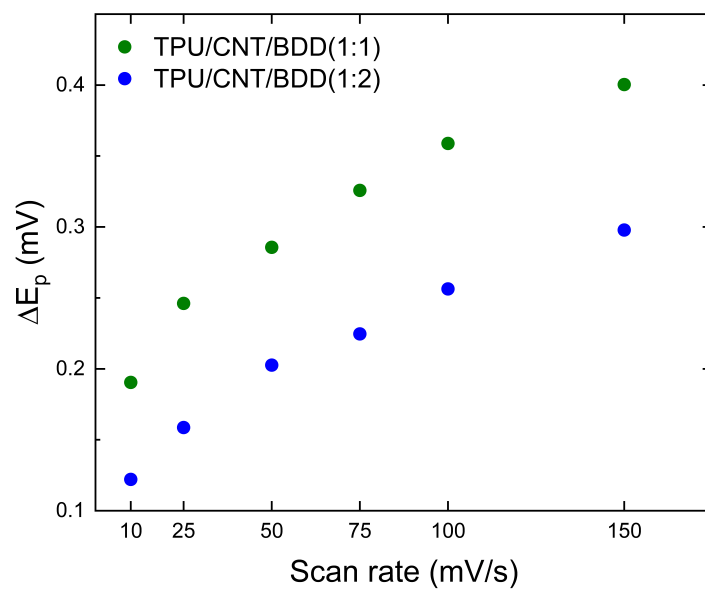


Figure B.11: Plots of ΔE_p versus the scan rate recorded in 1mM ferrocyanide in 0.5M KNO_3 .

